

# Computational methods for live heart imaging with speed-constrained microscopes

Présentée le 1<sup>er</sup> février 2021

Faculté des sciences et techniques de l'ingénieur  
Laboratoire de l'IDIAP  
Programme doctoral en génie électrique

pour l'obtention du grade de Docteur ès Sciences

par

**Olivia MARIANI**

Acceptée sur proposition du jury

Prof. M. Unser, président du jury  
Dr J.-M. Odobez, Dr M. S. D. Liebling, directeurs de thèse  
Prof. N. Mercader Huber, rapporteuse  
Prof. M. J. Ledesma-Carbayo, rapporteuse  
Prof. A. Radenovic, rapporteuse



“Questions don’t have to make sense, Vincent,” said Miss Susan.

“But answers do.”

— Terry Pratchett, *Thief of Time*

To my family





# Acknowledgements

I would like to thank my supervisor, Michael Liebling, for giving me the opportunity to do this thesis in his lab, for his availability and guidance. A special thanks to Alexander with whom I collaborated throughout this thesis, for the many datasets he produced, including most of those featured in this thesis, his expert eye for light-sheet microscopy, and for the interesting discussions.

I would like to thank the members of my lab and office for their scientific and moral support through coffee break discussions. In particular Christian for the motivational talks and François for his positive energy. Hakan for the food discussions and the many kilos of baklava, and Thibaut for his deep study of the Swiss alps.

On a more personal level, I would like to thank my family and friends for their support, Lionel for giving me the courage to start this adventure, and Hugues for the moral support throughout this thesis.

*Martigny, January 12, 2021*

O. M.



# Abstract

Imaging methods to capture the beating and developing heart inside embryonic animal models such as the zebrafish are a key component for the study of fundamental biological processes such as cardiac birth defects or tissue regeneration. However, live heart imaging is subject to many challenges that limit the achievable spatial and temporal resolutions, which must be high enough to discern fine structures and fast processes, respectively.

While many commonly available microscopes offer the necessary optical sectioning capabilities to produce slices or 3D volumes at the required scale, they often lack the necessary speed to seamlessly resolve the beating heart within a still frame, the entire heartbeat, or over a complete developmental sequence.

In this thesis, I aim to assemble dynamic image series of the heart by using a wide range of microscopes, including, in particular, scanning microscopes—which are widely available but slow—and microscopes with a slow framerate.

First, I considered the problem of reconstructing an image sequence covering one heartbeat from still images acquired in multiple cardiac cycles, with each image triggered at an arbitrary time, when the underlying cardiac motion pattern is temporally asymmetrical. I proposed to solve the sequence creation by sorting the images such as to maximize the overall similarity between contiguous frames, which I formulated as a traveling salesman problem. The performance of the method increases with the number of images. I demonstrated I could reconstruct image sequences of the heart at a virtual frame-rate of up to 300 frames per second.

Second, I relaxed the cardiac motion assumption to allow for symmetric patterns, provided the imaging setup permits active illumination. To resolve the ill-posedness of the sorting problem when identical object poses appear multiple times in one cycle, I proposed to illuminate the scene with a temporally-asymmetric pattern in alternate frames. Sorting issues are thereby mitigated at the cost of a more sophisticated setup and additional light exposure without adversely affecting the reconstructed sequence.

Third, I considered the problem of imaging the beating heart on conventional scanning confocal microscopes that have a frame scanning rate comparable to the heartbeat rate. My approach takes a set of images that may contain scanning aberrations, each triggered at an arbitrary time in the cardiac cycle, and assembles it into an image sequence that covers a single heartbeat. Reconstructing scanning-aberrated frames (which intrinsically patterns the illumination) offers a robust alternative for confocal LSM. The quality of recovered heartbeat dynamics is comparable to that obtained by fast microscopes.

Finally, I considered the problem of building smooth time-lapse sequences in the cardiac

## Abstract

---

phase versus development or cardiac phase versus imaging depth spaces based on a set of still images captured at weakly-constrained times within the heartbeat cycle and over the course of development or at various depths in the heart. This method determines a smooth path in cardiac phase-development or depth space enforcing neighborhood similarity via a within-stage (or within-depth) sorting followed by a cyclical least-squares phase alignment approach that I formulated as a mixed integer linear problem. Constraining the paths of time-lapses by providing key-points together while enforcing local similarity successfully stabilizes the excursion error from which recursive registration approaches suffer.

The results suggest that reliably imaging the heart on a wide range of microscopes is possible, provided the heart motions are stereotypical and that minimal sampling constraints are met. The newly gained possibility of using conventional instruments (confocal microscope, fast snapshots with slow repetition rate) may be particularly relevant for applications with emerging modalities that do not allow wide-field capture (multi-photon imaging). This thesis opens the possibility to study cardiac functions within developing organisms on a wider range of imaging instruments.

## Résumé

L'étude de processus biologiques fondamentaux tels les anomalies cardiaques congénitales ou la régénération tissulaire, dépendent de méthodes d'imagerie capable de capturer le développement cardiaque à l'intérieur de l'embryon d'animaux modèles. Cependant, la capture du coeur en temps réel a de nombreuses problématiques qui contraignent les résolutions spatiales et temporelles, le but étant de discerner à la fois les structures fines, et les processus rapides. De nombreux modèles courants de microscopes offrent le sectionnement optique nécessaire pour produire des plans ou des volumes à la résolution requise, mais leur vitesse d'acquisition ne permet souvent pas de discerner le coeur en temps réel, que ce soit au sein d'une image, d'un battement cardiaque, ou d'une séquence couvrant le développement cardiaque entier. L'objectif de cette thèse est d'assembler des séries d'images dynamiques du coeur dans une large gamme de microscopes, dont notamment des microscopes confocaux à balayage laser, qui sont lents mais courants, et des microscopes dont la fréquence d'acquisition d'images est lente.

Je me suis d'abord attaquée au problème de reconstruction d'une séquence d'image couvrant un battement cardiaque à partir d'images acquises à des temps arbitraires, sur plusieurs battements, sachant que les mouvements du coeur sont asymétriques. Pour résoudre cette problématique, j'ai proposé de trier les images de façon à maximiser la similarité entre images adjacentes. J'ai formulé cette approche comme un problème du voyageur de commerce. La performance de la méthode croît avec le nombre d'images. J'ai démontré qu'on pouvait atteindre un taux d'acquisition virtuel de 300 images par seconde.

Ensuite, j'ai assoupli l'hypothèse d'asymétrie pour inclure les mouvements symétriques. Pour que cette méthode soit réalisable, le dispositif de capture d'image doit permettre l'utilisation d'illumination structurée. Pour résoudre le caractère mal-posé du problème de tri quand une configuration d'objet apparaît plus d'une fois dans un cycle, je propose d'illuminer de façon alternée la scène avec un motif d'illumination temporellement asymétrique. Les problèmes de tri sont ainsi résolus, au prix d'un dispositif plus sophistiqué et de plus de temps d'exposition, sans affecter la reconstruction de la séquence.

Puis j'ai considéré le problème d'acquérir, avec un microscope confocal à balayage laser conventionnel qui a une vitesse de balayage similaire au battement cardiaque, des images de coeur en temps réel. Mon approche considère une série d'images, acquises à des temps arbitraires du battement cardiaque et qui peuvent contenir des aberrations de balayage, pour les assembler en une séquence d'images couvrant un unique battement cardiaque. La reconstruction d'images exemptes d'aberration de balayage (qui modèlent intrinsèquement l'illumination)

offre une alternative robuste au microscope confocal à balayage laser. La qualité de recouvrement de la dynamique du battement cardiaque est similaire à celle obtenue avec des microscopes rapides.

Enfin, je me suis intéressée au problème de la création de séquences vidéo illustrant la phase cardiaque à différents stades de développement ou à différentes profondeurs de coupe optique. Pour mon approche, j'utilise des images capturées avec une faible contrainte temporelle au sein du cycle cardiaque, à différentes phases de développement ou de profondeur de coupe. Cette méthode établit un chemin graduel entre les phases de développement ou dans l'espace de profondeur, en forçant la similarité entre voisinage à travers un tri effectué au sein d'une phase de développement ou d'une coupe de profondeur. Cette étape est suivie d'une approche cyclique aux moindres carrés d'alignement de phases, que j'ai formulée comme un problème linéaire d'entiers mélangés. Contraindre les chemins des vidéos avec intervalles en offrant des points-clés tout en imposant des similarités locales permet de stabiliser l'erreur d'excursion dont souffrent les méthodes de recalage récursif.

Les résultats suggèrent qu'il est possible d'imager fidèlement le cœur sur une large gamme de microscopes, pour autant que les mouvements du cœur soient stéréotypiques et que les contraintes d'échantillonnages minimales soient atteintes. La possibilité nouvellement acquise d'utiliser des instruments d'imagerie conventionnels (microscope à balayage laser, images instantanées avec taux de répétition basse) peut être particulièrement intéressante pour les applications sur méthodes d'imageries émergentes pour lesquelles l'imagerie à grand-champ est exclue (imagerie multiphoton). Cette thèse ouvre la voie à l'étude de fonctions cardiaques dans des organismes en cours de développement pour une gamme plus large d'instruments d'imagerie.

# Contents

<b>Acknowledgements</b>	<b>i</b>
<b>Abstract (English/Français)</b>	<b>iii</b>
<b>1 Live cardiac imaging in microscopy</b>	<b>1</b>
1.1 Time resolution . . . . .	1
1.2 Time series completion . . . . .	3
1.3 Sorting periodic symmetric sequences . . . . .	3
1.4 Still frame acquisition in point-scanning microscopy . . . . .	3
1.5 4-Dimensional acquisition . . . . .	4
<b>2 Sorting of periodic time-series</b>	<b>7</b>
2.1 Virtual High-Framerate Microscopy of the Beating Heart via Sorting of Still Images	7
2.2 Methods . . . . .	8
2.2.1 Imaging Model and Problem Statement . . . . .	8
2.2.2 Virtual Frame-Rate Improvement via Sorting . . . . .	9
2.3 Results . . . . .	10
2.3.1 Method Characterization on Synthetic Data . . . . .	10
2.3.2 Validation on Experimental Measurements . . . . .	11
2.4 Discussion and Conclusion . . . . .	12
<b>3 Structured illumination to create asymmetry in the data</b>	<b>15</b>
3.1 Unequivocal cardiac phase sorting from alternating ramp- and pulse- illuminated microscopy image sequences . . . . .	15
3.2 Methods . . . . .	16
3.2.1 Imaging model and problem statement . . . . .	16
3.2.2 Phase-sorting ramp-, pulse-illuminated image pairs . . . . .	17
3.3 Results and Discussion . . . . .	17
3.4 Optical flow trajectories of sorted data . . . . .	17
3.4.1 Ground truth phases of sorted data . . . . .	20
3.4.2 Application on experimental data . . . . .	20
3.5 Conclusion . . . . .	21
<b>4 Scanning aberrations correction</b>	<b>23</b>

## Contents

---

4.1	Reconstruction of image sequences from ungated and scanning-aberrated laser scanning microscopy images of the beating heart . . . . .	23
4.2	Related work . . . . .	26
4.3	Contributions . . . . .	27
4.4	Model and Problem Definition . . . . .	29
4.5	Phase sorting, period completion and estimation method . . . . .	29
4.5.1	Sorting scanning-aberrated images according to cardiac phase . . . . .	30
4.5.2	Estimation of the heartbeat period . . . . .	31
4.5.3	Scan-aberration compensation via resampling . . . . .	32
4.6	Experiments . . . . .	32
4.6.1	Expected error due to non-gated, non-uniform sampling . . . . .	33
4.6.2	Method characterization on synthetic data . . . . .	33
4.6.3	Evaluation of the overall accuracy of the proposed reconstruction method . . . . .	37
4.6.4	Reconstruction of a beating heart sequence from experimental measurements . . . . .	39
4.6.5	Reconstruction independence on scanning direction . . . . .	40
4.6.6	Comparison to state-of-the-art fast microscopes . . . . .	41
4.7	Discussion . . . . .	42
4.8	Conclusion . . . . .	44
4.A	Scanning-aberrations correction in volumetric data . . . . .	45
4.A.1	Method . . . . .	45
4.A.2	Preliminary results on simulated data . . . . .	45
4.A.3	Discussion and prospective future work . . . . .	46
<b>5</b>	<b>Constrained sequence extraction for time-lapses and volumes</b>	<b>49</b>
5.1	Cardiac image sequence extraction from still images with unknown heartbeat phases . . . . .	49
5.2	Imaging Model and Problem Statement . . . . .	51
5.3	Methods . . . . .	53
5.4	Sorting frames acquired within an interval $r_i$ . . . . .	54
5.5	Relative phase-shift between consecutive sequences . . . . .	54
5.6	Sequence extraction . . . . .	55
5.7	Experiments . . . . .	56
5.8	Method characterization using synthetic data . . . . .	56
5.8.1	Phase error characterization . . . . .	57
5.9	Comparison to existing methods . . . . .	57
5.9.1	Time-lapse data acquisition simulation . . . . .	57
5.9.2	Comparison of excursion error . . . . .	59
5.9.3	Excursion error on simulated volumetric data . . . . .	59
5.10	Validation on experimental data . . . . .	60
5.10.1	Timelapse of the beating heart . . . . .	60
5.10.2	Volume reconstruction . . . . .	61



5.11 Discussion . . . . .	62
5.12 Conclusion . . . . .	64
<b>6 Conclusion and perspective</b>	<b>65</b>
6.1 Summary of contributions . . . . .	65
6.2 A short guidebook to imaging the live heart . . . . .	66
6.2.1 Living or fixed? . . . . .	66
6.2.2 Single phase imaging for the custom microscope-equipped researcher . . . . .	66
6.2.3 Commercially available microscopes as an alternative . . . . .	67
6.2.4 OpenSPIM . . . . .	68
6.2.5 Concluding recommendations . . . . .	68
6.3 Future perspectives . . . . .	68
6.3.1 Adaptive time-lapse volume acquisition . . . . .	68
6.3.2 Machine learning solutions . . . . .	69
6.4 Concluding remarks . . . . .	69
<b>A Microscopy and Zebrafish</b>	<b>71</b>
A.1 Microscopes . . . . .	71
A.1.1 Point-scanning confocal microscope . . . . .	72
A.1.2 Spinning disk . . . . .	72
A.1.3 AiryScan module . . . . .	73
A.1.4 Two-photon microscopy . . . . .	73
A.2 Zebrafish heart development . . . . .	74
<b>Curriculum Vitae</b>	<b>87</b>



# 1 Live cardiac imaging in microscopy

Optical microscopes are essential tools in biology and are to this day heavily used to study whole organisms, organs, cellular-level, or sub-cellular processes. New microscopy techniques are constantly developed to push back spatial and temporal resolution, to image smaller structures and faster processes. However, most often, one needs to reach a trade-off between spatial and temporal resolution, which can be especially problematic in the context of live imaging of fast moving objects such as the beating heart of developing embryos. Specifically, when capturing the beating and developing heart inside *live* embryonic animal models such as the zebrafish, imaging is subject to additional challenges. On one hand it is essential to reach sufficient spatial and temporal resolutions, which must be high enough to discern fine structures and fast processes, respectively and on the other hand maintaining the integrity of the sample is equally important.

## 1.1 Time resolution

Many commonly available microscopes offer the necessary optical sectioning capabilities to produce slices or 3D volumes at the required scale, but either lack temporal resolution, require special acquisition protocols, or need additional or custom hardware. The shortfall in speed translates to a lack of resolution, geometric deformations, or temporal irregularities, which can appear within still frames of the heart when it rapidly contracts, image and volume sequences of the entire heartbeat, or over observations that cover longer developmental stages.

Fig. 1.1 shows an overview of the current state-of-the art solutions for live fluorescence heart imaging. The two main approaches to heart imaging are prospective gating, when the cardiac phase is known at acquisition time (acquisition is gated or phase-locked to a certain heart-beat phase) and retrospective gating, when the phase is unknown at acquisition time and is estimated retrospectively.

Prospective gating methods [1] have aimed to acquire images of the heart at one phase of interest throughout volume and developmental time. They require a secondary signal detector

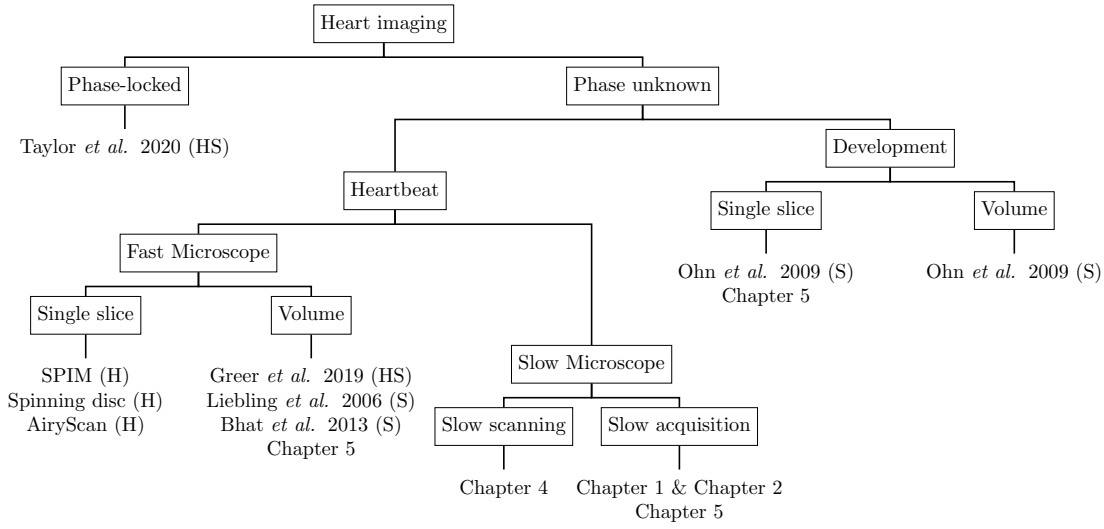


Figure 1.1 – Overview of microscopy solutions to image the beating heart of live zebrafish. "H" stands for hardware solutions, and "S" for software solutions. "HS" is for solutions that combine custom microscope and specialized software.

coupled with the acquisition hardware that can trigger the acquisition at the phase of interest. Taylor *et al.*, 2019 [2], proposed a hardware and software solution based on adaptive optical gating that allows 3D timelapse imaging of a single phase. Prospective gating has the advantage of not requiring any additional post-processing to synchronize the phases, as there is just one phase. The disadvantages are the need for a custom hardware and the loss of heartbeat dynamics. It is also not an ideal exploratory solution if the phase of interest is not known.

By contrast, retrospective gating does not assume any knowledge of the cardiac phase during imaging but requires post-processing for phase synchronization.

In this thesis, I will propose and characterize several cardiac imaging methods that all fall under the retrospective gating category, under various hardware and motion constraints and with various reconstruction objectives (still frames, dynamic volumes, etc.). Specifically, the methods are further organized (see Fig. 1.1) based on the type of motion involved (cardiac heartbeat only or cardiac heartbeat combined with motions due to organ development), the targeted image dimensionality (single slice or full volumes) and the type of microscope available for imaging (microscopes capable of capturing full-frames or volumes (near-)instantly versus microscopes whose image formation process is slow).

In the following sections (1.2–1.5) I provide a brief overview of the state-of-the-art, the problem formulation and chosen approach in each of the situation that I have covered in this thesis (see "Chapters" in the tree of Fig. 1.1). The proposed solutions both offer an alternative approach in cases where other solutions exist, but also cover configurations that have so far lacked accessible alternatives.

## 1.2 Time series completion

I first considered, in Chapter 2, the problem of reconstructing an image sequence covering one heartbeat from still images acquired in multiple cardiac cycles, with each image triggered at an arbitrary time, when the underlying cardiac motion pattern is temporally asymmetrical. Several sorting methods for periodic symmetric signals have been previously proposed [3, 4], both using Isomap [5], but either require use large datasets or additional post-processing.

I proposed to solve the sequence creation by sorting the images such as to maximize the overall similarity between contiguous frames, which I formulated as a traveling salesman problem. The performance of the method increases with the number of images. I demonstrated image sequences of the heart at a virtual frame-rate of up to 300 frames per second. This method is particularly useful for microscopes that have a fast frame acquisition rate, but have a slow bandwidth or slow camera. For example a fast confocal microscope such as a standard microscope with the AiryScan module, a line scanning microscope with a short dwell time, or a microscope with a camera that has an insufficient framerate.

## 1.3 Sorting periodic symmetric sequences

In Chapter 2 I proposed a method to sort still images of the beating heart acquired at random time in the cardiac cycle. However, the method I propose is restricted to periodic asymmetric signal, and cardiac time-series may contain symmetry points. In Chapter 3, I relaxed the cardiac motion assumption to allow for symmetric patterns, provided the imaging setup permits active illumination. Structured illumination using a spatial pattern has been used to reach spatial super-resolution [6], and a sub-frame *temporal* pattern has been shown to improve temporal resolution [7] and sampling [8]. Here, I proposed to illuminate the scene with a temporally-asymmetric pattern in alternate frames. Sorting issues are thereby mitigated at the cost of a more sophisticated setup and additional light exposure without adversely affecting the reconstructed sequence.

## 1.4 Still frame acquisition in point-scanning microscopy

Ideally, the acquisition time of a single frame should be short enough to only contain a single phase of the cardiac cycle. That is not always possible, in particular with laser-scanning microscopes. A standard point-scanning confocal microscope acquires one pixel at a time, and the signal-to-noise ratio directly depends on the pixel exposure time (dwell time). Despite the limited temporal resolution, standard confocal microscopes have many advantages such as a good optical sectioning, the possibility to acquire only a region of interest, and be available in many microscopy facilities, among others.

Some state-of-the-art microscopes, such as multi-photon microscopes, are usually point-scanning as well and the same compromise between dwell time and acquisition speed has to

be found. There are alternatives that satisfy the required temporal resolution. In light-sheet microscopy, illuminate an entire plane at once. Spinning disk confocal microscopes, which use rotating arrays of pinholes to illuminate one plane very fast, or Airyscan modules, which use a point detector array, increasing the acquisition speed and signal-to-noise-ratio, are fast enough to avoid scanning aberrations in still images. However, those microscopes and module are not always available or a viable alternative.

In Chapter 4, I propose a method taking as input scan-aberrated still image sequences of the beating heart, and giving as output a time-series of one scan-aberration-corrected heartbeat. My approach takes a set of images that may contain scanning aberrations, each triggered at an arbitrary time in the cardiac cycle, and assembles it into an image sequence that covers a single cardiac heartbeat. Reconstructing scanning-aberrated frames (which intrinsically patterns the illumination) offers a robust alternative for confocal LSM. The quality of recovered cardiac heartbeat dynamics is comparable to that obtained by fast microscopes.

### 1.5 4-Dimensional acquisition

Multidimensional acquisition of the beating heart has been explored in various imaging modalities, whether to reconstruct a beating heart volume, or a phase-synchronized timelapse.

In optical coherence tomography (OCT) for instance, which is highly used in mouse cardiac development studies [9], several techniques have been developed to reconstruct 3D volumes and synchronize timelapses. First a parallel geometry acquisition (standard z-slice acquisition) [10, 11] was proposed, adapted from a confocal microscopy volume reconstruction technique [12, 13] previously developed. However, this technique is susceptible to drift. It was further improved [14] to reduce drift, but requires the acquisition of dense OCT volumes, i.e. much more data. An alternative acquisition method was proposed with radial geometry [15], where time-lapses are acquired radially around a central rotation line, which is used as a reference for realignment. However, this technique requires a custom setup as the images are acquired radially instead of parallel. Finally, the two ideas were combined to propose a parallel geometry acquisition of two datasets rotated perpendicularly [16]. The two datasets can be easily realigned as they have many reference points along the common central line, with the downside of needing twice the data. However, if OCT reveal the tissue morphology [17, 18, 19], it does not allow for single-cell tracking due to a lack of spatial resolution. OCT is widely used in mouse cardiac development imaging as the penetration depth is typically 1-3 mm [20] contrarily to, for instance, a confocal microscope (maximal depth of  $\sim 100 \mu\text{m}$ , limited by light scattering). The current limit for multi-photon microscopy penetration depth is a 500-600  $\mu\text{m}$  [21, 22].

In light-sheet microscopy, Mickoleit *et al.*, 2014 [23] also used perpendicular sequences to reconstruct high temporal resolution 3D heart image volumes. Their registration method to reconstruct the dynamic 3D heart is based on image similarity, calculating the Pearson correlation coefficient between full periods in movies of adjacent planes. As for the OCT,

this method requires the acquisition of twice the data. Trivedi *et al.*, 2015 [24] combined an optimized retrospective image registration protocol with two-photon excitation SPIM, for a high penetration depth and high imaging speed. They do not however address the problem of drift. Recently, Greer *et al.* [25] proposed a high-speed light-sheet microscope with parallel image acquisition on multiple cameras for a volume imaging rate of 40Hz. This setup does reach the required temporal resolution for volumetric acquisition, but requires to either have access to it or to build it.

In Chapter 5, I consider the problem of building smooth time-lapse sequences in the cardiac phase versus development or cardiac phase versus imaging depth spaces based on a set of still images captured at weakly-constrained times within the heartbeat cycle and over the course of development or at various depths in the heart. This method determines a smooth path in cardiac phase-development or depth space enforcing neighborhood similarity via a within-stage (or within-depth) sorting followed by a cyclical least-squares phase alignment approach that I formulated as a mixed integer linear problem. Constraining the paths of time-lapses by providing key-points together while enforcing local similarity successfully stabilizes the excursion error from which recursive registration approaches suffer.

In Chapter 6 I discuss the relative merits of the solutions proposed in this thesis. Given the multi-disciplinary nature of this thesis, for the convenience of the reader, I have provided short references to some of the microscopy techniques mentioned in this thesis in the Appendix A.1. In Appendix A.2 you will find a brief overview of the zebrafish heart development that should give some context to the experimental data I show in this thesis.





## 2 Sorting of periodic time-series

This Chapter is adapted from our paper Mariani *et al.*, 2019 [26]. We present a method to reconstruct an image sequence covering one heartbeat from images acquired over multiple cardiac cycles, with each image triggered at an arbitrary time, by sorting them according to their similarity. We formulate this task as a traveling salesman problem for which efficient solutions are available. We characterized our approach by evaluating its accuracy on synthetically generated data and sub-sampled high-speed movies of the beating heart in zebrafish larvae. We found that reconstructions are reliable when each phase produces a distinct image and when there are no abrupt cardiac motions, which amounts to collecting at least 100 images in a typical microscopy imaging scenario. We finally demonstrate that our method can be applied on data acquired with a fast confocal microscope, increasing its limited frame-rate by a factor 8.

### 2.1 Virtual High-Framerate Microscopy of the Beating Heart via Sorting of Still Images

Line scanning confocal microscopy [13], spinning disk microscopes (in some cases with strobed illumination [27]), or light sheet microscopes [28, 29, 30], allow for fast framerates but are still limited by data-transfer bandwidth. Several techniques have been proposed to build movies from image series acquired over multiple cycles of periodic processes when direct acquisition with a sufficient frame-rate was not possible. Zhang *et al.* [4] proposed to post-process MRI images of the beating heart acquired without gating in free-breathing subjects by learning the cardiopulmonary manifold formed by the images. This allowed them to sort the images over two axes, that they linked to the cardiac and the respiratory phases, respectively. Tralie *et al.* [3] used a tracking-free Eulerian approach for synthesizing slow motion videos from videos of multiple periods of a repetitive motion. In astronomy, techniques to assemble data acquired during irregularly-spaced observations to determined revolution periods [31, 32] inspired methods to determine the period in cardiac microscopy [13] and to virtually increase the framerate in cardiac optical coherence tomography [33].

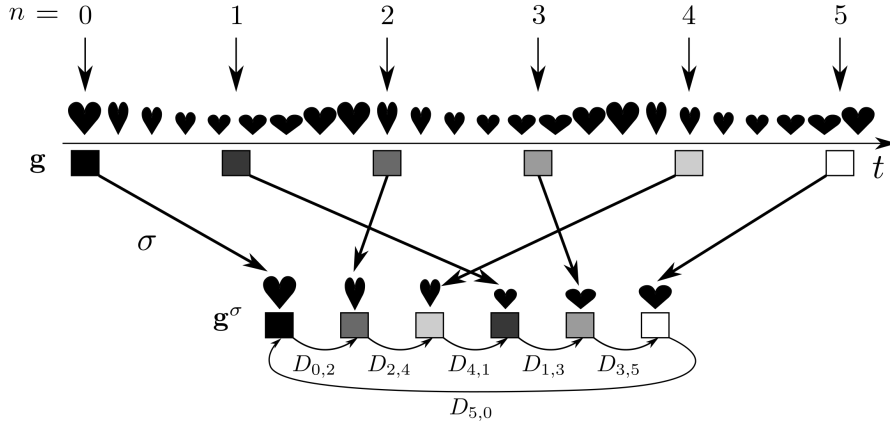


Figure 2.1 – Images of the beating heart are acquired at arbitrary phases of the cardiac cycle. We sort the acquired images such as to minimize the image-to-image distance  $D_{k,\ell}$  between consecutive images, a task that we identify as a traveling salesman problem.

However, the latter methods assume the underlying process is strictly periodic and that the acquisition time-stamps are known, which limits applicability and robustness.

In this Chapter, we propose a method that takes microscopy images of the beating heart, each triggered at an arbitrary time, and virtually increases the time resolution by sorting them to form a complete heartbeat (Fig. 2.1). The novel contributions in this Chapter are threefold. First, in Section 2.2 we formulate the task of sorting cardiac images as a traveling salesman problem for which efficient algorithms are available and whose output is a direct solution to the ordering problem (rather than a manifold projection). Second (in Section 2.3), we characterize our method on synthetic and experimental data. Third, we show an application to increase the framerate in an imaging modality, fluorescence microscopy, for which fast imaging is particularly challenging and which may therefore benefit from our method (Section 2.3). In Section 2.4, we discuss the performance and limitations of our method and conclude.

## 2.2 Methods

### 2.2.1 Imaging Model and Problem Statement

We consider a time-varying two-dimensional image  $f(x, y, t)$  with  $(x, y)$  the spatial position and  $t$  the time. The image intensity varies periodically with a period  $T$ , such that:

$$f(x, y, t) = f(x, y, t + T) \quad \text{for all } t \in \mathbb{R}. \quad (2.1)$$

We denote by  $\mathbf{f}$  the image series covering one heartbeat:

$$\mathbf{f}[k, \ell, n] = f(k\Delta_x, \ell\Delta_y, n\Delta_t), \quad (2.2)$$

where  $\Delta_x$  and  $\Delta_y$  are the pixel width and height, respectively,  $(k, \ell) \in \mathcal{K} = \{0, \dots, K-1\} \times \{0, \dots, L-1\}$  are the row and column index pairs,  $n \in \mathcal{N} = \{0, \dots, N-1\}$  denotes the time frame index, and  $\Delta_t = \frac{T}{N}$  the time interval.

Given that  $\Delta_t$  must be small (to achieve sufficient temporal resolution), it is typically not possible to acquire  $\mathbf{f}$  directly. Instead, we consider the image series  $\mathbf{g}[k, \ell, n]$ ,  $(k, \ell) \in \mathcal{K}$ :

$$\mathbf{g}[k, \ell, n] = f(k\Delta_x, \ell\Delta_y, t_n), \quad (2.3)$$

where  $t_n$ ,  $n \in \mathcal{N}$ , denotes the times at which the frames were acquired. These times occur at arbitrarily-spaced times with:  $t_0 < \dots < t_n < \dots < t_{N-1}$ , and  $t_n \in \mathbb{R}$ .

The image reconstruction problem we address is obtaining an estimate  $\tilde{\mathbf{f}}$  of the uniformly sampled image sequence  $\mathbf{f}$  given the measurements  $\mathbf{g}$ , without knowledge of the underlying heartbeat period  $T$  nor the starting times  $t_n$ .

### 2.2.2 Virtual Frame-Rate Improvement via Sorting

The key insight for reconstructing  $\tilde{\mathbf{f}}$  is that the underlying signal  $f$  is repeating and that, as we collect sufficient frames to build the data  $\mathbf{g}$  (i.e.  $N$  sufficiently large), we eventually capture the heart in all its poses, under the assumption that acquisitions occur at arbitrary times, unrelated to the period  $T$ . We further assume that the heart takes up poses that are distinct for each phase of the heartbeat and that only small changes are required to transform one image into the next. We propose to estimate  $\tilde{\mathbf{f}}$  by sorting the frames  $\mathbf{g}[:, :, n]$ ,  $n \in \mathcal{N}$ .

We define the cardiac phase  $\phi_n$  of the  $n^{\text{th}}$  frame  $\mathbf{g}[:, :, n]$  as the wrapping operation:

$$\phi_n = \mathcal{W}_T(t_n) = t_n + mT, \quad m \in \mathbb{Z} \text{ s.t. } \phi_n \in [0, T). \quad (2.4)$$

The task of sorting the frames is equivalent to finding a permutation  $\sigma : \mathcal{N} \rightarrow \mathcal{N}$ ,  $m \mapsto n = \sigma(m)$  such that the phases  $\phi_{\sigma(0)}, \dots, \phi_{\sigma(N-1)}$  are in increasing order:

$$\phi_{\sigma(0)} \leq \dots \leq \phi_{\sigma(N-1)}. \quad (2.5)$$

Given the sequence  $\mathbf{g}$ , we denote by  $\mathbf{g}^\sigma$  a permuted frame sequence obtained by applying the permutation  $\sigma$  to  $\mathbf{g}$ :

$$\mathbf{g}^\sigma[:, :, m] = \mathbf{g}[:, :, \sigma(m)], \quad m \in \mathcal{N}. \quad (2.6)$$

We formulate the phase-ordering problem as a minimization task where we seek a permutation that minimizes the frame-to-frame image difference between neighboring frames. We define the cost of a given candidate permutation  $\sigma'$  (with  $\sigma'(t_0) = 0$ ) as:

$$C(\mathbf{g}, \sigma') = \sum_{m=0}^{N-2} d\left(\mathbf{g}^{\sigma'}[:, :, m], \mathbf{g}^{\sigma'}[:, :, m+1]\right) + d\left(\mathbf{g}^{\sigma'}[:, :, N-1], \mathbf{g}[:, :, 0]\right), \quad (2.7)$$

where the frame-wise distance operator  $d(\cdot, \cdot)$  between two 2D frames  $\mathbf{x}$  and  $\mathbf{y}$  is defined as:

$$d(\mathbf{x}, \mathbf{y}) = \sum_{k=0}^{K-1} \sum_{\ell=0}^{L-1} |\mathbf{x}[k, \ell] - \mathbf{y}[k, \ell]|. \quad (2.8)$$

The permutations that lead to a minimal cost come in pairs (given that the image distance is symmetrical):

$$\{\tilde{\sigma}^T, \tilde{\sigma}\} = \underset{\sigma' \in S_{N-1}}{\operatorname{argmin}} C(\mathbf{g}, \sigma'), \quad (2.9)$$

where  $\tilde{\sigma}$  is the ordering that satisfies Eq. (2.5), and  $\tilde{\sigma}^T$  the same permutation in reverse order. We identify Problem (2.9) as an incarnation of the traveling salesman problem (TSP): the permutation we seek corresponds to finding a path that visits each image (and comes back to the starting image) while minimizing the distance traveled between adjacent images. Since there are  $(N-1)!$  possible frame permutations (the first frame is fixed) exploring all combinations would be prohibitively expensive. Instead, we use the TSP solver package Concorde [34], with the linear programming solver QSOPT [35]. It takes an  $N \times N$  (symmetrical) table  $\mathbf{D}$ , whose entries  $D_{j,k} = d(\mathbf{g}[:, :, j], \mathbf{g}[:, :, k])$  contain the frame-wise distances between all frame pairs. The computational complexity of the Concorde solver is  $\mathcal{O}(a \cdot b^{\sqrt{N}})$ , with  $a = 0.21$  and  $b = 1.24194$  [36, 37]. To build the table  $\mathbf{D}$  efficiently and robustly, we spatially-average and downsample each frame  $\mathbf{g}[:, :, n]$ ,  $n \in \mathcal{N}$  before computing the image distances.

## 2.3 Results

### 2.3.1 Method Characterization on Synthetic Data

To characterize the accuracy of the sorting process as a function of the number of available frames, we produced synthetic data of a ring contracting periodically and asymmetrically [13] over multiple periods. We selected  $N \in \{10, 20, \dots, 300\}$  frames, whose temporal phases were drawn from a uniform distribution, and applied our sorting algorithm. To quantify the sorting accuracy, we defined the score:

$$\bar{\mathcal{E}} = \left| \frac{1}{N} \sum_{n=0}^{N-1} \mathcal{E}[n] \right|, \text{ with} \quad (2.10)$$

$$\mathcal{E}[n] = \begin{cases} 1 & \phi_{\tilde{\sigma}(n)} < \phi_{\tilde{\sigma}(\langle n+1 \rangle_N)} \\ 1 & \phi_{\tilde{\sigma}(n)} = \phi_{\max} \text{ and } \phi_{\tilde{\sigma}(\langle n+1 \rangle_N)} = \phi_{\min} \\ -1 & \text{otherwise,} \end{cases} \quad (2.11)$$

where  $\phi_{\min}$  and  $\phi_{\max}$  are the minimal and maximal ground truth phases, respectively and  $\langle n \rangle_N = n \bmod N$ . When correctly sorted, the phases should be in a strictly increasing or decreasing order, with a single jump between the minimal and maximal phases  $\phi_{\min}$  and  $\phi_{\max}$ . We have  $0 \leq \bar{\mathcal{E}} \leq 1$ , with a low score expressing poor and a high score expressing correct sorting (the score does not penalize the direction). We observed that the sorting is unreliable below

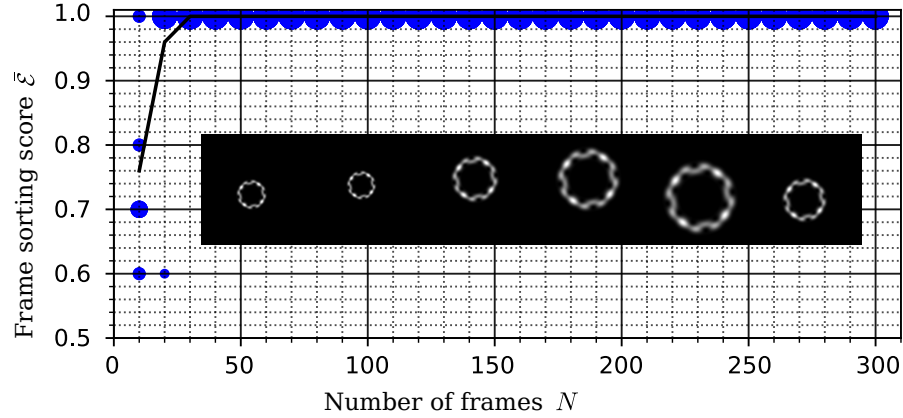


Figure 2.2 – Cardiac image sorting score as a function of the number of available images  $N$ . Frames were selected from a synthetic image series ( $K = L = 256$ ) with phases drawn randomly from a uniform distribution (10 realizations per experiment). The sorting is near perfect for  $N \geq 100$ .

$N = 30$  frames, then stabilizes toward the best score as  $N$  increases. In additional experiments (not shown), we synthesized a motion that did not produce unique images for different phases (breaking an assumption for our method to perform correctly), which produced unpredictable sorting results (e.g. inverting segments in time between similar images).

### 2.3.2 Validation on Experimental Measurements

We bred wild type as well as transgenic  $Tg(myl7:membranemCherry)$  [38] zebrafish according to standard procedures [39]. The latter express red fluorescent protein in the muscle cells of the atrium. All procedures were authorized by the Institutional Animal Care and Use Committee at the University of California, Santa Barbara (wild-type) and the Cantonal Veterinary Office, Bern. Briefly, we grew the zebrafish embryos in E3 medium and added PTU (0.003% 1-phenyl-2-thiourea) to avoid pigmentation when the embryos reached an age of 24 hours post fertilization (hpf). At an age of 36 hpf, we removed the chorion surrounding the embryos with forceps and anesthetized the embryos with Tricaine at 0.08 mg/ml, pH 7. We embedded the embryos with the ventral side down on a glass bottom dish in 1% low melting agarose.

#### Validation on high-speed data of the heart

We imaged the wild type heart at 55 hpf on a Leica DMR microscope equipped with a FASTCAM SA3 camera, using transmission, at a frame rate of 1,000 fps. We collected a 32,001-images dataset which covered about 76 heartbeats. We identified the first 380 frames (covering 0.38 s) as a ground truth heartbeat, which we averaged pairwise to form a sequence of  $N = 190$  frames. Next, we randomly selected  $N = 190$  frames among the full dataset with indices drawn from a uniform distribution over the entire dataset, simulating a slow acquisition procedure. We next applied our sorting method and compared it with the 190 frames of the ground truth

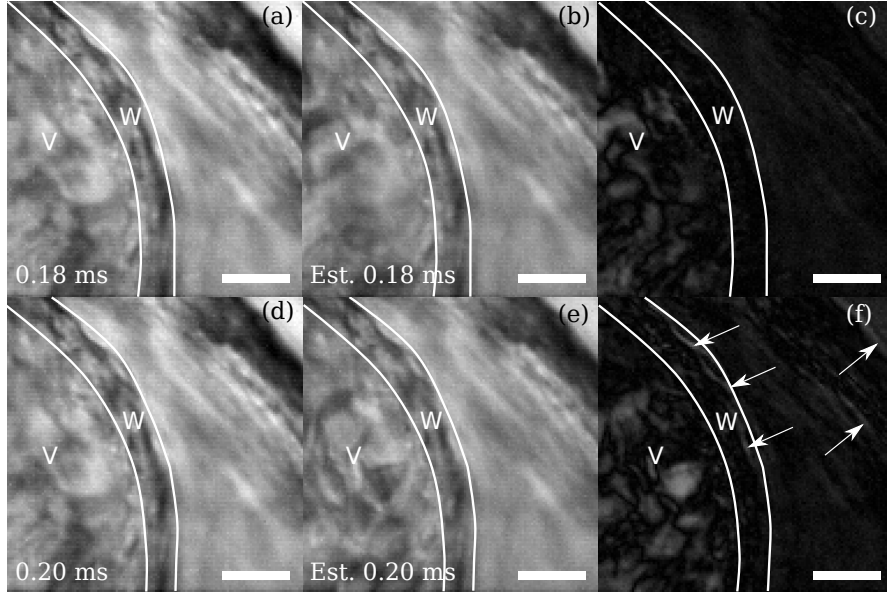


Figure 2.3 – Sorting evaluation on experimental data. (a),(d) Two frames from a 190 frame high-speed sequence of the beating zebrafish heart, acquired at 1000 fps (ground truth). (b),(e) Corresponding frames obtained by sorting 190 randomly drawn from a 32,001-frame high-speed sequence. (c),(f) difference between ground truth and reconstruction. V: ventricle, W: heart wall. Arrows in (f) indicate areas of mismatch. Scale bar is 100  $\mu\text{m}$ . See also Chapter 2 Supplementary Movie part 1 ([00:00-00:14]).

period (Fig. 2.3). The periodic parts of the ground truth and reconstructed images agree, demonstrating the correct ordering in experimental data. However, the red-blood cells, which are different from one heart-beat to the next differ.

### Virtual Framerate Increase in Fluorescence Microscopy

To demonstrate the potential of our method for limited framerate modalities, we imaged the heart of the 36 hpf old Tg(myl7: membranemCherry) zebrafish on a Zeiss LSM880 inverted confocal microscope with an LD C-Apochromat 40 $\times$ /1.1 NA water immersion objective lens, in fluorescence, at 26.3 fps. We collected 100 frames. We applied our method to virtually increase the framerate by sorting all 100 frames into one single period (Fig. 2.4). Given the observed heartbeat covered 13 frames in the original dataset, the virtual frame achieved was 202 fps, a 7.7-fold increase. Note that only the framerate (not the temporal resolving power) is increased.

## 2.4 Discussion and Conclusion

Our sorting approach reaches a good accuracy when  $N \geq 100$ . In particular, the standard deviation becomes smaller with an increasing  $N$ , with a mean around 99%. Our method has

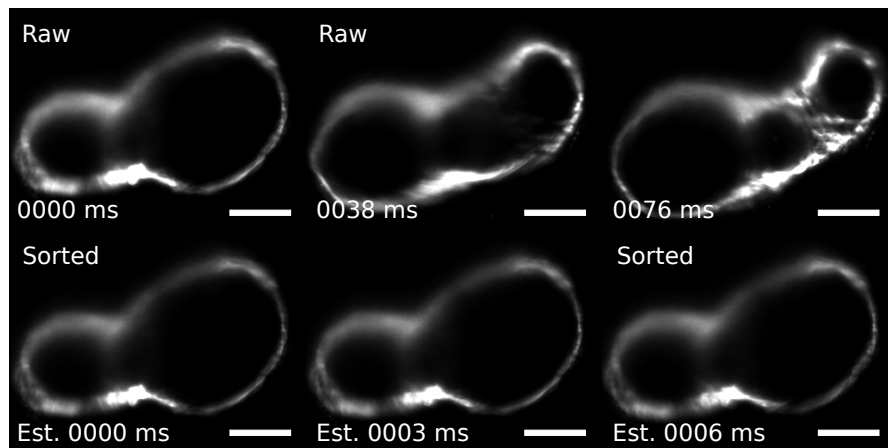


Figure 2.4 – Virtual framerate increase (202 fps) via sorting of 100 frames across about 8 heartbeats acquired at 26.3 fps on a confocal microscope. Top row: three consecutive frames from raw sequence. Bottom row: three consecutive frames after virtual framerate increase. Scale bar is 50  $\mu\text{m}$ . See also Chapter 2 Supplementary Movie part 2 ([00:15-00:40]).

two limitations. First, it requires that the sampling be unrelated to the cardiac period (to avoid stratified sampling) which is typically the case because the heart exhibits variations from one heartbeat to the next. Second, the signal must be asymmetric. For instance, imaging just a part of the cardiac heart wall or downsizing the signal too much can lead to a loss of asymmetry in the signal and failure to reconstruct the correct order. We will address this issue in Chapter 3. Artificially increasing the framerate of an image series is particularly promising for modalities that have too slow a framerate or whose writing bandwidth is insufficient or irregular.





## 3 Structured illumination to create asymmetry in the data

This chapter was adapted from our publication submitted to ISBI 2021.

However, while collections of still images of the beating heart at arbitrary phases can be sorted to obtain a virtual heartbeat, the presence of identical heart configurations at two or more heartbeat phases can derail this approach, as discussed in Chapter 2. Here, we propose a dual illumination method to encode movement in alternate frames to disambiguate heartbeat phases in the still frames. We propose to alternately acquire images with a ramp and pulse illumination then sort all successive image pairs based on the ramp-illuminated data but use the pulse-illuminated images for display and analysis. We characterized our method on synthetic data, and show its applicability on experimental data and found that an exposure time of about 7% of the heartbeat or more is necessary to encode the movement reliably in a single heartbeat with a single redundant node. My method opens the possibility to use sorting algorithms without prior information on the phase, even when the movement presents redundant frames.

### 3.1 Unequivocal cardiac phase sorting from alternating ramp- and pulse- illuminated microscopy image sequences

Live imaging of organ development is an essential tool to study the beating heart in zebrafish. However, imaging is challenging because the heart is beating starting from early stages of development and requires a fast acquisition frame rate. Fluorescence microscopy is particularly affected as fairly long exposure times are necessary or camera speed and data-transfer bandwidth are limited.

An attractive alternative to increasing the frame rate is to process a series of still images acquired at a slow (compared to the heartbeat) or even irregular frame rate. Several computational solutions to then sort the images into a virtual sequence that depicts the beating heart have been previously proposed [26, 3, 4]. While these methods do not require prior phase information they fail to reconstruct accurate motions when the heart follows a motion, within

one heartbeat, that results in two or more identical configurations as multiple equivalent solutions exist (Fig. 3.1(a)–(d), left column). While the acquisition cameras are often already pushed to their speed limit, microscopy offers complete control of the illumination, which affords much more flexibility and fewer temporal constraints. Patterned illumination has been employed effectively to imprint a spatial pattern in structured illumination (spatial) super-resolution microscopy[6] or a sub-frame *temporal* pattern to improve the temporal resolution [7] and sampling [8]. Here, we propose to take advantage of an acquisition scheme where we alternate frames in which the heart is illuminated by a single short pulse [27] and frames in which it is illuminated by a temporally asymmetric ramp pattern (Fig. 3.1(e)). Thereby, heart configurations that appear identical in still frames but differ in their motion can be distinguished based on their differing motion blur in the ramp-illuminated frames (Fig. 3.1(a)–(d) right column).

In Section 3.2, we formally describe the proposed image acquisition protocol. In Section 3.3, we characterize our method in several illumination scenarios using synthetic data and demonstrate the feasibility of our method using an Arduino Uno, an open-source microcontroller board, with our OpenSPIM [40] microscope on fluorescence data of the beating heart. In Section 3.5, we discuss the performance and limitations of our method and conclude.

## 3.2 Methods

### 3.2.1 Imaging model and problem statement

We consider an image series of a sample that moves periodically, with a period  $T$ :

$$f(x, y, t) = f(x, y, t + T), \quad (3.1)$$

where  $x, y$  are the sample coordinates and  $t$  the time. We further assume that the motion contains a crossing point, as shown in Fig. 3.1 (a), that is, two times  $t_a$  and  $t_b$ ,  $0 \leq t_a < t_b < T$ , where the heart takes the same shape:

$$f(x, y, t_a) = f(x, y, t_b). \quad (3.2)$$

Our goal is to reconstruct an estimate of the discrete image series covering one period:

$$\mathbf{f}[k, \ell, n] = f(k\Delta x, \ell\Delta y, n\Delta t) \quad (3.3)$$

where  $\Delta x$  and  $\Delta y$  are the pixels width and height, and  $(k, \ell) \in \{0, \dots, K\} \times \{0, \dots, L\}$  the row and column index pairs,  $n \in \{0, \dots, N-1\}$  the time frame index, and  $\Delta t = T/N$  a time interval. As

input, the reconstruction takes a series of  $N$  image pairs  $(\mathbf{g}_p[:, :, n], \mathbf{g}_r[:, :, n])$  acquired as:

$$\mathbf{g}_r[k, \ell, n] = \int_{t_n}^{t_n+a} r(t - t_n) \cdot f(k\Delta x, \ell\Delta y, t) dt \quad (3.4)$$

$$\mathbf{g}_p[k, \ell, n] = \int_{t_n+a}^{t_n+a+\Delta_p} f(k\Delta x, \ell\Delta y, t) dt \quad (3.5)$$

where  $t_n$ ,  $0 \leq n < N$  is the frame acquisition time, occurring at arbitrary phases of the signal and  $r(t)$  is an illumination intensity function that follows a ramp pattern composed of  $N_a$  discrete steps:

$$r(t) = i_r \frac{\left\lfloor t \frac{N_a}{a} + 1 \right\rfloor}{N_a} \quad (3.6)$$

where  $i_r$  is the maximal intensity value of the ramp. The  $\mathbf{g}_p[:, :, n]$  correspond to frames acquired with an illumination pulse of duration  $\Delta_p$ , just following the previous ramp frame. Since the integral of this ramp over the interval of duration  $a$  is  $\frac{N_a+1}{N_a} a i_r / 2$  and that of the pulse  $i_p \Delta_p$ , we adjust the ramp intensity  $i_r$  such as to achieve similar exposure levels in the pulse and ramp frames:

$$i_r = i_p \frac{2\Delta_p}{a} \frac{N_a}{N_a + 1}. \quad (3.7)$$

### 3.2.2 Phase-sorting ramp-, pulse-illuminated image pairs

Since the ramp- and pulse-illuminated image pairs are acquired at nearby times, we can assume that the phase of the ramp-illuminated images are all offset by a constant (equal to  $a$ ) when compared to the phase of their corresponding pulse-illuminated frame. We therefore propose to apply a phase-sorting method to the ramp-illuminated images  $\mathbf{g}[:, :, n]$ ,  $0 \leq n < N$ , thereby obtaining a frame permutation  $\sigma : \{0, \dots, N-1\} \rightarrow \{0, \dots, N-1\}$ ,  $n \mapsto \sigma(n)$  (using a traveling salesman method that minimizes the absolute image difference between consecutive frame pairs, which we previously described [26]). Since the ramp-illuminated images contain motion blur, heart configurations that would lead to ambiguous still frames do no longer confuse the method. However, since the blur is detrimental to any further image analysis, we apply the permutation  $\sigma$  to the sharp, pulse-illuminated sequence to obtain the estimated sequence:

$$\tilde{\mathbf{f}}[:, :, n] = \mathbf{g}_{\text{pulse}}[:, :, \sigma(n)]. \quad (3.8)$$

## 3.3 Results and Discussion

### 3.4 Optical flow trajectories of sorted data

To test our proposed acquisition procedure, we simulated synthetic data of a beating heart [12]. We simulated a deformation pattern that roughly resembles a figure-eight deformation pattern, with two phases within one heartbeat in which the heart has the same shape (Fig. 3.1

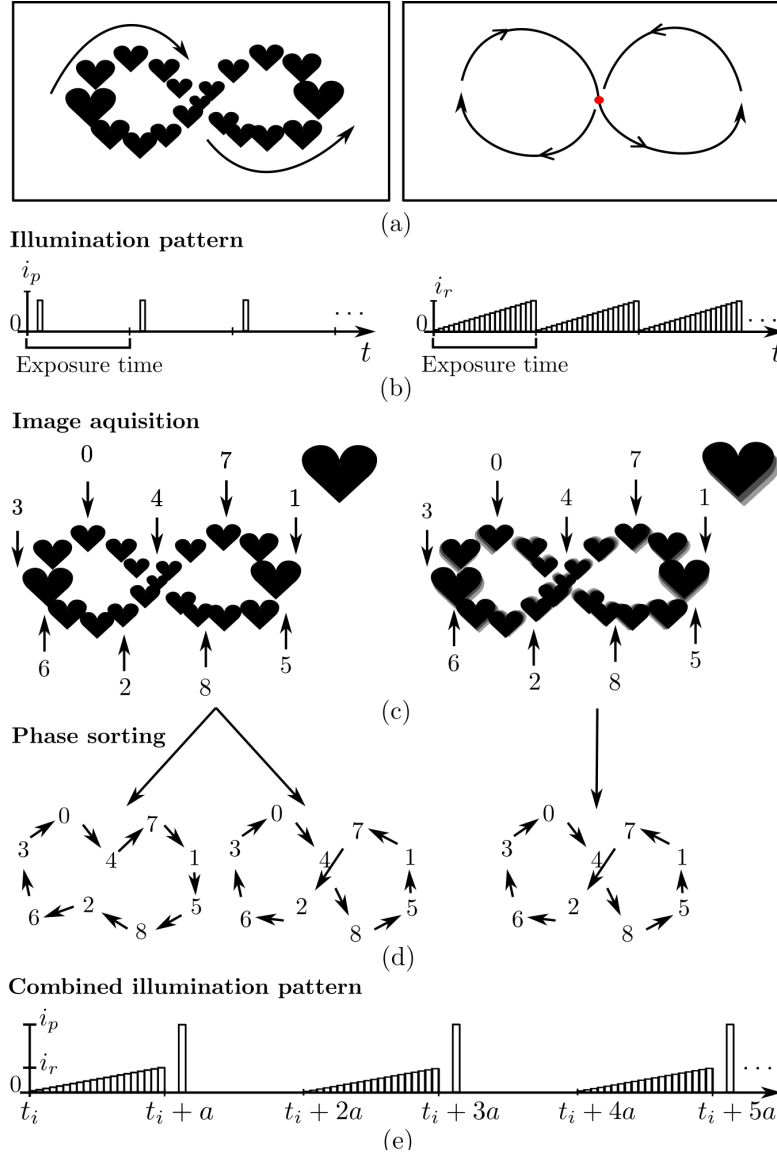


Figure 3.1 – Structured illumination pattern removes sorting ambiguity. (a) The object movement trajectory is an eight-shaped and periodic. The red dot (on the right) indicates a position appearing twice in the period. (b) Illumination patterns. Left: Pulse illumination, during a fraction of the camera exposure time. Right: Ramp illumination, with increasing intensity during the whole exposure time. (c) Left: The pulse illumination leads to a sharp image. Right: The ramp illumination pattern creates a movement blur in the image. (d) Left: The image sorting process can lead to two different results, as the center of the eight-shaped movement is a point of symmetry. Right: The structured illumination removes the central point ambiguity thanks to the movement blur. (e) We propose an alternating illumination pattern, where the ramp-illuminated images are used to sort the pulse-illuminated images.

(a)) but not the same velocity. We simulated the acquisition of  $N = 240$   $256 \times 256$ -pixel frames, 120 for each illumination method. The period was  $T = 6\pi \cdot N_a$  and with the number of ramp

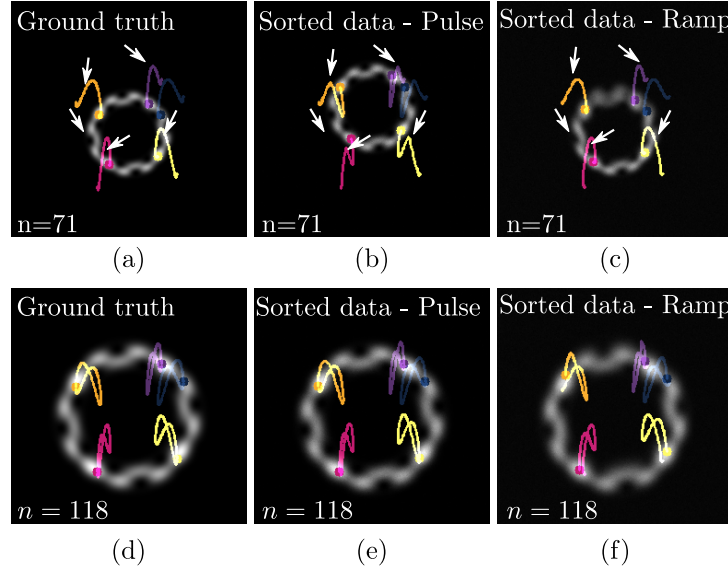


Figure 3.2 – Simulation of a periodic signal containing a symmetry node. The acquisition time was 9.3% of the signal period. The colored lines are the trajectories of keypoints, forming an eight-shaped trajectory with a symmetry points shown by the arrows. (a)–(c) Frame  $n = 71$ . (a) Ground truth data, with the expected trajectories. (b) Sorted data of the simulated acquisition with a short pulse. The correct sorting path was missed at the symmetry point. (c) Sorted data of the simulated acquisition with a ramp illumination. The sorting was successful, as the ramp eliminated the ambiguity at the symmetry node. (d)–(f) Last frame  $n = 118$ . The complete trajectories shown in (d)–(f) all have the same final shape, showing that the error is indeed only located at the symmetry node. See Chapter 3 Supplementary Movie [00:00-00:25]

steps set to  $N_a = 20$  we combined frames such as to end up with a period of  $T = 6\pi$  in the final simulated sequence. We further added background intensity and finally considered each pixel to be a realization of a Poisson process. We additionally simulated a ground truth sequence.

We then sorted both the ramp- and pulse-illuminated data. The sorted pulse-illuminated data followed a path different from the ground truth whereas the ramp-illuminated data yielded the correct motion. To better visualize the paths, we tracked keypoints on the image sequences (using the OpenCV implementation of the Lucas-Kanade optical flow method [41] and selected keypoints with the good feature to track method [42]). Fig. 3.2 shows the trajectories of five points in the ground truth (Fig. 3.2 (a) and (d)), sorted pulse-illuminated (Fig. 3.2 (b) and (e)), and ramp-illuminated (Fig. 3.2 (c) and (f)) sequences. The arrows in Fig. 3.2 (a), (b), and (c) point towards the point in the data where the trajectories cross. The ground truth (Fig. 3.2 (a)) and ramp-illuminated (Fig. 3.2 (c)) data show the correct eight-shaped trajectory. The pulse-illuminated (Fig. 3.2 (b)) data shows the alternative bow-tie-shaped trajectory. Fig. 3.2 (d), (e), and (f) shows that the complete trajectories for the ground truth (Fig. 3.2 (d)), pulse-illuminated (Fig. 3.2 (e)) and ramp-illuminated (Fig. 3.2 (f)) data is the same. See also Chapter 3 Supplementary Movie [00:00-00:25].

### 3.4.1 Ground truth phases of sorted data

In order to characterize the requirements on the ramp length required to disambiguate the signal, we simulated 5 sequences of different ramp duration (exposure time as compared to the duration of one heartbeat) together with the corresponding pulse illumination. We sorted the data and plotted the sorted ground truth phases in Fig. 3.3. To make the data more readable, we shifted the phases for each sequence such that the minimal phase is at frame  $n = 0$ . The phases should be in increasing order. Fig. 3.3 (a) shows the sorted phases of the pulse-illuminated data. Discontinuities in phases (marked by circles) occur at the repeat motion crossing points and show that the sequences are sorted incorrectly. Fig. 3.3 (b) shows the sorted phases of the ramp-illuminated data. An exposure time  $a < 0.066 T$  leads to errors in sorting (circles), showing that there was not enough shaded blur to encode direction.

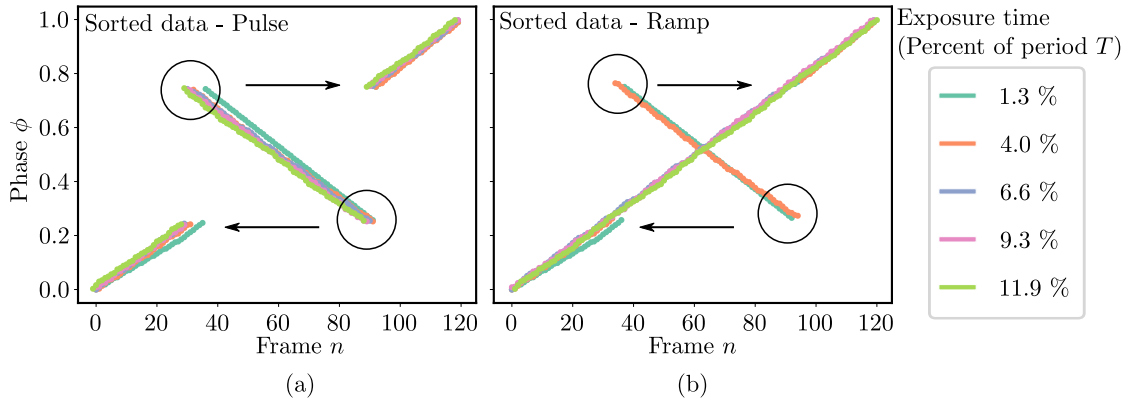


Figure 3.3 – Characterization of the acquisition time  $a$  required to disambiguate the signal in percent of period  $T$ , shown as numbers in the graph legends. (a) Phases of the pulse acquisition sorted according to the sorting results of the pulse acquisition simulation. The sorting was not successful at the symmetry point (circles), as can be seen by the discontinuity and change in direction of the phase. The arrows point toward the correct phase position. (b) Phases of the ramp acquisition sorted according to the sorting results of the ramp acquisition simulation. The sorting was successful when the ramp acquisition time  $a$  was longer or equal to 6.6% of the signal period and unsuccessful for shorter ramps as can be seen by the discontinuity in the phases (circles).

### 3.4.2 Application on experimental data

We finally tested whether our method could be implemented in an experimental setting without adversely affecting the image quality. We bred transgenic zebrafish Tg(actb2:LIFEACT-RFP) [43], which express red fluorescent proteins that bind to F-actin fibers. We collected embryos that we grew in E3 medium with added PTU (0.003% 1-phenyl-2-thiourea) at age 24 hours post fertilization (hpf) to avoid pigmentation. At 48 hpf, we anesthetized the hatched embryos with Tricaine at 0.08 mg/ml, pH 7. We embedded the embryos with the anterior side (head) down in a fluorinated ethylene propylene tube in 1% low melting agarose (Promega). We imaged the heart on a OpenSPIM [40] microscope with an UMPLFLN 20XW semi-apochromat

water dipping objective lens. We imaged the heart across the ventro-dorsal plane.

We used an Arduino Uno to control the laser illumination pattern and MicroManager [44] to control the camera of our OpenSPIM [40] as well as the image acquisition itself. We set the exposure time to  $a = 70\text{ms}$  for the ramp with  $N_a = 8$  steps, and the pulse exposure time to  $t_p = 4\text{ms}$ . We added a delay of 10ms between the image pairs due to hardware limitations. We sorted the ramp-illuminated data and applied the solution to the pulse-illuminated data. Fig. 3.4 shows the acquisition of a beating zebrafish embryo heart with our alternating illumination. Fig. 3.4 (a) shows an image acquired with the ramp illumination, and Fig. 3.4 (b) shows the image acquired with the pulse illumination. The arrows point toward single cells that can be seen in the pulse-illuminated image but cannot be seen in the ramp-illuminated image due to motion blur. The acquired data can be seen in Chapter 3 Supplementary Movie [00:26-00:58], and the sorted data can be seen in Chapter 3 Supplementary Movie [00:59-01:12].

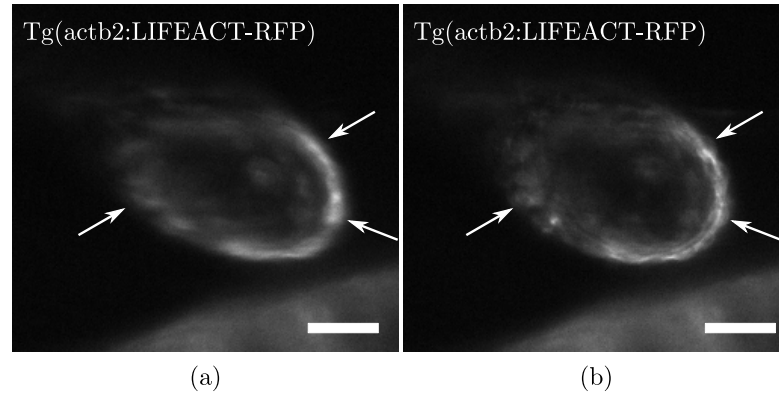


Figure 3.4 – Beating zebrafish heart acquired using alternating structured illumination. (a) Image acquired with a 70ms ramp illumination. (b) Image acquired with a 4ms pulse. The arrows point toward single cells that are visible in the pulse-illuminated data, but cannot be seen in the blurred ramp-illuminated data. Scale bar is  $30\mu\text{m}$ . See Chapter 3 Supplementary Movie [00:26-00:58] and [00:59-01:12]

### 3.5 Conclusion

Our method allows sorting still images of the beating heart even when it contains repeat shape configuration, without prior phase information, simply by encoding the movement in every other image with shaded motion blur through ramp illumination. We showed that the ramp illumination duration should be around 7% or longer than the signal period. We showed its applicability by implementing the proposed structured illumination patterns on the Arduino Uno open source microcontroller and showed the shaded motion blur on alternating images of the acquired data. Our method requires the implementation of a custom illumination pattern and the synchronization with a camera.





## 4 Scanning aberrations correction

This Chapter was adapted from our paper Mariani *et al.*, 2020 [45].

Laser scanning microscopes (LSM) are limited when used to study dynamic heart morphology or function. Despite their ability to resolve static cardiac structures, the fast motion of the beating heart introduces severe artifacts in the scanned images and gating the acquisitions to the heartbeat is difficult to implement on traditional microscopes. Furthermore, although alternative high-speed imaging instruments exist, they are not widely available (due to cost or hardware complications), putting dynamic cardio-vascular imaging off-limits for many researchers. Here, we propose a method that allows imaging the beating heart on conventional LSMs. Our approach takes a set of images containing scanning aberrations, each triggered at an arbitrary time in the cardiac cycle, and assembles an image sequence that covers a single cardiac heart beat. The steps are: (i) frame sorting by solving a traveling salesman problem (see Chapter 2); (ii) heartbeat duration estimation; and (iii) scan-delay compensation via space-time resampling. We characterize the performance of our method on synthetic data under several light intensities and scanning speeds. We further illustrate our method's applicability on experimental images acquired in live zebrafish larvae, and show that the reconstruction quality approaches that of fast, state-of-the-art microscopes. Our technique opens the possibility of using LSMs to carry out studies of cardiac dynamics, without the need for prospective gating or fast microscopes.

### 4.1 Reconstruction of image sequences from ungated and scanning-aberrated laser scanning microscopy images of the beating heart

*In vivo* microscopy is an essential tool to study organ development at the cellular level in embryos of animal models. In zebrafish, whose embryos and larvae are mostly transparent, most organs can be directly viewed under a light microscope.

In particular, it is possible to observe the developing zebrafish heart, whose early developmental stages are very similar to the ones in humans. Nevertheless, high-resolution and

depth-resolved cardiac imaging are hampered by the rapid beating of the heart. This limitation is especially important when acquiring images with a laser-scanning microscope (LSM; e.g. a confocal LSM, two-photon LSM, etc.). Laser scanning microscopy techniques, which allow optical sectioning, are widely used because of the many advantages they offer. These include high spatial resolution, possibility of acquiring images in arbitrary regions of interest, common availability of LSMs in imaging centers, and existence of many established and LSM-compatible sample mounting protocols. The limitation of LSMs, when imaging the heart, is the scanning procedure, which has contradicting requirements. The speed should ideally be high enough to avoid compromising the temporal resolution of heartbeats, yet slow enough to collect dim light and achieve acceptable signal-to-noise ratio (SNR). Naive imaging of the zebrafish heart leads to aberrations of two forms: first, the slow scanning speed creates scanning aberrations because the heart beats during the acquisition of a single image (Fig. 4.2(a)); second, the variable time spent in between frames (to write the data) leads to images captured at arbitrary phases of the cardiac cycle (Fig. 4.1(a)).

There are various ways to avoid scanning artifacts when imaging a fast-moving sample but none of them offers simultaneously the molecular insights possible with fluorescence microscopy, high enough spatial and temporal resolution, compatibility with a wide range of sample mounting protocols, and availability in most core imaging facilities. For example, the scan speed could be increased, such as demonstrated in optical coherence tomography (OCT)[46], where heart morphology and function in non-transparent embryos (both in avians [17, 47] and mammals [15]) is possible. However, in OCT, the scan speed is primarily limited by the instrument (mirror scan speed and light source intensity) whereas in fluorescence imaging, it is the number of available fluorophores that can emit light, which is the limiting factor, and hence faster scanning severely affects the SNR. For example, fluorescence LSMs equipped with a resonant scanner [48] can offer sufficient temporal and spatial resolution to image fast cells [49] but the faster scanning speed requires that the samples be very bright and that emitted photon losses be minimized as the pixel dwell time (the time spent by the scanner on a single point) is lower. High-performance point scanning confocal microscopy systems that combine high-speed scanners and light-efficient collection approaches [50] are sometimes available to researchers but they remain costly. Line scanning confocal microscopes [51, 13] and spinning disk microscopes [52, 53] allow imaging at high speeds yet at the cost of less regional scanning flexibility and crosstalk in thicker samples compared to point scanning systems. Light sheet microscopy [28, 23, 29, 30] satisfies the spatial and temporal resolution requirements for cardiac imaging but is not always available, in particular at imaging centers that have only few instruments; since the cost of purchasing a reliable turn-key microscope is high (ranging from tens to hundreds of thousands of USD or Euros), LSMs are a common first choice as they cover the needs and applications of many users (Table 4.1). Indeed, LSMs offer exquisite sensitivity and spatial resolution, optical sectioning capabilities in a wide range of fluorescent samples, possibility to scan only small regions of interest (ROI), compatibility with a variety of mounting techniques, and widespread options for both single and multi-photon excitation.

#### 4.1. Reconstruction of image sequences from ungated and scanning-aberrated laser scanning microscopy images of the beating heart

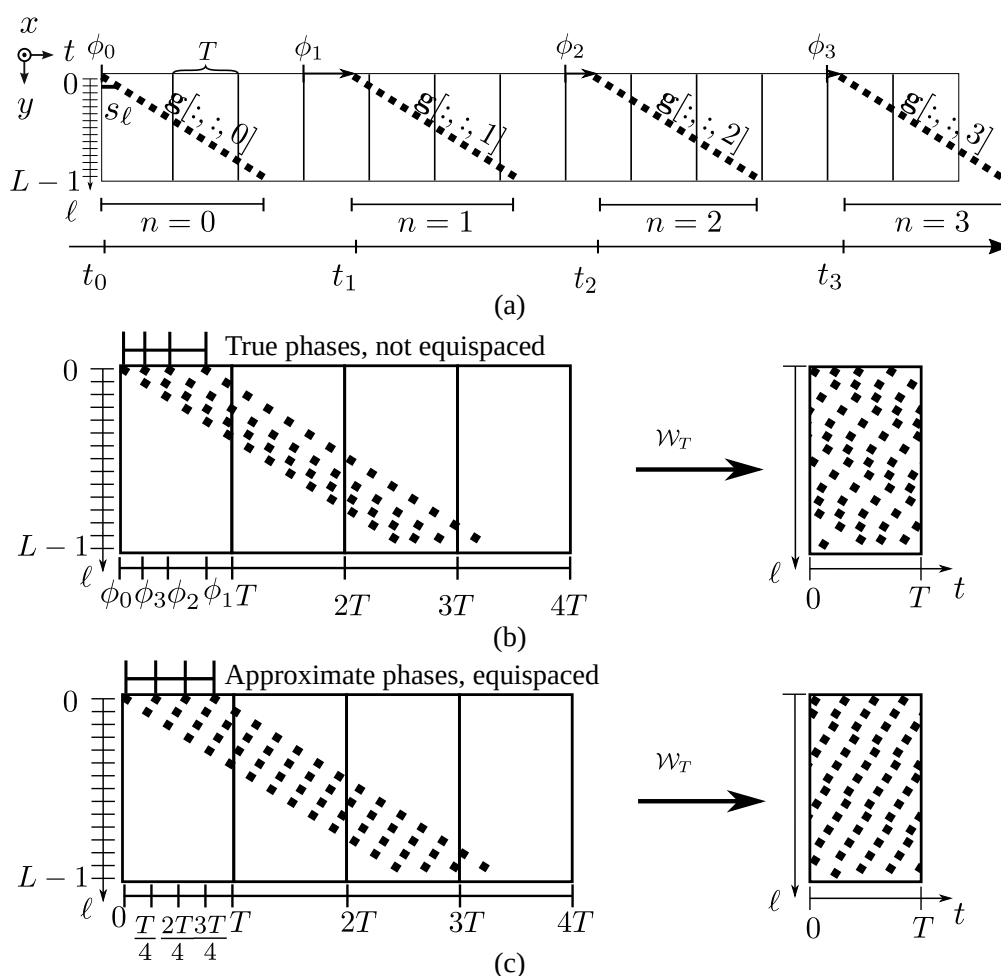


Figure 4.1 – Sampling model for scanning, true and approximated frame phase distribution. (a) The scanning acquisition results in sheared images  $\mathbf{g}[k, \ell, n]$ , (diagonal dots, one image line corresponds to one dot), which can span multiple periods  $T$  of the original signal. Acquisition is triggered at arbitrary times  $t_n$  with corresponding phases  $\phi_n$ . (b) Frames sorted according to their true (but unknown) cardiac phase. Wrapping the data to a single period results in a dense sampling of the space-time for one heart-beat. Note that given the stochastic nature of the start times  $t_n$ , the phases are not evenly distributed over the heartbeat. (c) While our sorting procedure produces reliable sorting, it does not provide the phase positions, which we approximate as equispaced. We investigate the error introduced by this approximation in Fig. 4.4(a).

## Chapter 4. Scanning aberrations correction

While purchasing or building a new microscope dedicated specifically to a cardiac imaging project (e.g. a light-sheet microscope) offers the best quality images at high speed, it will only be a sensible investment for researchers who image the heart regularly and can dedicate major funds to purchasing and maintaining such a microscope, or who have the skills to assemble a more cost effective version on their own [40, 54]. If LSM images of the heart were not severely corrupted by scanning artifacts, the possibility of using already existing (LSM) resources at a core facility would therefore be a practical, versatile, and economical alternative.

Table 4.1 – Comparison of optical sectioning-capable microscopy methods (Conventional laser scanning microscopy (LSM), Fast LSM (Airyscan [55]), light-sheet microscopy, and LSM combined with our proposed reconstruction method). More stars (\*) indicate preferred method. Our proposed approach extends the use range of widely available LSMs to cardiac imaging.

	Accuracy of cardiac shape in images	Sample preparation and mounting	Flexible ROI Imaging	Multi-photon options	Cost	Availability
LSM	*	Standard	****	****	\$\$\$	****
Fast LSM	****	Standard	****	**	\$\$\$\$	**
Light Sheet	****	Non-standard	*	**	\$\$\$\$/\$\$ <sup>a</sup>	**
LSM + our method	** to **** <sup>b</sup>	Standard	****	****	\$\$\$	****

<sup>a</sup>Commercial light-sheet microscopes are very expensive, but do-it-yourself options [40, 54] can be more affordable if skills and time are available.

<sup>b</sup>Dependent on cardiac phase and cell velocity

In this Chapter, we consider the problem of enabling such an alternative. Specifically, we aim at developing a computational method that takes a set of scanning-aberrated LSM images of the beating heart as input (as obtained, e.g., by use of an unmodified, off-the-shelf commercial LSM) and returns an image sequence (movie) with a faithful representation of the beating heart geometry covering one heartbeat (Fig. 4.2). Although, challenges of imaging the heart on slow devices have been considered in the past, we are not aware of methods that directly address the problem at hand.

### 4.2 Related work

Cardiac phase sorting methods have been considered in the past. Zhang and Pless [4] sorted cardiopulmonary MRI images according to the cardiac and respiratory phases by projecting the images on a low-dimensional manifold [56], and used level sets to segment the images. Kellman *et al.* [57] rebinned MRI images according to cardiac phase, with the phase determined with ECG timing data. In free-breathing MRI, Feng *et al.* [58] extracted the motion signal from different coils to extract estimations of the cardiac and respiratory frequencies, and then sort the acquired data according to the cardiac and respiratory phases. In OCT, Liu *et al.* [47] pooled OCT images from multiple sequences of continuous and undistorted heartbeats to obtain higher framerate sequences by determining their relative phases. Similarly, Happel

*et al.* [33] increased the frame rate in OCT using the string-length method [32, 12]. Approaches based on the string-length method assume that data are collected in a strictly sequential fashion and with known timestamps, which we do not assume here. Tralie and Berger [3] created high temporal resolution movies of periodic subjects by estimating the period of the signal then the phases within a sliding window. We recently proposed a cardiac phase sorting method (based on a traveling salesman problem (TSP) formulation) to recover the cardiac phase of a series of still images of a beating heart [26]. A similar TSP approach, albeit using different distance metrics and boundary conditions, has been proposed by Hanslovsky *et al.* [59] to sort out-of-order electron microscopy image stacks. Despite the ability of the above cardiac imaging methods to increase the framerate given instantaneous snapshots, none of them tackles the problem of compensating for aberrations introduced by scanning. Methods that compensate for scanning aberrations have been developed separately in other contexts, including for de-interlacing in television [60]. In the field of microscopy, Surgon *et al.* [61] have proposed a method to reconstruct a single frame without aberrations given a series of un-gated images. Nevertheless, this method falls short of reconstructing entire sequences, which is necessary to study cardiac dynamics.

### 4.3 Contributions

In this Chapter we present a fully computational method to recover cardiac heartbeat series from scanning-aberrated snapshots, with only minimal knowledge of the imaging device characteristics and without the need for additional hardware or hardware modifications, making our method well-suited for post-processing images acquired on a wide range of LSMs, even from devices that do not allow low-level acquisition adjustments by the user (a common limitation of commercial LSMs). We formulate the image reconstruction problem as a combined sorting and space-time unshearing problem, whose free parameters are unknown (cardiac phase, timestamps, or cardiac heart-beat frequency).

We propose to solve this image reconstruction problem by splitting it into two variational problems to recover the unknown parameters, followed by data resampling. Specifically, we cast the problem of retrieving the images' unknown phases as a shortest path search problem with periodic boundary conditions to match the cyclical nature of the cardiac heartbeat and with a pixel-wise similarity criterion as a distance metric, an approach whose efficacy we already demonstrated for sorting unaberrated cardiac images [26]. Following sorting we formulate the second problem as a space-time shearing problem whose unknown spacing parameter we recognize to coincide with the unknown cardiac period. Again, we use a variational approach to determine the unknown parameter, based on a minimum image difference criterion between adjacent, resampled slices.

In addition to detailing the method, we characterize the algorithm on synthetic data, demonstrate its applicability on experimental microscopy data, and qualitatively compare the reconstruction to experimental data acquired with two high-speed modalities.

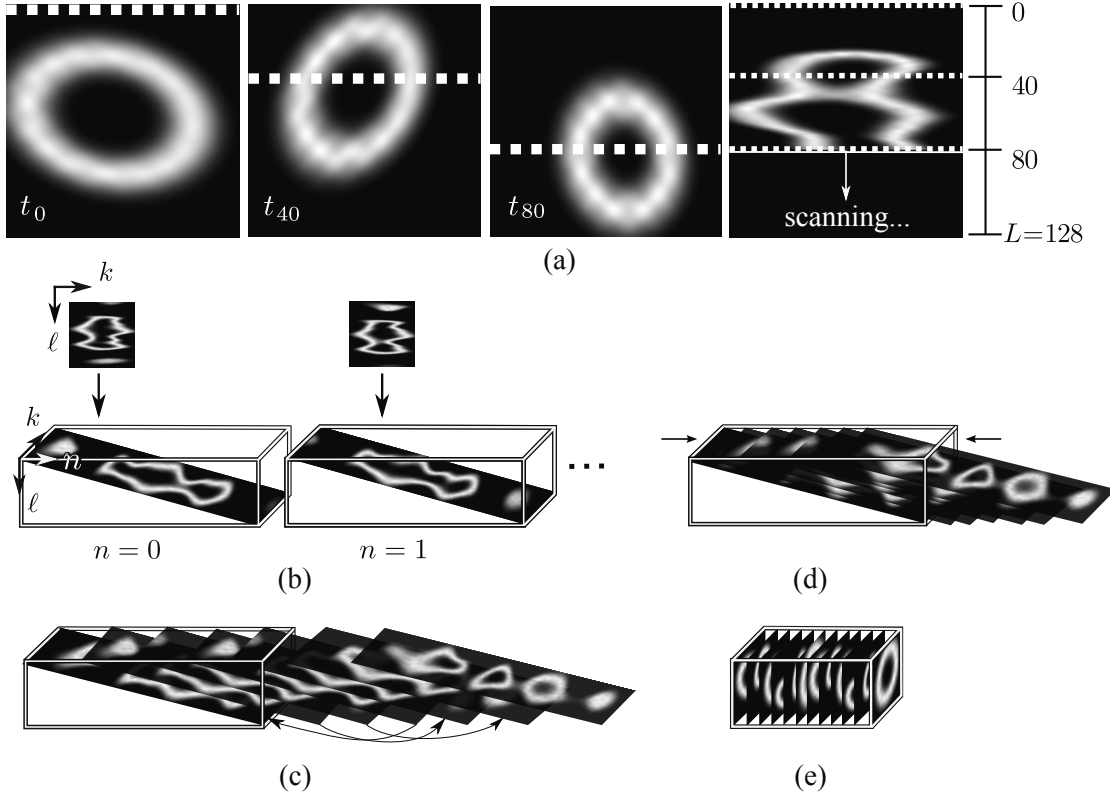


Figure 4.2 – Summary of acquisition and proposed reconstruction procedure. (a) Artifacts arise when a fast-moving object is imaged via slow scanning (one line at a time). Each row in the resulting frame (right) comes from a different cardiac contraction phase. (b)–(e) Our reconstruction procedure consists of: (b) collect multiple aberrated frames, which can be represented as slanted planes in space-time; (c) sort the frames according to increasing cardiac phase; (d) estimate the heartbeat period and produce a dense cardiac cycle; (e) resample the data on a uniform space-time grid that covers one heartbeat. See also Chapter 4 Supplementary Movie 1 for Steps (a) and (b).

Given the novelty of the reconstruction problem and method, we have characterized and validated our proposed approach using different datasets and settings. First, we reconstructed synthetically generated data (with and without noise corruption) for which the ground-truth signal was known, then quantitated the reconstruction accuracy as a function of the main free parameters. Next we carried out reconstructions on experimentally acquired images of the beating heart in zebrafish larvae, acquired on a (slow) confocal LSM, and compared our reconstructed images to those obtained via direct fast imaging methods (fast confocal LSM and light-sheet microscopy), suggesting that our method can reliably reconstruct the geometry of the beating heart (with some limitations).

The Chapter is organized as follows. In Section 4.4, we provide a formal description of the imaging model and problem. In Section 4.5, we propose a sorting solution based on a TSP solver and a compensation for scanning artifacts. In Section 4.6, we evaluate our method on synthetic and experimental data. In Section 4.7, we discuss our findings. Finally, we conclude

in Section 4.8.

#### 4.4 Model and Problem Definition

We consider a time-varying two-dimensional image whose intensity at spatial location  $(x, y)$  and time  $t$  we denote by  $f(x, y, t)$ . The image intensity varies periodically with a period  $T$ , such that, for any  $t \in \mathbb{R}$ , we have:

$$f(x, y, t) = f(x, y, t + T). \quad (4.1)$$

We further define a uniformly-sampled image series  $\mathbf{f}$  that covers the duration  $T$  of one heartbeat:

$$\mathbf{f}[k, \ell, n] = f(k\Delta_x, \ell\Delta_y, n\Delta_t), \quad (4.2)$$

where  $\Delta_x$  and  $\Delta_y$  are the pixel width and height, respectively,  $k = 0, \dots, K-1$  and  $\ell = 0, \dots, L-1$  are the row and column indices, respectively,  $n = 0, \dots, N-1$  denotes the time frame index, and  $\Delta_t = \frac{T}{N}$  denotes the time interval between frames.

We denote by  $\mathbf{g}[k, \ell, n]$ ,  $k = 0, \dots, K-1$ ,  $\ell = 0, \dots, L-1$ , and  $n = 0, \dots, N-1$ , the discrete image series measured by the scanning microscope, which we model by:

$$\mathbf{g}[k, \ell, n] = f(k\Delta_x, \ell\Delta_y, t_n + s_\ell \ell), \quad (4.3)$$

where  $s_\ell$  is the vertical scanning rate (in units of time per row, where we assume that the lateral scanning, which is fast compared to the vertical scanning rate, is instantaneous) and the  $t_n$ 's are the times at which the corresponding frames  $\mathbf{g}[:, :, n]$  are triggered. These starting times occur at increasing, but arbitrarily-spaced times:

$$t_0 < \dots < t_n < \dots < t_{N-1}, \quad t_n \in \mathbb{R}. \quad (4.4)$$

Given the above definitions, the image reconstruction problem is to obtain an estimate  $\tilde{\mathbf{f}}$  of the uniformly sampled image sequence  $\mathbf{f}$  given the sheared measurements  $\mathbf{g}$  and knowledge of the microscope's vertical scan speed  $s_\ell$  (but without knowledge of the underlying heartbeat period  $T$  nor the starting times  $t_n$ ).

#### 4.5 Phase sorting, period completion and estimation method

To reconstruct a uniformly sampled image series of the beating heart over one period from the scanning-aberrated data that we measure, we proceed in three steps, which can be summarized as follows: first, we sort the scanning-aberrated frames  $\mathbf{g}$  (Fig. 1(a) and (b)) so that the starting times  $t_n$  are in order of increasing cardiac phase (see Section 4.5.1, Fig 1(c)); next, we estimate the duration  $T$  of one heartbeat (see Section 4.5.2, Fig 1(d)) such that the pixels in

the sorted frames can then be assigned to their position in the cardiac phase space; finally, we resample the phase-ordered scanning-aberrated data on a uniform grid to obtain the final estimate  $\tilde{\mathbf{f}}$  (see Section 4.5.3, Fig 1(e)). Note that, in [26], only the special case where the vertical scanning rate is instantaneous was considered, i.e.  $s_\ell = 0$ , and the problem therefore limited to sorting frames.

### 4.5.1 Sorting scanning-aberrated images according to cardiac phase

We follow the phase-sorting method described in [26], and define the cardiac phases  $\phi_n$  of the  $n^{\text{th}}$  frame  $\mathbf{g}[:, :, n]$ , as the wrapping operation  $\phi_n = \mathcal{W}_T(t_n) = t_n + mT$ ,  $m \in \mathbb{Z}$ , s.t.  $\phi_n \in [0, T)$ . The task of sorting the frames is equivalent to finding a permutation  $\sigma : \{0, \dots, N-1\} \rightarrow \{0, \dots, N-1\}$ ,  $m \mapsto n = \sigma(m)$  such that the phases  $\phi_{\sigma(0)}, \dots, \phi_{\sigma(N-1)}$  are in increasing order:

$$\phi_{\sigma(0)} \leq \dots \leq \phi_{\sigma(N-1)}. \quad (4.5)$$

Given a sequence of images  $\mathbf{g}$ , we denote by  $\mathbf{g}^\sigma$  the phase-ordered (but still scan-sheared) frame sequence obtained by applying the permutation  $\sigma$  to  $\mathbf{g}$ :

$$\mathbf{g}^\sigma[:, :, m] = \mathbf{g}[:, :, n] \Big|_{n=\sigma(m)}, \quad m = 0, \dots, N-1. \quad (4.6)$$

We assume the cardiac cycle to be a closed repeating cycle and the images corresponding to adjacent phases in the cycle to be similar. We further assume that each cardiac phase produces a unique image (symmetrical patterns are excluded). We formulate the phase-ordering as a minimization problem, with image difference as a similarity criterion, so that this problem boils down to a classical combinatorial optimization problem. To do so, we define the cost of a given candidate permutation  $\sigma'$  (with  $\sigma'(t_0) = 0$ ) as:

$$\begin{aligned} C(\mathbf{g}, \sigma') = & \sum_{m=0}^{N-2} d\left(\mathbf{g}^{\sigma'}[:, :, m], \mathbf{g}^{\sigma'}[:, :, m+1]\right) \\ & + d\left(\mathbf{g}^{\sigma'}[:, :, N-1], \mathbf{g}[:, :, 0]\right), \end{aligned} \quad (4.7)$$

where the frame-wise distance operator  $d(\cdot, \cdot)$  between two 2D frames  $\mathbf{a}$  and  $\mathbf{b}$  is defined as:

$$d(\mathbf{a}, \mathbf{b}) = \sum_{k=0}^{K-1} \sum_{\ell=0}^{L-1} |\mathbf{a}[k, \ell] - \mathbf{b}[k, \ell]|. \quad (4.8)$$

Given that the distance is symmetrical, permutations that lead to a minimal cost come in pairs:

$$\{\tilde{\sigma}^T, \tilde{\sigma}\} = \arg \min_{\sigma' \in S_{N-1}} C(\mathbf{g}, \sigma'), \quad (4.9)$$

where  $\tilde{\sigma}$  is the ordering that satisfies Eq. (4.5), and  $\tilde{\sigma}^T$  the same permutation in reverse order.

Given an  $N \times N$  (symmetrical) table  $\mathbf{D}$  whose entries  $D_{j,k} = d(\mathbf{g}[:, :, j], \mathbf{g}[:, :, k])$  contain the



frame-wise distances between all frame pairs, we can recognize that Problem (4.9) is an incarnation of the TSP: the permutations we seek correspond to finding a path that visits each image (and comes back to the starting image) while minimizing the distance traveled between adjacent images.

In order to solve this problem efficiently and robustly, we spatially-average and downsample each frame  $\mathbf{g}[:, :, n]$ ,  $n = 0, \dots, N - 1$  before computing the distance table  $\mathbf{D}$ . Since there are  $(N - 1)!$  possible frame permutations ( $N$  is the number of frames and the first frame is fixed) exploring all combinations would be prohibitively expensive. Instead, we use the TSP solver package Concorde [34] with the linear programming solver QSOpt [35]. The computational time and complexity of the Concorde solver was discussed in [36], and shown to follow a function of the form  $a \cdot b^{\sqrt{N}}$ , with  $a = 0.21$  and  $b = 1.24194$  [37], which is still exponential, but grows much slower than  $(N - 1)!$ . We solve the problem of choosing between  $\tilde{\sigma}$  and the reverse permutation  $\tilde{\sigma}^\top$  in the next step.

##### 4.5.2 Estimation of the heartbeat period

Although the previous step produces a sorted series of images, the scanning artifacts remain. In order to compensate for them, we estimate the heartbeat period, which specifies the spacing of frames in space-time. Concretely, the phase-ordered images,  $\mathbf{g}^\sigma$ , are related to the underlying continuous signal  $f$  via:

$$\mathbf{g}^{\tilde{\sigma}}[k, \ell, m] = f(k\Delta x, \ell\Delta y, t_{\tilde{\sigma}(m)} + s_\ell \ell) \quad (4.10)$$

$$= f(k\Delta x, \ell\Delta y, \mathcal{W}_T(t_{\tilde{\sigma}(m)} + s_\ell \ell)) \quad (4.11)$$

$$= f(k\Delta x, \ell\Delta y, \mathcal{W}_T(\mathcal{W}_T(t_{\tilde{\sigma}(m)}) + s_\ell \ell)), \quad (4.12)$$

where Equation (4.11) results from the periodicity of  $f$  and Equation (4.12) from a property of the wrapping operation. In Equation (4.12), we recognize the phase  $\tilde{\phi}_m = \mathcal{W}_T(t_{\tilde{\sigma}(m)})$  of the  $m$ th frame of the ordered stack, which we substitute therein to obtain:

$$\mathbf{g}^{\tilde{\sigma}}[k, \ell, m] = f(k\Delta x, \ell\Delta y, \mathcal{W}_T(\tilde{\phi}_m + s_\ell \ell)). \quad (4.13)$$

We next approximate the (unknown) phase as:

$$\tilde{\phi}_m \approx \frac{Tm}{N}. \quad (4.14)$$

This approximation, illustrated in Fig. 4.1, leads to the following expression:

$$\mathbf{g}^{\tilde{\sigma}}[k, \ell, m] \approx f\left(k\Delta x, \ell\Delta y, \mathcal{W}_T\left(\frac{Tm}{N} + s_\ell \ell\right)\right). \quad (4.15)$$

The rationale behind the approximation in Eq. (4.14) is that we assume the starting phases to follow a uniform random distribution within one heartbeat, i.e.  $\phi_m \sim U([0, T))$ , which

stems from the stochastic nature of data write times to disk and (slight) variability in the heartbeat. Provided sufficient frames are available, such an assumption is reasonable. We have evaluated the accuracy of approximating the true phases by equispaced phases in Section 4.6.1 (specifically, see Fig. 4.3).

The final step before we can exploit Eq. (4.15) to reconstruct images of the beating heart is to estimate the heartbeat period  $T$ , which is unknown. To do so, we assume a candidate period  $T'$  for  $T$  and invert Eq. (4.13) to obtain  $\mathbf{f}_{T'}$ , a uniformly sampled (without scanning aberration) version of  $f$ :

$$\mathbf{f}_{T'}[k, \ell, n] = \mathbf{g}^{\tilde{\sigma}} \left[ k, \ell, \mathcal{W}_N \left( n - \left( \frac{s_\ell N}{T'} \ell \right) \right) \right]. \quad (4.16)$$

Since the time index in the right-hand-side can be non-integer, we interpolate the data between successive time points. Specifically, we use a cubic B-spline model with periodic boundary conditions [62].

Next, to obtain the estimate  $\tilde{T}$  of the underlying period  $T$ , we minimize the sum of the differences between neighboring rows  $\ell$  for reconstructions  $\mathbf{f}_{T'}$  obtained from different values of the candidate period  $T'$ :

$$\tilde{T} = \underset{T'}{\operatorname{argmin}} \left( \sum_{k=0}^{K-1} \sum_{\ell=0}^{L-2} \sum_{n=0}^{N-1} \left| \mathbf{f}_{T'}[k, \ell, n] - \mathbf{f}_{T'}[k, \ell+1, n] \right| \right). \quad (4.17)$$

If the period resulting in the minimal cost is smaller than 0, then the best estimated permutation is  $\tilde{\sigma}^T$ , and the time points need simply to be mirrored with respect to time.

In practice, we used an implementation (from the Python package SciPy) of the Nelder-Mead simplex method [63] to minimize the expression in Eq. (4.17).

### 4.5.3 Scan-aberration compensation via resampling

Finally, Equation (4.16), evaluated for the optimal estimate  $T' = \tilde{T}$ , provides our estimate of  $\mathbf{f}$  in Eq. (4.2):

$$\tilde{\mathbf{f}} = \mathbf{f}_{\tilde{T}}. \quad (4.18)$$

## 4.6 Experiments

We have characterized the accuracy of our method and evaluated its applicability in practice, which we detail in the following sub-sections.

#### 4.6.1 Expected error due to non-gated, non-uniform sampling

We first investigated the error that can be expected from the approximation in Eq. (4.14). Under the assumption that the starting times of the image acquisitions are stochastic and unrelated to the heartbeat (a reasonable assumption given that slight irregularities in the heart-beat are common and that we empirically observed the image write-times to the disk to be stochastic), we compared the error we make by calculating the differences between the actual phases and the regularly-spaced phases that we impose on the ordered sequences during reconstruction. The assumption here is that there is no error in the ordering of the frames (an aspect that we study separately in Section 4.6.2). For a given number of frames, we computed the differences between the left-hand side and the right-hand side of Eq. (4.14), which corresponds to the integral of the absolute difference between realizations of the true phase curves and the linear approximation (see Fig. 4.3 inset A, B, C). We repeated the experiment, drawing phases from a uniform distribution, i.e.  $\phi_n \sim U([0, N))$ , and for a varying number of frames,  $N \in \{10, 20, 30, \dots, 300\}$ . We observed that the error decreases as the number of frames increases (Fig. 4.3).

#### 4.6.2 Method characterization on synthetic data

We next characterized the performance of the full reconstruction pipeline with respect to scan speed and number of frames on synthetic data.

##### Simulation framework for synthetic heart and scanning microscope

We simulated a beating heart (as previously described in [12]) and the LSM acquisition process by re-sampling data generated on a uniform grid. To simulate a beating heart  $f(x, y, t)$ , we produced synthetic time-series data  $\mathbf{f}^*[k, \ell, n]$ , where  $k = 0, \dots, 255$ ,  $L = 0, \dots, 255$ , and  $n = 0, \dots, 2999$ . The images featured a periodically contracting ring, with period  $T = 6\pi$ , which avoided sampling the exact same images over several periods when simulating the scanning artifacts. This sampling protocol represents a non-gated acquisition process, where each image is acquired at a different phase.

To simulate the line scanning acquisition process, we defined the heartbeat-to-frame scanning rate ratio  $r = \frac{s_\ell L}{T}$  (with units of number of beats per frame (bpf)). With these units, the simulated data can be expressed, based on Eq. (4.3), as  $\mathbf{g}[k, \ell, n] = \mathbf{f}^*[k, \ell, t + \frac{\ell r T}{L} + nrT]$ , where  $t \in U[0, T)$  is a random starting point in the period. At constant acquisition rate,  $r$  increases when the heartbeat increases, while at a constant heart rate, an increase in  $r$  corresponds to a decrease in the scanning speed. This simulation allowed us to investigate the influence of two imaging parameters: the number of frames  $N$  and the heartbeat-to-frame scanning rate ratio  $r$ . We first fixed the heartbeat-to-frame scanning rate ratio  $r$  and varied  $N$ . Then, we fixed the final number of frames  $N$  and varied  $r$ . See Chapter 4 Supplementary Movie 2 as an illustration.

### Noise simulation

To make our simulation more realistic, we considered each pixel  $i$  to be a realization of a Poisson process whose parameter we set to the noise-free pixel value  $f_i$  (in the range 0 to 1) times a global  $\lambda$  level (proportional to the product of photon emission rate and detector dwell time), such that the probability of measuring  $k$  photons on a particular pixel was  $p_i(k) = e^{-\lambda f_i} \frac{(\lambda f_i)^k}{k!}$ . We simulated data with three global parameters,  $\lambda = 1$ ,  $\lambda = 10$ , and  $\lambda = 100$ , which on a pixel with noise-less intensity  $f_i = 1$ , leads to measuring (on average) 1, 10, and 100 photons, respectively.

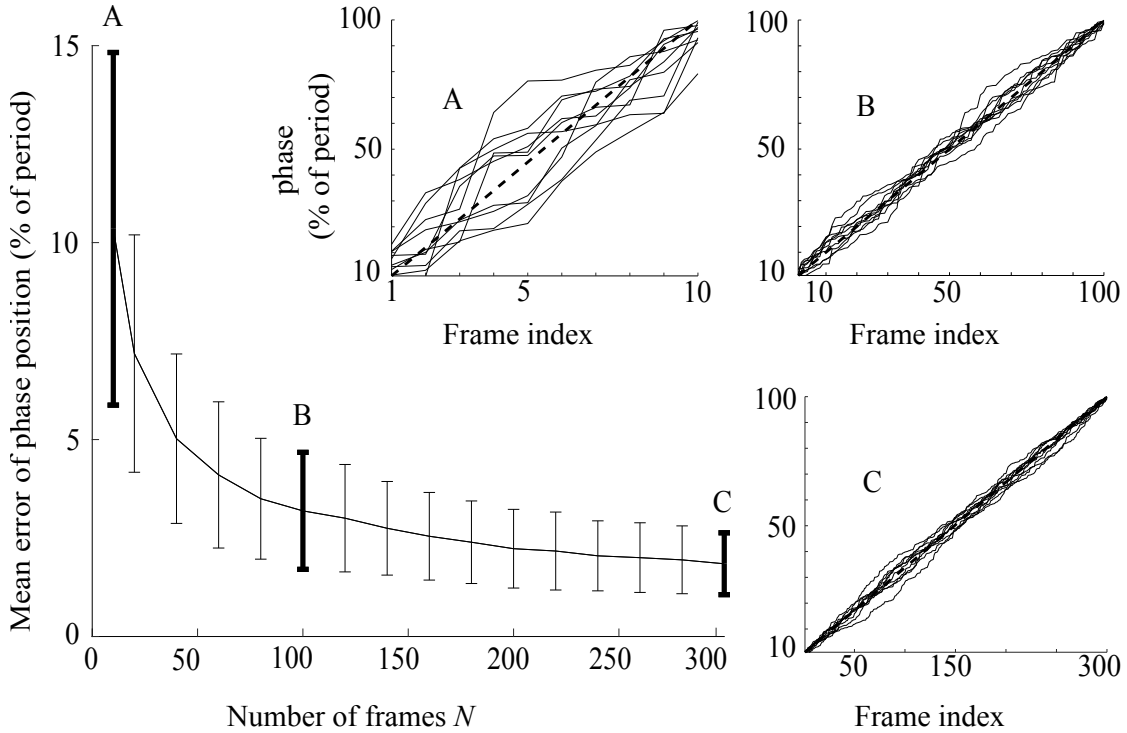


Figure 4.3 – Accuracy of the equispaced phases approximation. Mean distance between true and equispaced (approximated) phases assuming phases follow a uniform random distribution over the interval of a cardiac period and that sorting is perfect. Insets A, B, and C show the true phase as a function of the frame and the deviation from the equispaced phase assignment (diagonal) when the number of frames is 10, 100, and 300, respectively (10 realizations shown in each case).

### Evaluation of sorting accuracy

To characterize the accuracy of the frame-sorting method that uses the TSP solver with the image-based distance, we carried out the following experiments. We averaged and downsampled the simulated data by a factor 4, then sorted the downsampled data according to the solution of the TSP solver. We next inspected if the known ground truth phases attached to each frame

were in proper sequence. Specifically, to quantify the sorting accuracy we defined the score:

$$\mathcal{E}[n] = \begin{cases} 1 & \phi_{\tilde{\sigma}(n)} < \phi_{\tilde{\sigma}(\langle n+1 \rangle_N)} \\ 1 & \phi_{\tilde{\sigma}(n)} = \phi_{\max} \text{ and } \phi_{\tilde{\sigma}(\langle n+1 \rangle_N)} = \phi_{\min} \\ -1 & \text{otherwise,} \end{cases} \quad (4.19)$$

where  $\phi_{\min}$  and  $\phi_{\max}$  are the minimal and maximal ground truth phases, respectively and  $\langle n \rangle_N = n \bmod N$ . When correctly sorted, the phases should be in a strictly increasing or decreasing order, with a single jump between the minimal and maximal phases  $\phi_{\min}$  and  $\phi_{\max}$  and we defined the overall sequence sorting score as follows:

$$\bar{\mathcal{E}} = \left| \frac{1}{N} \sum_{n=0}^{N-1} \mathcal{E}[n] \right|, \quad (4.20)$$

with  $0 \leq \bar{\mathcal{E}} \leq 1$ , where a low score expresses poor sorting and a high score a correct sorting (the score does not penalize an inverted overall direction of the sorting). We additionally quantified this sorting score by measuring the error magnitude, i.e. the frame positional error as a percentage of the number of frames  $N$ .

First we studied the influence of the number of frames on the sorting accuracy by varying  $N \in \{10, 20, \dots, 300\}$ , keeping the heartbeat-to-frame scanning rate ratio fixed to  $r = 2\sqrt{2}$  bpf (Fig. 4.4). In the noiseless case, the average sorting score does not vary much as the number of frames increases. Although the sorting score decreases with higher noise levels ( $\lambda = 1$ ,  $\lambda = 10$ ) the relative phase error induced remains low (Fig. 4.4(b)).

Next, we set  $N = 100$  and varied the heartbeat-to-frame scanning rate ratio  $r \in \{0.5\sqrt{2} \text{ bpf}, \sqrt{2} \text{ bpf}, \dots, 9.5\sqrt{2} \text{ bpf}\}$  Fig. 4.4(a). The quality of the reconstruction decreases as the number of heartbeats per frame  $r$  increases. This indicates that while a slow scanning speed ( $r$  large) may be acceptable, the reliability of the sorting method is best when the scanning speed is fast ( $r$  is small).

### Characterization of the accuracy of the period determination method

In order to characterize the accuracy with which we can estimate the period of the heartbeat, we calculated the normalized difference between the estimated period  $\tilde{T}$  and the ground truth period  $T$ :

$$\mathcal{E}_{\tilde{T}} = \frac{|T - \tilde{T}|}{T}. \quad (4.21)$$

Similarly to Section 4.6.2, we considered first a fixed scan rate ratio  $r$  and varied  $N$ , then we fixed  $N$  and varied  $r$  (Figs 4.4(f) and 4.4(g), respectively). We observed that increasing the number of images  $N$  (Fig. 4.4(f)) increases the accuracy of the heartbeat period estimation with a lower variability as we repeated the experiment with multiple realizations of the starting phases. Decreasing the scanning speed (increasing  $r$ ) improves the accuracy of the heartbeat

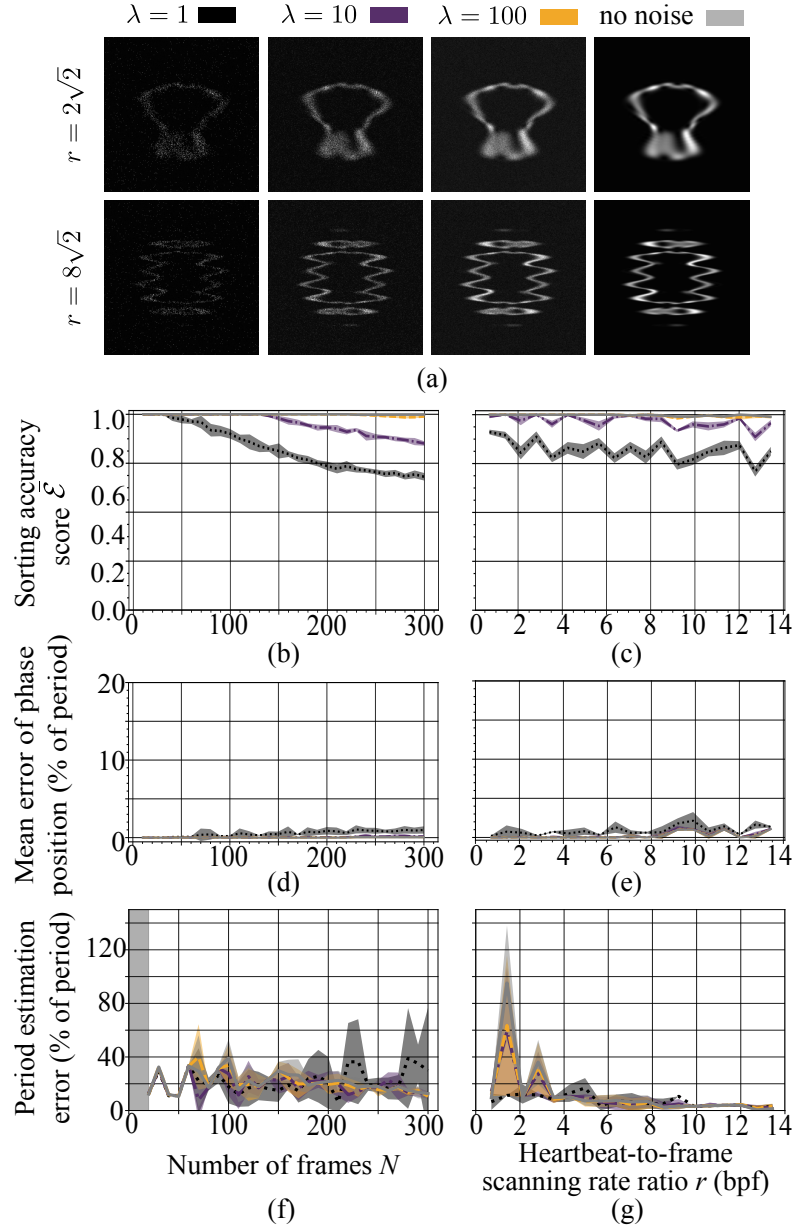


Figure 4.4 – Accuracy of the frame sorting and period estimation procedures. (a) Simulated data with decreasing levels of Poisson noise (Section 4.6.2), and without noise . The upper row shows data with a heartbeat-to-scanning rate ratio  $r$  of  $2\sqrt{2}$ , and the lower row of  $8\sqrt{2}$ . (b)–(c) Accuracy of the frame sorting procedure (see Eq. (4.20)) based on synthetic image data when (b)  $r = 2\sqrt{2}$  bpf is fixed while the number of frames  $N$  varies and (c)  $N = 100$  is fixed and  $r$  varies. The lines represent the mean over 10 realizations of the simulated movies, and the shadings the standard deviation. Darker colors indicate a higher level of noise, i.e. a lower value of  $\lambda$ . (d)–(e) Phase position error as a percentage of period when (d)  $r = 2\sqrt{2}$  bpf is fixed while  $N$  varies and (e)  $N = 100$  frames is fixed and  $r$  varies. (f)–(g) Positional error as a percentage of number of frames  $N$  (f)  $r = 2\sqrt{2}$  bpf is fixed while  $N$  varies and (g)  $N = 100$  frames is fixed and  $r$  varies. (f) The vertical shading for  $N \in [0, 19]$  indicate low reliability.

period estimation, with less variability as the experiment is repeated over multiple realization of the random starting phases of the frames. We observe that the estimation is robust to photon-count parameter as low as  $\lambda = 10$ , with the method becoming unreliable for  $\lambda = 1$ .

#### 4.6.3 Evaluation of the overall accuracy of the proposed reconstruction method

To quantify the end-to-end quality of our entire reconstruction procedure we calculated the intersection over union (IOU [64]) index between ground truth and reconstructed images. The IOU index gives a quantification of the image overlap, or in our case a quantification of the overall reconstruction quality. As the IOU requires binary images, we applied the reconstruction parameters (phase ordering and period estimation) to the noise-free data equivalent to our noisy datasets. We used the mean of the images as a threshold.

For medium to high photon counts ( $\lambda = 10, 100$ , no noise), increasing  $N$  improves the overall reconstruction quality (Figs. 4.5(a) and 4.5(c)). In high-noise conditions ( $\lambda = 1$ ) the reconstruction quality becomes variable as  $N$  increases, in agreement with the worsening sorting and phase estimation performance at these low light conditions (Fig. 4.5). As the scan rate ratio  $r$  is increased, the overall reconstruction quality decreases slightly (Figs. 4.5(b) and 4.5(d)). However, this result assumes that it is possible to keep the photon count constant as the scanning speed is increased. In practice, a slower scanning rate, leads to longer dwell times and proportionally larger photon counts (at constant excitation intensity). To illustrate the benefits of using slower scan rates (higher  $r$ ), we compared the reconstructions obtained by simultaneously slowing the scanning rate ( $r = \{2\sqrt{2}/25, 2\sqrt{2}, 8\sqrt{2}\}$ ) and proportionally increasing the photon counts ( $\lambda = \{1, 25, 100\}$ , Fig.4.5(c) and Chapter 4 Supplementary Movie 10). Reconstructions show that the shape of the synthetic heart is recovered in all cases, but that the main benefit of a longer dwell-time—the associated higher photon count—can be reaped by compensating the accompanying scanning artifacts with our proposed method.

#### Evaluation of the reconstruction time

We timed the reconstructions on a Debian GNU/Linux 9.9 Operating System, with an Intel Core i7-5930K 3.50GHz CPU, and 32GB RAM (see Fig. 4.6). Within the probed range of frames, we observed that the reconstruction time increases linearly with the number of frames and stays constant as the heartbeat-to-frame scanning rate ratio increases. As shown in a detailed example in Section 4.6.4, the resampling step is the most time consuming, and scales linearly with the data size. The sorting step scales exponentially with the data size as mentioned in Section 4.6.1 but contributes less to the overall computational cost.

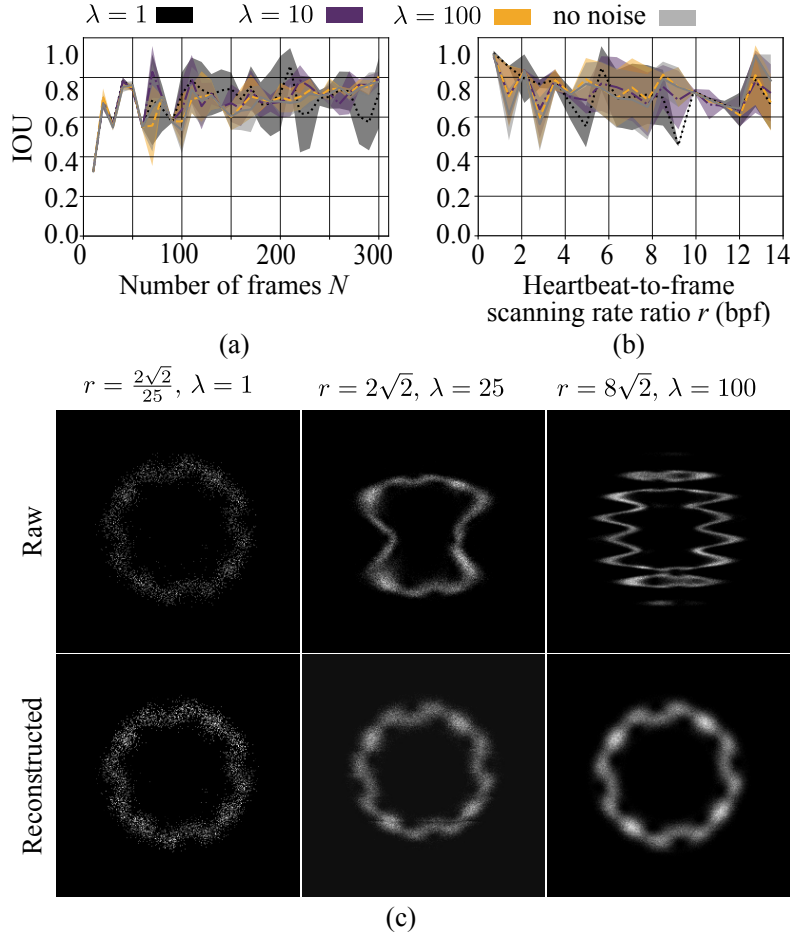


Figure 4.5 – The image reconstruction quality (IOU) on simulated data compared to ground truth (a)–(b). Reconstruction quality when: (a) the heartbeat-to-frame scanning rate ratio  $r = 2\sqrt{2}$  bpf is fixed while the number of frames  $N$  varies and (b) the number of frames  $N = 100$  is fixed and  $r$  varies. Each line corresponds to the mean of one level of noise, over 10 realizations, and the shadings the standard deviation. (c) High acquisition speed data,  $r = \frac{2\sqrt{2}}{25}$ ,  $\lambda = 1$  versus lower acquisition speeds,  $r = 2\sqrt{2}$ ,  $\lambda = 25$ , and  $r = 8\sqrt{2}$ ,  $\lambda = 100$ , from left to right. The upper row is the acquired data, the lower row is the reconstructions. See also Chapter 4 Supplementary Movie 11.



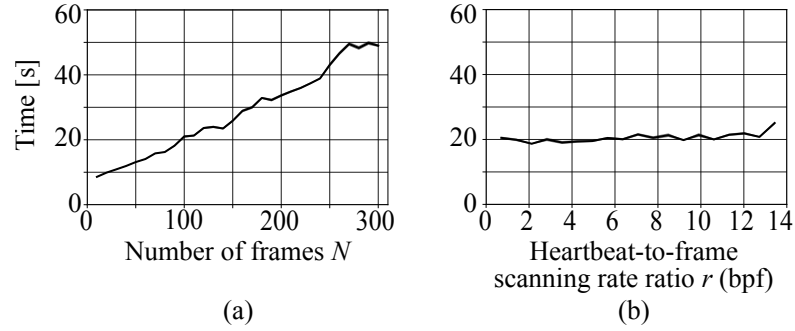


Figure 4.6 – The computation reconstruction time increases with (a) the number of frames  $N$ , rather than (b) the number of beats per frame  $r$ .

#### 4.6.4 Reconstruction of a beating heart sequence from experimental measurements

##### Methods

In order to evaluate the potential of our method for biological applications using standard LSMs, we acquired data in live samples. We bred transgenic zebrafish (Tg(myl7:GFP) [65] and Tg(myl7:membranemCherry) [38]), which express fluorescent proteins in the heart (green and red fluorescent protein, respectively, in the muscle cells of the entire heart) according to standard procedures [39]. All procedures were previously authorized by the Veterinary Office of the Canton of Bern, Switzerland, for conformity. We grew the zebrafish embryos in E3 medium and added PTU (0.003% 1-phenyl-2-thiourea) to avoid pigmentation when the embryos reached an age of 24 hours post fertilization (hpf). At an age of 36 hpf, we removed the chorion surrounding the embryos with forceps and anesthetized the embryos with Tricaine at 0.08 mg/ml, pH 7. We embedded the embryos with the ventral side down on a glass bottom dish in 1% low melting agarose (Promega). We imaged the heart on a Zeiss LSM880 inverted confocal microscope with an LD C-Apochromat  $40\times/1.1$  NA water immersion objective lens.

##### Qualitative evaluation on multiple samples

We imaged the hearts of Tg(myl7:GFP) (Fig. 4.8, Chapter 4 Supplementary Movie 3) in single direction scanning mode and the hearts of Tg(myl7:membrane-mCherry) in both single (Fig. 4.9, Chapter 4 Supplementary Movies 5–9) and bi-direction (Fig. 4.7, Chapter 4 Supplementary Movie 4) scanning modes. The reconstructions allow recovering the sequential beating of the heart, with atrium and ventricle beating distinctively one after the other (Fig. 4.7 and Chapter 4 Supplementary Movie 4).

In order to evaluate the practical potential of our method on a multi-channel data set, we further imaged the transgenic Tg(myl7:membranemCherry) zebrafish and simultaneously collected fluorescence emission and transmitted light. The duration to scan a full frame of  $1024\times 1024$  pixels was 1270 ms/frame, with a corresponding duration to scan a line of  $s_\ell = 1.24$

## Chapter 4. Scanning aberrations correction

ms. We acquired  $N = 100$  images. Based on those numbers and our method, we estimated the period to be  $\tilde{T} = 0.33$  seconds, which corresponds to  $\frac{1}{\tilde{T}} = 3.0$  heartbeats per second. The reconstructed sequence of 100 images, which covers one heartbeat, therefore has a virtual frame rate of 300 Hz. For this dataset, the whole reconstruction took 1 minute and 9 seconds: it took 3.4 seconds to load the data (in CZI format); calculating the distance table **D**, finding the TSP solution, and sorting the data took 3.1 seconds; estimating the period took 2.1 seconds; resampling took 41.3 seconds; finally, saving the data both to MP4 and OME formats took 21.7 seconds. This reconstruction was performed on a Debian GNU/Linux 9.9 Operating System, with an Intel(R) Core(TM) i7-5930K CPU 3.50GHz, and 32GB RAM.

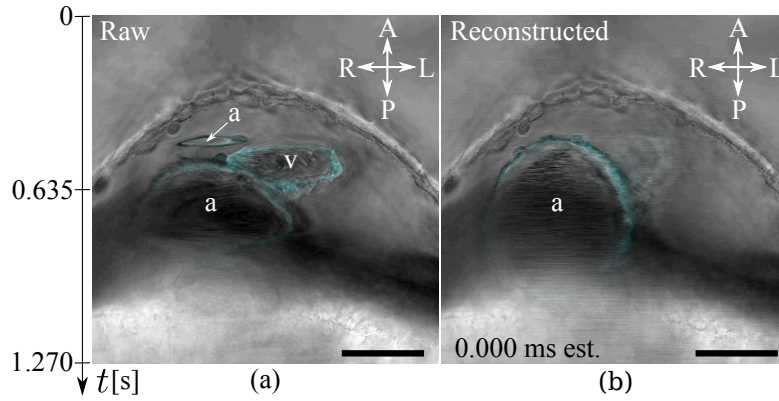


Figure 4.7 – This dataset features both chambers of the beating heart. The images were acquired in transmission (gray) and fluorescence (cyan) simultaneously. (a) Raw frame: several heartbeats are co-mingled. In particular the atrium (marked by ‘a’) a single chamber of the heart, appears as two separate chambers. Both the atrium and the ventricle (marked by ‘v’) show deformations due to the slow acquisition. (b) Reconstructed heart. The atrium is properly shaped. The contracted ventricle is out of the field of view in this frame (full sequence in Chapter 4 Supplementary Movie 4). A: anterior, P: posterior, L: left, R: right. Scale bar is  $50\mu\text{m}$ . Additional reconstructions can be seen in Chapter 4 Supplementary Movies 7–9

### 4.6.5 Reconstruction independence on scanning direction

To verify that the reconstructions were not biased by the mounting orientation with respect to the scanning direction, we acquired two movies of the Tg(myl7:GFP) zebrafish heart with the scan-field rotated by 0 and 90 degrees (see Figs. 4.8(a) and 4.8(b), respectively). We superimposed both reconstructed datasets (Fig. 4.8(c)), in the green channel for one scan-field orientation and in the purple channel for the 90-degree rotated orientation. Discrepancies in the reconstructions are visible whenever the signal is not white, which occurs predominantly in the fastest phases of the cardiac cycle as can be seen in Chapter 4 Supplementary Movie 3.

### 4.6.6 Comparison to state-of-the-art fast microscopes

In order to compare our method with the fastest (commercially) available microscopes, we carried out the following experiments. First, we took advantage of the fact that the LSM we used (Zeiss LSM880) was equipped with an Airyscan module, which permits scanning at high speed and allowed us to do a direct comparison (on the same sample) with standard LSM (Fig. 4.9(d)-(f)).

In addition, we acquired images with a Leica TCS SP8 microscope in both LSM and light sheet mode. To do so, we prepared a U-shaped capillary on plasticine in a glass bottom MatTek dish. Subsequently, we immersed a zebrafish larva at 3 dpf in 1% low melting agarose and mounted it into the capillary, ventral side up. We acquired the images in the light sheet mode. We removed the larva from the capillary and mounted it ventral side down in 1% low melting agarose in a glass bottom dish. We then acquired the confocal LSM images of the same larva in a similar position (Fig. 4.9(a)-(c)).

Fig. 4.9 and Chapter 4 Supplementary Movies 5 and 6 show that the reconstructions with our method from data from a slow LSM yield comparable quality reconstruction during the slow phases of the heartbeat, with artifacts remaining when the motion of the heart is at its fastest.

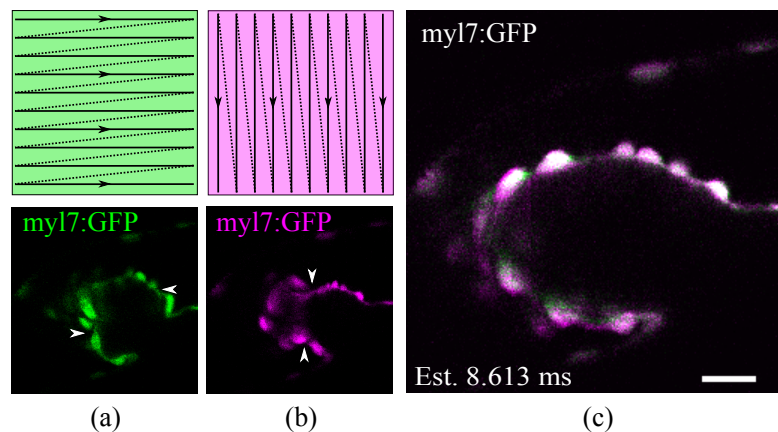


Figure 4.8 – Reconstruction is independent of scan field orientation. (a) Top: single-direction, row-first scanning. Bottom: Raw scan frame acquired prior to reconstruction has artifacts: arrows indicate pinching of the membrane that is due to presence of multiple phases of the heartbeat in one frame (scanning artifact). (b) Top: scan-field is rotated by 90 degrees. Bottom: Similar scanning artifacts are visible (arrows). (c) Composite frame of the reconstructed movies obtained from the original and rotated scan-field data, in the green and purple channels, respectively. Predominantly white areas show consistent reconstruction and independence from scan direction. See also Chapter 4 Supplementary Movie 3. Scale bar is  $20\mu\text{m}$ .

### 4.7 Discussion

Our method addresses the problem of reconstructing scanning-aberrated images with minimal knowledge of the experimental process, to ensure applicability with a wide range of microscopes (closed commercial or custom-built). Specifically, our method does not require gating the microscope to the heartbeat. Although demonstrated as feasible on custom microscopes, gating requires an additional layer of experimental complexity [1] and is difficult to implement on commercial microscopes, which forbid low-level user intervention during the acquisition process. We also note that although the arbitrariness in the timestamps is not purposeful, as it naturally arises from slow variations in the heartbeat on the sample side or communication lags on the acquisition side, the lack of perfect periodicity is also an advantage as it limits the risk of stratified sampling, which could provide only partial coverage of the cardiac phases.

The first step of our method sorts the frames, which then cover one single period with a higher (virtual) time sampling density. The underlying assumption is that the phase is drawn from a uniform distribution. We further assume that the sorted phases are equally spaced. In [26], we observed that the discrete signal  $\mathbf{f}[k, \ell, n]$  (Eq. (4.2)) had to be asymmetric for the sorting to be successful. Here, since the scanning aberrations encode the movement direction in the images, all images are by construction asymmetric. Our investigation of the uniform distribution with equally-spaced and deterministic samples approximation (Fig. 4.3), showed that it is less error-inducing as the number of frames  $N$  increases. We determined that this error becomes acceptable when  $N > 100$ , as the maximal difference error becomes less than 5%, meaning that there is less than 5% difference between the non-uniform time position after sorting and the uniform time position. If the number of frames is lower,  $N < 100$ , then the time difference between two successive sorted frames will have more than 5% maximal error and lead to important reconstruction artifacts, or even make reconstruction impossible (which we further discuss below). Our choice of using a TSP solver allowed us to find reliable solutions in a very short time (around a second for 100 frames). The sorting error depends on noise, (Fig. 4.4(b), Fig. 4.4(c)), but although the number of sorting errors increases, the phase errors remains low (Fig. 4.4(d), Fig. 4.4(e)).

The second step estimates the signal period. We observed that acquiring more images leads to a better period estimation and lower variance as we repeat the experiments over multiple realization of the simulated data (Fig. 4.4(f)). However, very noisy data lead to an increase in period estimation error as  $N$  increases, especially over approx.  $N = 150$  frames. The sorting accuracy for data with  $\lambda = 1$  is below 75% when  $N > 150$ . Even if the phase position errors are small (less than 2%), the accumulation of errors leads to an increasing error in period estimation; for  $\lambda = 10$  the estimated period error is 30% at most, and for  $\lambda = 100$  is around 10%. For fewer than  $N = 100$  frames, the standard deviation of the error increases and reconstructions are less reliable for all levels of noise. As  $r$  increases, the mean and standard deviation drop very quickly (Fig. 4.4(f)). The error on the estimated period decreases from around 20-40%, when  $r = 1.8$ , to below 5% for all noise levels, when  $r > 9$ . There is a trade-off

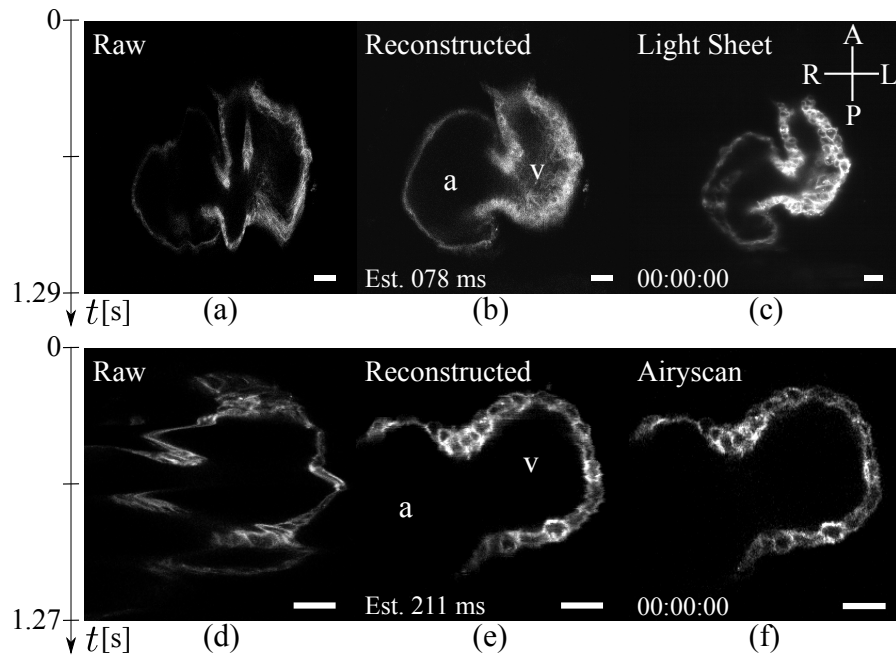


Figure 4.9 – These datasets feature both chambers of the beating heart. In (a) and (d) several heartbeats are co-mingled. Both the atrium (marked by ‘a’) and the ventricle (marked by ‘v’) show deformations due to the slow confocal microscope acquisition. (b) and (e) show reconstructed hearts. The atrium and ventricle are properly shaped. (full sequences in Chapter 4 Supplementary Movies 5 and 6). (c) Data acquired with a light sheet microscope. There are no deformations in this image, as an entire plane is acquired at once. (f) Data acquired with a confocal equipped with an Airyscan, which allows much faster acquisitions, avoiding deformations. A: anterior, P: posterior, L: left, R: right. Scale bar is  $20\mu\text{m}$ .

to find between the number of frames and the heartbeat-to-framerate ratio. A higher number of heartbeats per frames with a low noise level lead to a better reconstruction than a noisy data acquired with less heartbeats per frame. A high level of noise with a very fast scanner would not need to be reconstructed (4.5(c) upper left), but the data will have a very low SNR. That could easily be improved with a slower scanning speed (i.e. higher heartbeat-to-frame ratio  $r$ ), that would allow for a higher SNR with a high reconstruction accuracy.

The overall accuracy (Fig. 4.5) is better when the number of frames  $N$  is high, and the scan rate ratio  $r$  is high. The overall accuracy as a function of the scan rate ratio  $r$  (Fig. 4.5(b)) seems to be mainly limited by the sorting step (Fig. 4.4(c) and (e)), since the estimated period error decreases with higher scan rate ratios (Fig. 4.4(g)). The overall accuracy is better with a lower noise, and that translates to a slower scanning rate. Data can be acquired with a high scanning speed (Fig. 4.5(c), upper-left image), without any visible scanning aberration in the data. In that case, the data do not need to be reconstructed to compensate for scanning artifacts, but they are very noisy. When slowing the scanning speed, the data become scanning-aberrated but also less noisy (Fig. 4.5(c) upper-middle and -right). The reconstruction quality increases with longer integration times (Fig. 4.4(b)–(g), Chapter 4 Supplementary Movie 10).

Coarse image structures appear sufficient to provide the necessary information to sort and estimate the heartbeat period and we can therefore average and downsize raw images for processing, which both reduces image noise (improving the reconstruction accuracy) and computation time. In practice we used a downsizing factor of 4 for a minimal image size of  $64 \times 64$  pixels, which is sufficient for a good reconstruction, but for raw images whose size is less than  $256 \times 256$ , reconstruction becomes less reliable.

Our method assumes that the cardiac motion is both spatially and temporally cyclic and deviations from this assumption lead to reconstruction artifacts. While our method could be used in perturbation experiments that maintain a regular heartbeat (e.g. perturbations that slow or accelerate the heart-beat yet maintaining it stationary [66, 67]) it would not be applicable to study the effect of more general perturbations or diseased hearts that exhibit severe arrhythmia.

## 4.8 Conclusion

In this Chapter we proposed a method to reconstruct image series of the beating heart from scanning-aberrated microscopy images. The method relies on a fast TSP solver to sort images according to a minimal frame-to-frame image difference and we use a spatial difference criterion to compensate for scanning aberrations.

We characterized the method on synthetic data, and showed that data acquired at a frame rate up to 4 heartbeats per period (equivalent to a duration to scan a full image of about a second per frame in the case of the beating heart of a zebrafish larva) for 100 frames allows over 75% reconstruction accuracy (IOU, noise up to  $\lambda = 10$ ). This accuracy can be improved

by increasing the number of collected frames (at the cost of a longer overall image acquisition time). We showed that our method allows reconstructing data with a virtual framerate of up to 300 Hz. We demonstrated that the method is applicable in practice on data from a standard confocal LSM, providing reconstruction quality similar to that of state-of-the-art fast microscopes in the slower phases of the heartbeat (with remaining artifacts in the faster phases). We foresee that this reconstruction method could be applied to other point- or line-scanning microscopy modalities (in particular, for multi-photon imaging, where alternatives to point scanning are even fewer). Our simulations provide guidelines on the critical parameters (number of frames and scanning speed) to be adjusted and an experimental procedure to verify the validity of a reconstruction, by varying the sample orientation with respect to the scanning direction. Future work could include extensions for sub-pixel estimation of frame positions and automatic detection of arrhythmia, where our method would not be applicable.

### 4.A Scanning-aberrations correction in volumetric data

As a proof of principle, I applied the method described in Chapter 4 on synthetic volumetric time-series. In Chapter 4 I showed we could use our method to correct for scanning aberrations in images. However, similar scanning aberrations can be seen in volumes, if the microscope acquired several heartbeats per volume. In this case, the scanning aberrations can be seen in XZ/YZ.

I adapted the method described in Chapter 4.1 to take as input sequences of volumes instead of sequences of still images. I assumed the data periodicity did not change throughout the acquisition process. I also assume the data was acquired one volume after another, and not as slice-by-slice time sequences. I assumed the initial phase of each volumetric acquisition to be arbitrary.

#### 4.A.1 Method

Similarly to Chapter 4.1 I first sorted the data with the method proposed in Chapter 2, but volume-wise instead frame-wise. Then, I estimated the period of the data on the Z axis by shifting the sequences at each slice (XYT) instead of lines (XT).

#### 4.A.2 Preliminary results on simulated data

Fig. 4.10 (a) shows a XZ view of a raw volume (all the slices, one frame at each slice). The aberrations due to the time interval between slice acquisitions are visible as these wave-like structures. Fig. 4.10 (b) shows the reconstructed volume. We can see that there are some remaining artifacts, similarly to the image-based aberration correction. Fig. 4.10 (c) shows the ground truth volume that is aberration-free. Fig. 4.10 (d) shows the overlap between reconstruction and ground truth. The white color indicates an overlap between reconstruction

and ground truth. The green and magenta colors reveal the remaining artifacts.

### 4.A.3 Discussion and prospective future work

These preliminary results are encouraging as the reconstruction and ground truth overlap nicely, with some remaining artifacts at the fast phases of the cycle, as in Chapter 4.

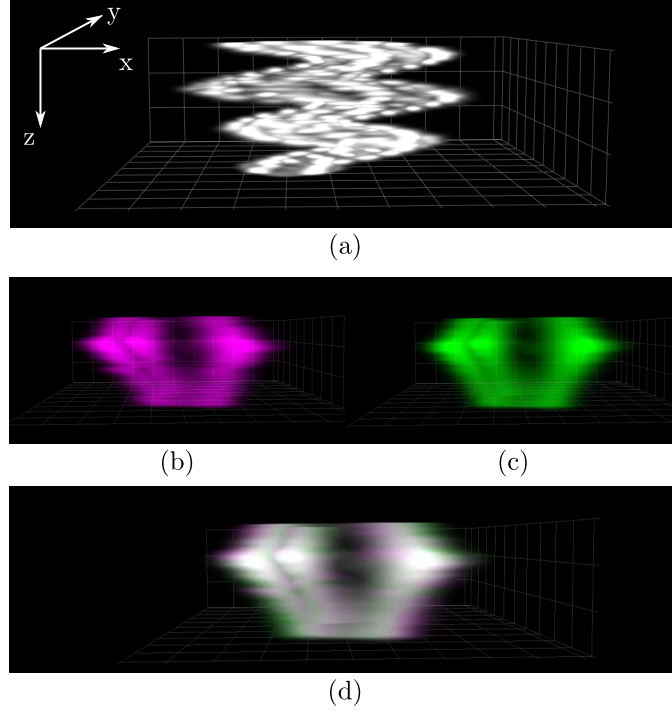


Figure 4.10 – Scanning-aberration correction on volumetric time-series. XZ views of one time-point of (a) the scanning aberration along the raw volume, (b) the reconstructed data, (c) the ground truth data. (d) XZ view of one time-point of the overlap between reconstructed data and ground truth. The white color indicates an overlap.

However, this method is built on the strong assumption that the cardiac cycle remains the same throughout the whole acquisition process. This assumption depends, among others, on a stable temperature in the acquisition chamber [68]. As the acquisition of volumes can be slow, this assumption is not easy to meet. In the synthetic data, the volume contains about 3 heartbeats, which would correspond to a volume acquisition rate of about 0.75-1.5 seconds per volume (assuming 2-4 heartbeats/sec [69]), which means 20-40 fps for a 30 slice volume (which is the size of the simulated data), but become 33-66 fps for a 50 slice volume, and this upper bound is not achievable for all the microscopes.

Volumetric reconstruction using this method would probably not beat state-of-the art methods - including our own method presented in Chapter 5. The assumption that the heartbeat is regular is too constraining in the context of acquisition of many volumes. For this method to work the cost function should be modified to allow for a refined volume-wise adjustments of



the slices.



## 5 Constrained sequence extraction for time-lapses and volumes

Live heart microscopy is an essential tool for studying the developing heart of animal models such as the zebrafish. However, developmental time-series and volumetric acquisitions are not phase-locked on conventional microscopes, which impacts any further image-based analysis. Although phase-based timelapse and volumetric recursive registration methods exist, they fail to constrain excursion errors. To address phase-based registration and recursion-based drift, we propose a method determining a smooth path in cardiac phase-development or depth space enforcing neighborhood similarity via a within-stage/depth sorting followed by a cyclical least-squares phase alignment approach that we formulate as a mixed integer linear problem. We take as input a set of still images captured at weakly-constrained times within the heartbeat cycle and over the course of development or at various depths in the heart. Constraining the paths of time-lapses by providing key-points together with enforcing local similarity successfully stabilizes the excursion error from which recursive registration approaches suffer. We characterize our method with simulated periodic data of an affine-transformation model of the heart development (linear growth) and heart drift (linear displacement), and show its applicability on experimental data.

### 5.1 Cardiac image sequence extraction from still images with unknown heartbeat phases

*In vivo* time-lapse microscopy is an important tool for developmental biology research, as it allows studying the development of organs in live animal models. When imaging developmental changes in a live heart, the acquired images can be difficult to analyze due to the heartbeat. To analyze changes on a developmental scale, the heart would ideally always be acquired at the same phase. In other words, one would need the ability to build image series in which changes in shape are solely due to processes occurring on developmental time-scale, while those related to the heartbeat, whose amplitude likely mask the more subtle underlying movements, would be discarded. This can be achieved by repeatedly examining the heart in the same phase of the cardiac cycle. Several methods and approaches have been proposed to

achieve this.

One approach consists in artificially stopping the zebrafish heart with drugs prior to imaging process then restarting it to allow for the development to proceed normally [70, 71, 72, 73]. This method has the advantage of not needing any additional hardware and software. However, stopping the heart has to be properly timed to not impact development, either because of the stopping itself [74] or because of chemical or physical changes in the medium [75].

Taylor *et al.* [2] have proposed a method that combines hardware and software for acquiring three-dimensional time-lapses of the beating zebrafish heart using a phase-locking method. This reduces the exposure time and does not require, by design, additional phase-based registration. The limitation is that it requires additional hardware and software to trigger image acquisition based on a secondary signal that captures the heartbeat and which ideally should be independent from the image signal itself. In the context of three-dimensional acquisition, Greer *et al.*, 2019 [25] proposed a setup with several cameras that can reach a 40 Hz stack acquisition rate. While such acquisition rates might be sufficient they require a specialized setup. Software-only solutions have been proposed that register (post-acquisition) movies that were acquired sequentially at different depths and developmental stages [76, 66, 27, 77]. These approaches still require the ability to image at least one heartbeat per slice at high speed.

In a different but related field, Zhang *et al.* [4] have proposed a retrospective gating method for MRI imaging based on Isomap, to reduce data dimensionality and represent the images in a two-dimensional space whose main directions they observed to correspond to breathing and heartbeat, respectively. While this approach maps the data to a low-dimensional manifold it would still require additional processing to extract sequences.

More generally, the problem of registering image sequences has been extensively studied in the field of serial-section electron microscopy to build volumetric images, in some cases also allowing for unknown sequence positions in the stack [78, 79, 80, 81, 82].

In this Chapter, we consider the problem of building image sequences that represent a still or slowly varying state in the cardiac phase, either as a function of development or imaging depth  $s$ , based on a set of still images captured at weakly-constrained times within the heartbeat cycle and over the course of development or at various depths in the heart. In all cases the cardiac phases are unknown. Our proposed approach determines a smooth path in the space of cardiac phase versus development stages or in the space of cardiac phase versus imaging depth by enforcing image similarity via a within-stage or within-depth sorting step, followed by a cyclical least-squares phase alignment approach that we formulate as a mixed integer linear problem. In order to offer wide user flexibility, the method can accommodate key-point constraints that fix the phase of the first and last images in the time-lapse or image stack, which allows to stabilize the excursion error from which recursive registration approaches suffer. We characterize our method with simulated periodic data of an affine-transformation model of the heart development (linear growth) and heart drift (linear displacement) and

determine its applicability on experimental microscopy data.

This Chapter is organized as follows. In Section 5.2 we formalize the imaging model and problem. In Section 5.3 we describe our two-step method to extracting image sequences with end-point constraints. In Section 5.7 we evaluate our method on synthetic and experimental data, and compare it to methods that rely on recursive registration of high-speed image sequences. In Section 5.11 we discuss the advantages of our proposed approach and its limitations. Finally we conclude in Section 5.12.

## 5.2 Imaging Model and Problem Statement

We consider a time-varying two-dimensional image  $f(x, y, t)$  with  $(x, y)$  representing the spatial coordinates and  $t$  the time. We assume the signal varies periodically as long as  $t$  is within limited time intervals. Specifically, we define  $i \in \mathcal{R} = \{0, \dots, R-1\}$ , an index that refers to one of  $R$  sequential image configurations of the heart. These configurations do not represent static poses but instead are characterized by the fact that the image intensity varies periodically, with a period  $T_i$ :

$$f(x, y, t) = f(x, y, t + T_i) \quad \forall t \in r_i, \quad (5.1)$$

where the  $r_i = [q_i, q_i + b]$  are time intervals of duration  $b$  (which we assume much longer than the heartbeat period  $T_i$ ), and with  $q_i$  the starting point of the interval that coincides with the start of an underlying cycle (heartbeat phase is zero). In the context of cardiac developmental biology image, the configurations  $i$  represent fixed developmental stages (increasing with  $i$ ), during which heart growth and drift are negligible. Alternatively, the configurations  $i$  could represent the depths at which a movie was acquired while slowly scanning an optical section through the heart while the camera continuously acquires images. We denote by  $\mathbf{f}_i[\cdot, \cdot, \cdot]$  a discrete image series representative of configuration  $i$  that covers exactly one heartbeat:

$$\mathbf{f}_i[k, \ell, n] = f_i(k\Delta_x, \ell\Delta_y, q_i + n\Delta_i), \quad (5.2)$$

where  $\Delta_x$  and  $\Delta_y$  are the pixel width and height, respectively,  $(k, \ell) \in \mathcal{K} = \{0, \dots, K-1\} \times \{0, \dots, L-1\}$  are the row and column index pairs,  $n \in \mathcal{N} = \{0, \dots, N-1\}$  denotes the time frame index with  $q_i$  that both marks the start of an interval and coincides with the underlying phase's zero. Finally,  $\Delta_i = \frac{T_i}{N}$  is a time step that regularly samples  $T_i$  the duration of one heartbeat at that configuration step.

Given that  $\Delta_i$  should be sufficiently small to resolve the fast motions during one heartbeat, it is typically not possible to acquire  $\mathbf{f}$  directly. Therefore, we consider the image series  $\mathbf{g}_i[k, \ell, n]$ ,  $(k, \ell) \in \mathcal{K}$ ,  $n \in \mathcal{N}$ ,  $i \in \mathcal{R}$ :

$$\mathbf{g}_i[k, \ell, n] = f(k\Delta_x, \ell\Delta_y, q_i + t_{n,i}), \quad (5.3)$$

where the  $t_{n,i}$  denote the times at which the frames are acquired in time interval  $r_i$ . Specifically,

these acquisitions occur at arbitrarily spaced times with:  $0 \leq t_{0,i} < \dots < t_{n,i} < \dots < t_{N-1,i} \leq b$ , in each interval  $r_i$ . We define the cardiac phase  $\phi_{n,i}$  of the  $n^{\text{th}}$  frame in interval  $r_i$ ,  $\mathbf{g}_i[k, \ell, n]$ , via the phase wrapping operation  $\phi_{n,i} = \langle t_{n,i} \rangle_{T_i} = t_{n,i} + mT_i$ , with  $m \in \mathbb{Z}$ , such that  $\phi_{n,i} \in [0, T_i)$ .

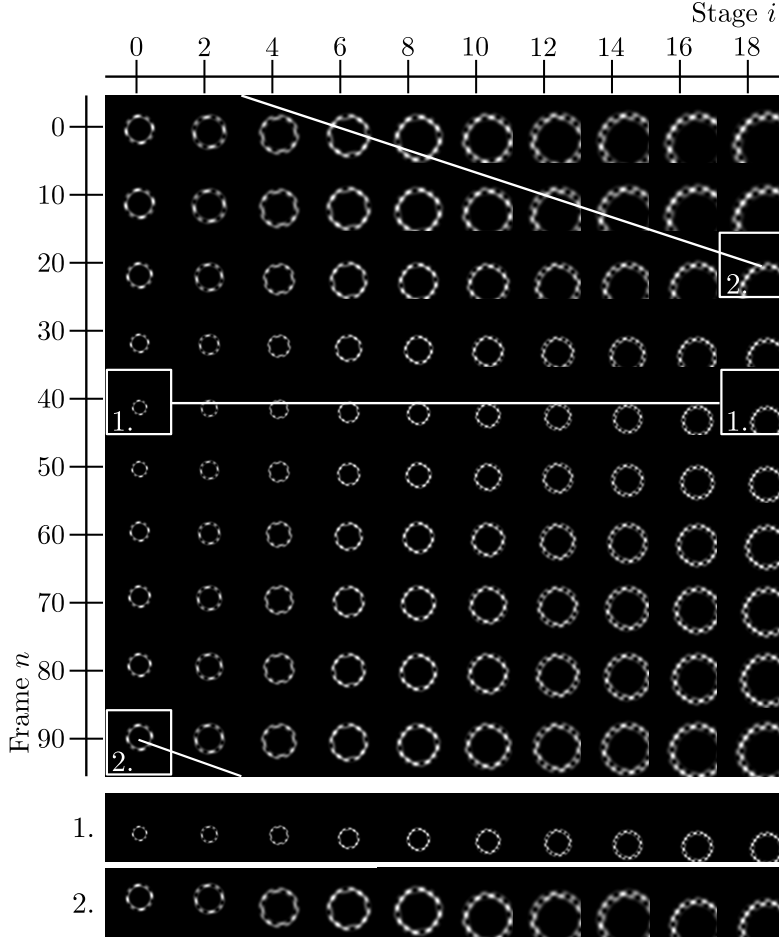


Figure 5.1 – Sequence selection in the developmental stage versus phase space. The first and last frames are selected by the user and might correspond to arbitrary phases in the cardiac cycle. Our proposed method to extract a sequence of frames to smoothly transition from the first to the last frame accounts for the periodicity of the problem to find an optimal path. An added complication is that the phases and order of the frames at each stage are unknown (not shown). 1. a desired path when the select frames in the first and last stages correspond to the same underlying cardiac phase. 2. a smooth path joining frames with differing underlying phases can feature an apparent phase discontinuity.

Given the measurements  $\mathbf{g}$  above, the problem we aim to solve is to create an image sequence  $\mathbf{h}[k, \ell, i]$  that spans all the configurations  $i$ , transitioning linearly from a first (user-specified) phase  $\bar{\phi}_0 \in \{\phi_{0,0}, \dots, \phi_{N-1,0}\}$  to a final (user-specified) phase  $\bar{\phi}_{R-1} \in \{\phi_{0,R-1}, \dots, \phi_{N-1,R-1}\}$ , such that:

$$\mathbf{h}[k, \ell, i] = \mathbf{f}_i[k, \ell, \langle m_0 + \alpha i \rangle_N], \quad (5.4)$$

where  $m_0 = (\bar{\phi}_0 / T_0)N$  is the (possibly non-integer) index that corresponds to the phase  $\bar{\phi}_0$  and  $\alpha \in (-N/(2R), N/(2R)]$  the slope to reach the final phase, such that  $\langle m_0 + \alpha(R-1) \rangle_N = m_{R-1}$ .

### 5.3 Methods

We aim at determining a sequence of images that form a smooth transition from user-selected phases (frames) in the sequence corresponding to the first ( $i=1$ ) and in the last ( $i=R-1$ ) configuration, given the acquired sequences  $\mathbf{g}_i[k, \ell, n]$ . Fig. 5.1 shows two different types of path, one with the same initial and final phases, and one with different phases, which correspond to different user selections. While determining a sequence by picking one image from each stage  $i$  directly might seem appealing, given the phases, or even the image order with each configuration stage  $i$  are not known, such sequence might lead to abrupt rather than smooth transitions. We therefore opted for a two-step approach in which we first sort the images within each stage, such as to be able to estimate phase relations based on entire sequences rather than individual frames.

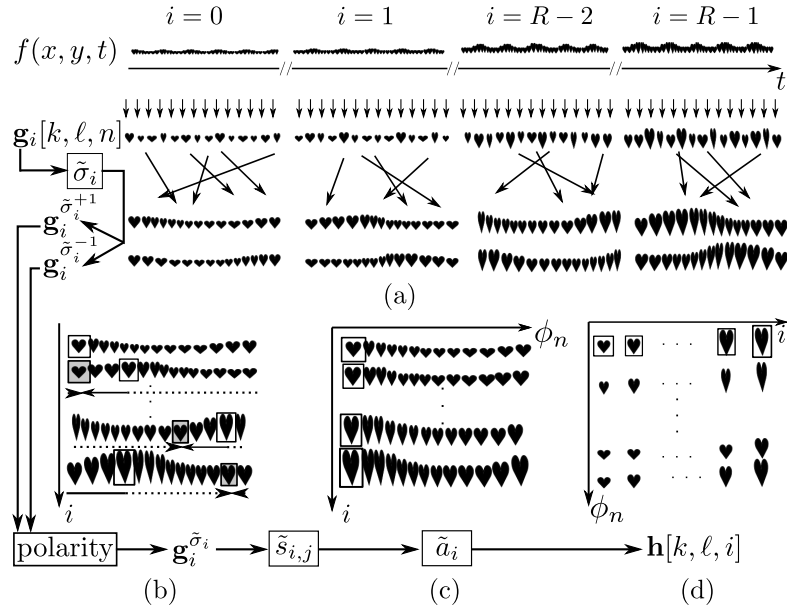


Figure 5.2 – Method overview. (a) The signal  $f(x, y, t)$  is acquired as a discrete signal  $\mathbf{g}_i[k, \ell, n]$  (5.3). The acquired signal is then sorted according to phase [26]  $\tilde{\mathbf{g}}_i^{\tilde{\sigma}_i}$  without knowledge of polarity. (b) We find the polarity together with the relative shifts between consecutive stages  $i$  (5.5). (c) Then, we solve (5.7) to find the absolute shifts  $\tilde{a}_i$  of each stage  $i$ . (d) Finally, we apply the absolute shifts  $\tilde{a}_i$  to the sorted sequences (5.10) such that the sequences of each stage  $i$  are in the same phase order and can be shown as single-phase sequences  $\mathbf{h}[k, \ell, i]$ .

## 5.4 Sorting frames acquired within an interval $r_i$

To sort the frames acquired within each time interval  $r_i$  to form a sequence that represents a single period, we create a permuted frame sequence  $\mathbf{g}_i^{\tilde{\sigma}_i}$  with  $\tilde{\sigma}_i$  denoting the permutation, such that the underlying phases  $\phi_{n,i}$  of  $\mathbf{g}_i$  are in increasing order after the permutation. For this step, we follow the method we previously proposed [26]. Briefly, the method proceeds by minimizing the frame-to-frame image difference, which is formulated as a travelling salesman problem that can be solved with efficient methods [34] (we use the commercial optimizer CPLEX 12.10 [83] but others may be suitable as well). While this approach retrieves frame order, it can return either of two equivalent solutions: the sorted sequences can be in either temporal direction, i.e. polarity is unknown. We denote those sequences as  $\mathbf{g}_i^{\tilde{\sigma}_i^{+1}}$  and  $\mathbf{g}_i^{\tilde{\sigma}_i^{-1}}$ , where the sign indicates the sequence temporal direction (Fig. 5.2 (a)). We will correct for direction with respect to the first time interval  $r_0$  together with relative phase alignment in the next section.

## 5.5 Relative phase-shift between consecutive sequences

To minimize the phase-to-phase difference between consecutive sequences, we calculate the discrete relative frame shifts  $\tilde{s}_{i,j}$  corresponding to the optimal direction  $\mathbf{g}_i^{\tilde{\sigma}_i}[k, \ell, n] = \tilde{\mathbf{f}}_i[k, \ell, n]$ . To do so, we calculate the correlation between sequences for both temporal directions,  $C_{i,j}^1[n]$  and  $C_{i,j}^{-1}[n]$ :

$$\begin{aligned} C_{i,j}^1[n] &= \sum_{k,\ell} \mathcal{F}^{-1} \left\{ \mathcal{F}^* \left\{ \mathbf{g}_j^{\tilde{\sigma}_j^1} \right\} \cdot \mathcal{F} \left\{ \mathbf{g}_i^{\tilde{\sigma}_i^1} \right\} \right\} [k, \ell, n] \\ C_{i,j}^{-1}[n] &= \sum_{k,\ell} \mathcal{F}^{-1} \left\{ \mathcal{F} \left\{ \mathbf{g}_j^{\tilde{\sigma}_j^1} \right\} \cdot \mathcal{F}^* \left\{ \mathbf{g}_i^{\tilde{\sigma}_i^1} \right\} \right\} [k, \ell, n] \end{aligned} \quad (5.5)$$

where  $\mathcal{F}$  is the discrete Fourier transform,  $\mathcal{F}^{-1}$  the discrete inverse Fourier transform, and the operator  $*$  indicates the complex conjugate. We then choose the maximum value in either  $C_{i,j}^1[n]$  and  $C_{i,j}^{-1}[n]$  to determine both the phase shift and direction:

$$(\tilde{s}_{i,j}, \tilde{p}_{i,j}) = \underset{n \in N, p \in \{-1, 1\}}{\operatorname{argmax}} C_{i,j}^p[n], \quad (5.6)$$

where  $\tilde{s}_{i,j}$  is the phase shift of  $\mathbf{g}_j^{\tilde{\sigma}_j}$  relative to  $\mathbf{g}_i^{\tilde{\sigma}_i}$  with the maximal correlation value and thus the optimal shift, and  $\tilde{p}_{i,j}$  the corresponding polarity.

While we estimate the polarity of sequences based on comparisons between consecutive sequences only, i.e. stages  $i$  and  $j=i+1$ , we calculate the relative shifts  $\tilde{s}_{i,j}$  between all sequence pairs  $i$  and  $j=i+d$ , with  $d \in \{i+1, R-1\}$  the distance between them (Fig. 5.2 (b)).



## 5.6 Sequence extraction

With images sorted by increasing phase order for each configuration  $i$ , we now turn to the problem of extracting one image from each sequence  $\mathbf{g}_i^{\tilde{\sigma}_i}$  such as to smoothly transition from the frame specified for  $i=0$  to the frame specified for  $i=R-1$ . We proceed by circularly shifting the frames of the entire sequence  $\mathbf{g}_i^{\tilde{\sigma}_i}$  instead of just selecting one image. To find the optimal phase shifts  $\tilde{a}_i \in [0, N]$  at each time interval  $r_i$ , we propose to first determine the best pair-wise relative shifts  $\tilde{s}_{i,j}$  between sequence pairs  $i, j$ , which we happen to have already computed in Eq. (5.5). The absolute shifts  $\tilde{a}_i$  must be such that when they are subtracted they satisfy the measured relative shifts  $\tilde{s}_{i,j}$  as closely as possible, but only up to an integer period term  $k_{i,d}$ . Furthermore, since the user is free to select start and end frames that have different underlying phases, we must allow for an unknown linear phase drift factor  $\alpha$  to smoothly transition between these frames. This results in the following minimization problem:

$$\tilde{a}_i = \min_{\mathbf{a}', \mathbf{k}', \alpha'} \sum_{d=1}^{R-1} \sum_{i=0}^{R-1-d} \left| a'_{i+d} - a'_i - \tilde{s}_{i,d} + k'_{i,d} + \alpha' d \right| \quad (5.7)$$

where  $\tilde{a}_i \in [0, 1)$  are the normalized absolute phase shifts.  $a'_0$  and  $a'_{R-1}$  are the phase shifts for the first and last time intervals and are fixed by the user.  $\mathbf{a}'$  is the vector containing the normalized absolute shifts and has size  $1 \times R$ ,  $\mathbf{k}'$  is a vector of size  $1 \times R$  that contains terms that are all binary and allows taking into account the periodicity of the problem.  $\tilde{s}_{i,d} = \tilde{s}_{i,d} / N$  are the normalized relative shifts calculated from the data with (5.5),  $k'_{i,d} \in \{0, 1\}$  is a binary term, and  $\alpha' = \alpha / N \in [-1/(2R), 1/(2R)]$  is the drifting factor, which controls the slope and applies to the distance  $d = j - i$ . To solve the linear programming minimization problem (5.7) we introduce the slack variables  $y_{i,d} \in [\epsilon, 1]$  and minimize the objective function:

$$\min_{y_{i,d}} \sum_{d=1}^{R-1} \sum_{i=0}^{R-1-d} w_d y_{i,d}, \quad (5.8)$$

with constraints:

$$\begin{cases} (a'_{i+d} - a'_i - \tilde{s}_{i,d} + k'_{i,d} + \alpha' d) \leq y_{i,d} \\ (a'_{i+d} - a'_i - \tilde{s}_{i,d} + k'_{i,d} + \alpha' d) \geq -y_{i,d}, \end{cases} \quad (5.9)$$

which is equivalent to (5.7), except for the weights  $w_d = 1/d$  that favor measurements between close neighbors. We solve the minimization problem (5.8) by using the CPLEX solver [83] and also retrieve the absolute shifts  $\tilde{a}_i$  (Fig. 5.2 (c)).

The sequence that joins phase  $\phi_{n,0}$  in the first configuration to phase  $\phi_{n,R-1}$  in the last configuration can be extracted starting from any time point  $n$  (Fig. 5.2 (d)), and  $\mathbf{h}[k, \ell, i]$  from (5.4) simply via the operation:

$$\mathbf{h}[k, \ell, i] = \mathbf{g}_i^{\tilde{\sigma}_i}[k, \ell, \langle n - \tilde{a}_i N \rangle_N] \quad (5.10)$$

## 5.7 Experiments

To characterize our method and compare it to alternative methods we set up an evaluation procedure on synthetic data that allows calculating the error of our estimated absolute shift with respect to a ground truth, under variably reliable relative-shift measurements, which we describe in Section 5.8. We then compare our method to a recursive registration method [13] in Section 5.9. Finally, we illustrate the applicability of our method in practice by reconstructing a time-lapse of the beating and developing zebrafish heart in Section 5.10.

### 5.8 Method characterization using synthetic data

Since we previously characterized the accuracy of our sorting method [26], we focused on characterizing the accuracy of the global phase registration method described in Section 5.6.

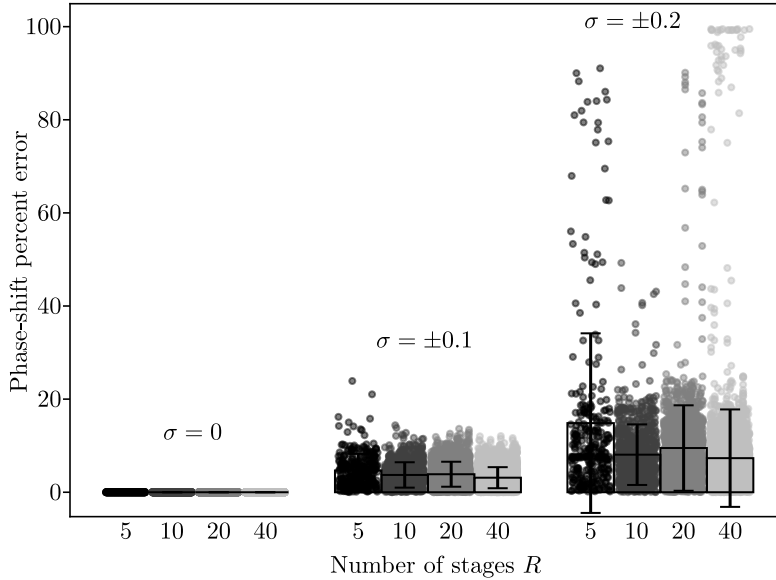


Figure 5.3 – Phase-shift error quantification. We sampled absolute shifts  $a_i$  from a random uniform distribution  $\sim \mathcal{U}(0, 1)$  that simulate shifts from a signal with a period  $T=1$ . We calculated the corresponding relative shifts  $\tilde{s}_{i,j}$ , and added three levels of noise sampled from a random uniform distribution ( $\sim \mathcal{U}(-\sigma, \sigma)$ ), with  $\sigma=0$  (no noise),  $\sigma=\pm 0.1$  (error of  $\pm 10$  frames for a 100 frames signal), and  $\sigma=\pm 0.2$  (error of  $\pm 20$  frames for a 100 frames signal). The calculated shift error is expressed in percent of period. Each vertical line of dots represents the shift error for all the stages  $i$  of an individual repeat. We simulated 100 repeats per noise level and number of stages  $R$ , so there are  $100 \cdot R$  dots per column. The mean values are shown as boxes, and the standard deviation as error bars. Our method allows to perfectly find the absolute shifts from the noise-free relative shifts ( $\sigma=0$ ). With  $\sigma=\pm 0.1$ , the output noise levels are as a mean below 20%, except for  $R=5$  that has some individual stages  $i$  with an error above 20%. For  $\sigma=\pm 0.2$ , which is a high noise level, we get a higher occurrence of stages  $i$  that are strongly displaced.

### 5.8.1 Phase error characterization

We simulated ground truth data with known absolute phase shifts (with respect to an underlying, fixed periodic process) by sampling values from a random uniform distribution  $a_i \sim \mathcal{U}(0, 1)$ , then calculated the corresponding relative shifts  $s_{i,j}$  and added random (uniformly-distributed) noise  $\sim \mathcal{U}(-\sigma, \sigma)$  with  $\sigma \in \{0, 0.1, 0.2\}$ . We then used our method to estimate the absolute shifts  $\tilde{a}_i$  and calculated the registration error for  $R \in \{5, 10, 20, 40\}$  stages. We repeated the noise sampling 100 times for each noise level to show the error distribution. We calculated the error as the difference between the noiseless absolute shift  $a_i$  and the output absolute shift  $\tilde{a}_i$ :

$$\min\{|a_i - \tilde{a}_i|, |1 - a_i + \tilde{a}_i|\} \cdot 100, \quad (5.11)$$

which takes into account the periodicity of the signal and scales the phase-shift error as a percent of the period, such that an error of 100% corresponds to a phase-shift of  $T/2$ . Fig. 5.3 shows that the output error mean and standard deviation (shown as boxes and bars) follow the input noise levels.

## 5.9 Comparison to existing methods

To compare the performance of our method to alternative software-based methods, we simulated 20 synthetic datasets of developing hearts for  $R = \{5, 10, 20, 40\}$ . We compared the phase-shift error trends of our method to those obtained via a recursive registration method [13] (initially designed for sequences acquired with high speed microscopes).

### 5.9.1 Time-lapse data acquisition simulation

We simulated the acquisition of a beating heart as previously described in [12]. We simulated the acquisition of  $\mathbf{f}_i[k, \ell, n]$ , with  $k=0, \dots, 255$ ,  $\ell=0, \dots, 255$ , and 10,000 frames. Our signal  $\mathbf{f}$ , which consists of images of a contracting ring, has a period  $T=6\pi$ . We chose an irrational period to avoid sampling the exact same phase twice and thus more realistically the situation encountered when acquiring experimental data. We fixed the number of frames per sequence to  $N=100$ . We thus ignored 1900, 900, 400, and 150 frames in between each consecutive sequence of 100 frames to get  $R=5, 10, 20$ , and 40 stages, while keeping a similar synthetic growth for all datasets. We simulated the development of the heart and the animal model with an affine-transform growth model. We linearly increased the mean diameter of the simulated heart from 70 to 160 pixels. Additionally, we simulated the animal's drift by linearly displacing the center of the simulated heart by 60 pixels both horizontally and vertically. Fig. 5.4 (a) shows the sorted frames from the first stage. Our simulation has a scaling and vertical displacement factor, which produces an asymmetric motion pattern. Fig. 5.4 (b) shows the first frame of each sequence of the contracting ring before the phase registration step. The centers of the rings do not follow the linear model of displacement as the linear displacement is intermingled with the periodic vertical displacement. After registration, Fig. 5.4 (c), the centers of the rings follow

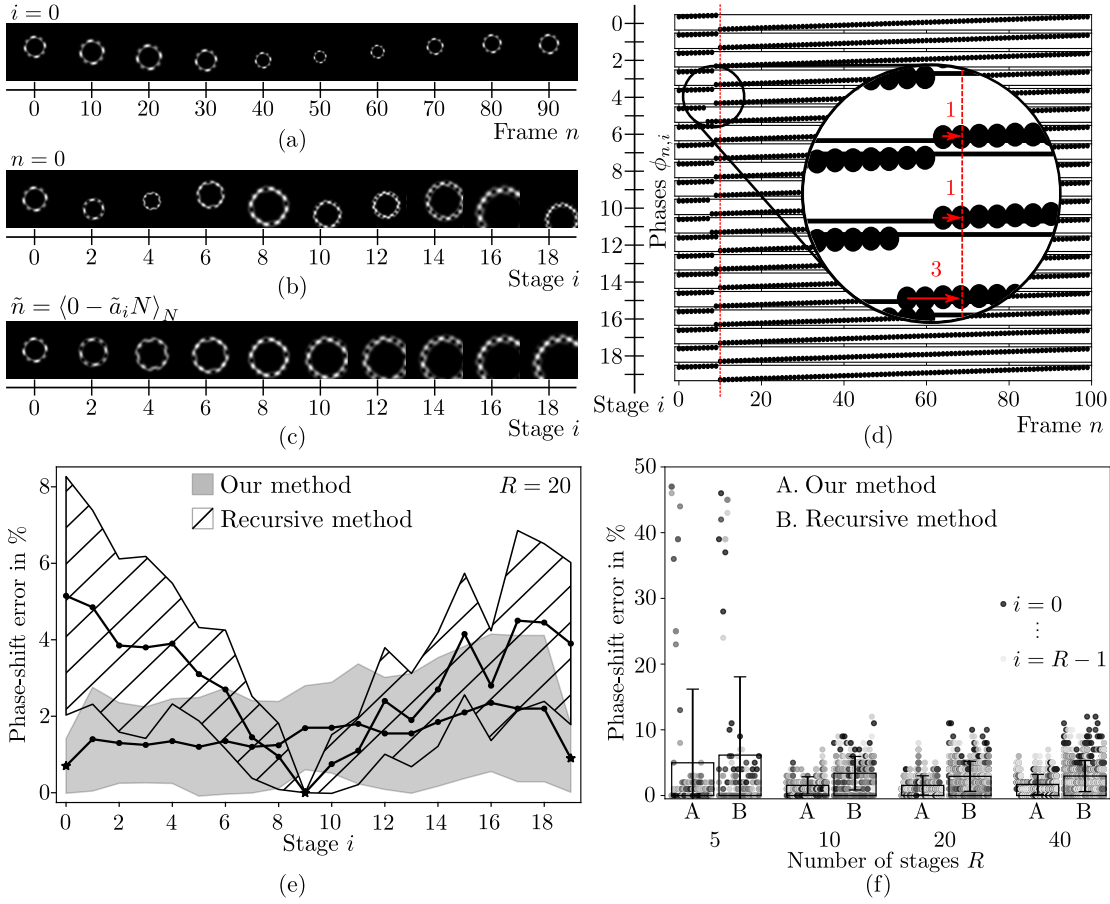


Figure 5.4 – Synthetic time-lapse of the beating heart. (a) Sorted frames for  $i=0$ . The period has a scaling and a vertical translation factor, which produces asymmetry. (b) Simulation of the developing beating heart before registration. The images represent the first frame  $n=0$  of each stage  $i=0, 2, \dots, 18$ . The sine-like displacement of the center of each circle shows a lack of alignment. (c) Simulation of the developing beating heart, after registration. The images show the first frame  $\tilde{n} = \langle 0 - \tilde{a}_i N \rangle_N$  of each stage  $i=0, 2, \dots, 18$  of the sorted and registered data. The linear displacement of the center of the circles follows our developmental model. (d) Example of registered phases, with each graph representing one stage  $i$ . The phase jump represents the jump from  $\phi_{n,i}=T$  to  $\phi_{n+1,i}=0$ . The magnification shows the integer shift error calculation whose mean and standard deviations are shown in (e). The vertical red line shows the ground truth minimum phase index. (e) Realignment error quantification and comparison to the state-of-the-art recursive method for  $R=20$ . The state-of-the-art registration method mean (solid line) with standard deviation (hatched) starts the registration from the central stage (star symbol). The error increases with the distance to the central reference time-series to reach around 8%. Our method error mean (solid line) with standard deviation (filled) fixes the first and last phases (star symbols), reducing the excursion error to a maximum of 4%. We simulated 20 datasets with initial phases linearly distributed  $\in [0, T)$ . (f) Each dot is an error calculated in (d). The boxes are the mean and the error bar the standard deviation, as shown in detail in (e).

a linear displacement that accurately recovers the underlying growth model, thus effectively removing the rapid vertical displacement motion that would hide the underlying growth.

### 5.9.2 Comparison of excursion error

To quantify the excursion error, we calculated the shift compared to a ground truth sequence (using (5.5)-(5.6)) and compensated for periodicity (5.11) for each stage  $i$  (Fig. 5.4 (d)). The ground truth minimum phase location is represented by a vertical red line. In the magnified view, the shifting error is shown as a red arrow between the estimated shift and the ground truth shift.

We calculated the phase excursion error obtained through our proposed method and via the recursive registration method [84]. The solid lines in Fig. 5.4 (e) represent the mean excursion error. The filled area is the standard deviation of our method. The stars at the first and last stages are the fixed user-selected phases. The hatched area is the standard deviation of the recursive registration method, and the star at the central stage is the reference stage  $i = \lfloor N/2 + 0.5 \rfloor$ .

Fig. 5.4 (f) is higher-level view of both Fig. 5.4 (d) and Fig. 5.4 (e) featuring stages  $R = \{5, 10, 20, 40\}$ . Each dot in Fig. 5.4 (f) is an error shown as a red number in the magnification in Fig. 5.4 (d). Fig. 5.4 (e) shows the mean and standard deviation for  $R=20$  that can be seen as box plots and error bars in Fig. 5.4 (f) 20, columns A and B. The brightness of the dots vary with the stage value (dark to light for first to last stages). Each column of dots represents one dataset.

### 5.9.3 Excursion error on simulated volumetric data

To illustrate the excursion error in a volumetric dataset (where different configurations  $i$  correspond to depths  $z$  through the sample), we simulated the acquisition of data using the periodic and asymmetric model of Section 5.9.1. We simulated a dataset that comprising 50 volumes, creating sequences of 50 frames at each slice  $z$ . We added a phase-shift factor of  $1.3T/Z$  between consecutive  $z$ , leading to a 1.3 period difference between  $z=0$  and  $z=Z-1$ , for  $z \in 0, \dots, Z-1$ ,  $Z$  the total number of slices in each volume. Here,  $Z=50$ . We then sorted each sequence (slice  $z$ ), then applied our method and the recursive registration method. Fig. 5.5 shows the sorted (not registered) data, the recursive method results, our method's results, and the ground truth. Fig. 5.5 (a) shows a volumetric view oriented in the XZ direction at frame  $n=0$ , and Fig. 5.5 (b) shows the XZ plane at frame  $n=24$ , the middle frame. Fig. 5.5 (c) shows a volumetric view oriented in the YZ direction at frame  $n=0$ , and Fig. 5.5 (d) shows the YZ plane at frame  $n=24$ . As shown in Fig. 5.4 (e), the excursion in the recursive method is highest on the extremities, as the reference frame is at the center. Our method is able to limit the excursion error, as the first and last frames are fixed.

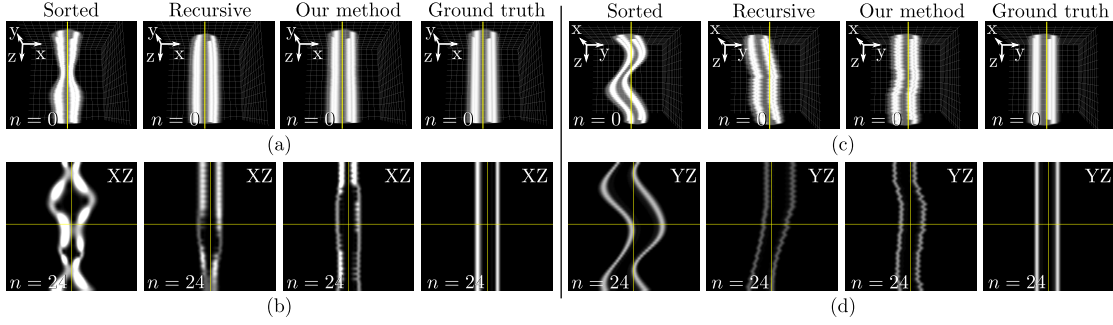


Figure 5.5 – Synthetic volumetric data reconstruction comparison. The ground truth is a textured cylinder that changes radius and position periodically. (a) and (c) volumetric view of the first frame  $n=0$ . (b) and (d) slice view of the central frame  $n=24$ . (a) and (b) XZ view of the simulated data. (c) and (d) YZ view of the simulated data. The recursive method registers the sorted data from the central slice, which results in a drift at the external slices. Our method fixes the first and last slice, limiting the excursion error.

## 5.10 Validation on experimental data

To evaluate the potential of our method in a live microscopy imaging context, we acquired the beating heart of live zebrafish embryos. We bred Et(-26.5Hsa.WT1-gata2:EGFP)cn12 (epi:GFP) [85] and Tg(myl7:GFP)[38] zebrafish to produce lines expressing red fluorescent proteins in the heart and green fluorescent proteins in proepicardial cells that are on and around the heart wall, and green fluorescent proteins in the heart, respectively. We followed standard procedures [39]. All procedures were previously authorized by the Veterinary Office of the Canton of Bern, Switzerland, for conformity. We grew the zebrafish embryos in E3 medium and added PTU (0.003% 1-phenyl-2-thiourea) to avoid pigmentation when the embryos reached an age of 24 hours post fertilization (hpf). At an age of 36 hpf, we removed the chorion surrounding the embryos with forceps and anesthetized the embryos with Tricaine at 0.08 mg/ml, pH 7. We embedded the embryos with the ventral side down on a glass bottom dish in 1% low melting agarose (Promega). We imaged the beating heart on a Leica TCS SP8 inverted confocal microscope with an HC PL APO 20x/0.75 IMM CS2 objective lens. The two fluorescent channels were acquired simultaneously.

### 5.10.1 Timelapse of the beating heart

To further test our method in practice, we imaged an Et(-26.5Hsa.WT1-gata2:EGFP)cn12 (epi:GFP) zebrafish embryos starting at 36 hpf and acquired 100,000 frames, consecutively, every 0.13 seconds (about 7.6 frames per second). We loaded the data by batch of  $N=100$  consecutive images, then skipped 2900 images, to reach  $R=33$  stages. This corresponds to a duration of  $b=13$  seconds per stage, then a delay of 6.28 minutes before the next stage (see Chapter 5 Supplementary Movie 1). We sorted and registered the developmental stages (Chapter 5 Supplementary Movie 2). We then extracted one registered phase at each stage (Chapter 5 Supplementary Movie 3). Fig. 5.6 shows stages  $i=0, 6, 12, 18, 24, 30$  (Fig. 5.6 (a)–(f))

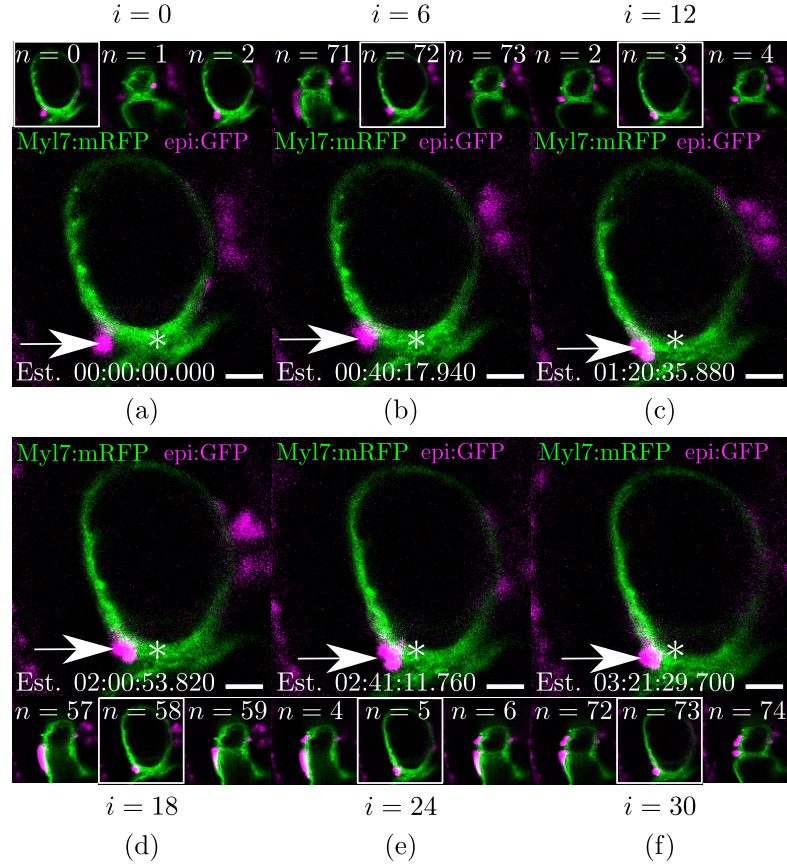


Figure 5.6 – Time-lapse result of a zebrafish embryo heart development over 3 hours and 36 minutes (see Chapter 5 Supplementary Movie 1). (a) Stage  $i=0$ , (b) stage  $i=6$ , (c) stage  $i=12$ , (d) stage  $i=18$ , (e) stage  $i=24$ , (f) stage  $i=30$ . The big images represent the output time-lapse images. The thumbnail images above ((a)–(c)) and below ((d)–(f)) show those images in their raw data context (see Chapter 5 Supplementary Movie 2). The surrounding white square shows the selected image. The star  $\star$  is at the same location on each image and shows the drift due to the heart and animal growth. The arrow point toward a cell that can easily be followed through the time-lapse. Scale bar is  $20\mu\text{m}$

of the same phase of the registered data. The star in the image is set at the same location, and shows the drift created by the animal growth. The arrow shows a cell on the heart, that is easy to follow when the phases are aligned.

### 5.10.2 Volume reconstruction

To show the applicability of our method on volume registration, we acquired 20 frames at 46  $z$  positions of Tg(myl7:GFP) embryos at 52 hpf. Fig. 5.7 shows the sorted data (not registered) and the data registered using our method. (Fig. 5.7 (a) and (b)) show a XZ orientation of the heart and (Fig. 5.7 (c) and (d)) show a YZ orientation of the heart. The sorted data in frame  $n=0$  (Fig. 5.7 (a) and (c)) and  $n=10$  (Fig. 5.7 (b) and (d)) is similar as each slice featuring a different

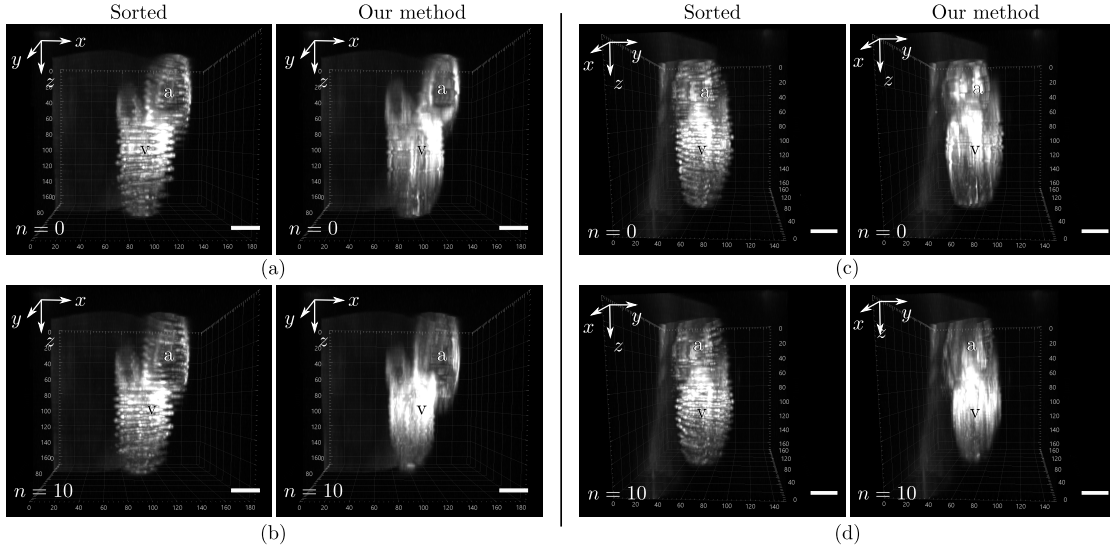


Figure 5.7 – Volumetric registration of experimental data. (a) and (c) first frame  $n=0$ . (b) and (d) middle frame  $n=10$ . (a) and (b) show an XZ view of the sorted (not registered) data and the results of our method, respectively. (c) and (d) show an YZ view of the sorted (not registered) data and the results of our method, respectively. The sorted data look similar in both featured frames as the heartbeat is lost due to the lack of synchronization between the slices of the volume. Our method recovers the heartbeat, which can be seen as the chambers in frame  $n=0$  have a different volume as the chambers of frame  $n=10$ . The atrium (white letter a) is smaller in frame  $n=0$  than  $n=10$ , whereas the ventricle (black letter v) is bigger in frame  $n=0$  than  $n=10$ . As this dataset only has 20 frames, there is some jitter at fast moving part of the period, as is the case in the first frame  $n=0$ . The central frame  $n=10$  features a slower part of the heartbeat, resulting in much less jitter between successive slices. Scale bar is  $30\mu m$ . See Chapter 5 Supplementary Movie 4

phase results in an average heart. With our method, frame  $n=0$  and  $n=10$  show different phases of the heartbeat, which can be observed with the volume of the heart chambers. The atrium (white letter a) is smaller in frame  $n=0$  than  $n=10$ , whereas the ventricle (black letter v) is bigger in frame  $n=0$  than  $n=10$ . In frame  $n=0$  we can see some misalignment remaining between consecutive  $z$  slices, probably due to the fact that the dataset only has 20 frames in the time axis. On faster moving part of the heartbeat, as in frame  $n=0$ , a small difference in phase will translate to a notable difference in the image. In frame  $n=10$ , a slower moving part of the heartbeat, these phase differences are negligible, exemplifying that reliable three-dimensional cardiac shapes can be recovered even using relatively low frame-rates and few images per heartbeat.

## 5.11 Discussion

Our method registers sequences of the beating heart through developmental time or depths through volumes in two steps. First, we sort frames in each sequence to cover one full heart-



beat, which we can achieve without requiring any knowledge of the underlying phase nor the heartbeat period, as we previously showed in [45]. Next, we register the sequences. Our method expects the user to choose frames in the first and last sequences, but does not necessarily require for those phases to be the same (Fig. 5.1). This allows more flexibility in data analysis, as features of interest might not always be visible at the same phase throughout the whole dataset. This approach could also directly take advantage of an external phase signal if it was available.

We assessed the impact of unreliable relative sequence registration input on the quality of the overall reconstruction (Fig. 5.3). The resulting mean and standard deviation of the reconstruction error for all datasets closely follows the quality of the input inaccuracies, yet limits the excursion error by constraining the end-point. In order to be able to analyze a fixed-phase timelapse it appears necessary that the inaccuracy on the relative phase shift estimates does not exceed 10%, as this level has a small standard deviation and a low number of outliers, which would otherwise compromise reliable visual analyses.

To compare our method to the recursive registration method, we simulated a time-lapse dataset of a developing heart that assumed that the changes in shape and position are slow, and that there are similarities between the first stage and the last stage. If the structural similarities were to be too important between the first and last stages, one could add additional keyframes and apply our method sequentially on successive parts of the dataset. The recursive registration method we compared ourselves to uses the central time-series as reference, and recursively registers the other stages. As a result, the error grows with the distance to this central stage. This can be further seen in Fig. 5.4 (f), as the lighter and darker dots show the highest error rate, whereas our method shows a majority of medium-gray dots. The error mean and standard deviation of our method is lower for all number of stages  $R$  that we tested, and shows we successfully limit the excursion error.

To illustrate the applicability of our method on live imaging, we show the application of our method on a timelapse dataset, and a volume dataset.

The arrows in Fig. 5.6 (a)–(f) point to a single cell attached to the heart wall that is easy to follow from one image to the next. The thumbnail images above (Fig. 5.6 (a)–(c)) and below (Fig. 5.6 (d)–(f)), show those images in the raw time-series context, where this same cell is difficult to track. This can be seen dynamically in Chapter 5 Supplementary Movie 1 (raw data), Chapter 5 Supplementary Movie 2 (registered data), and Chapter 5 Supplementary Movie 3 (timelapse of one single phase).

We additionally showed that our method is applicable for volumetric registration as well. We showed in Fig. 5.7 and Chapter 5 Supplementary Movie 4 that we restored the heartbeat dynamics while limiting erroneous excursions from which unconstrained methods suffer. Fig. 5.7 shows that the excursion error is higher in faster phases of the heartbeat but stays in check via the fixed endpoints.

### 5.12 Conclusion

In this Chapter, we proposed a method to register sequences of the beating and developing heart. We characterized our method on simulated data with different levels of noise, and showed that recursive shifts with an error of up to 10% lead to an output noise that does not exceed 10%, even on an individual time-series basis. We compared our method to registration method that operates recursively and showed that we are able to lower the error by up to a factor 2 by fixing the first and last phases. We demonstrated that the method is applicable in practice, by applying it on experimental datasets of zebrafish beating hearts, for time-lapse and volume registration. This method provides a highly flexible approach that we foresee could be used with a wide range of instruments thereby improving the accessibility of time-lapse and three-dimensional imaging methods to study the developing heart.

## 6 Conclusion and perspective

In this thesis, I explored several solutions for imaging the beating zebrafish heart with speed-constrained microscopes, for different cardiac motion time-scales and hardware imaging technologies and performances.

### 6.1 Summary of contributions

In Chapter 2, I proposed a method that allows to virtually increase the framerate given a series of images, under the assumption that the underlying motion is cyclical but asymmetric. This approach is particularly promising for modalities that have too slow a framerate or whose writing bandwidth is insufficient or irregular. However, asymmetry cannot be guaranteed at all time in cardiac time series, so in Chapter 3, I propose an alternative acquisition solution, which allows sorting still images of the beating heart even when the sequence contains repeated shape configurations, without prior phase information, simply by encoding the movement in every other image with shaded motion blur through ramp illumination, effectively increasing phase-based resolution.

In Chapter 4, I proposed a method to reconstruct image series of the beating heart from scanning-aberrated microscopy images. I demonstrated that the method is applicable in practice on data from a standard confocal LSM, providing reconstruction quality similar to that of state-of-the-art fast microscopes in the slower phases of the heartbeat, with some artifacts remaining in the faster phases. I expect that this reconstruction method could be applied to other point- or line-scanning microscopy modalities. It might be a particularly interesting option for multi-photon imaging (multi-photon fluorescence, second harmonic generation, etc.), where alternatives to point scanning are few. The simulation framework I developed provides a convenient tool to establish performance and design guidelines on the critical parameters to be adjusted. Beyond simulations, together with my collaborators, we showed via an experimental procedure, that reconstructions through this method are valid, by verifying the invariance of the reconstructions under varying sample orientations with respect to the scanning direction and through direct comparison with full-field, non-scanning

imaging methods.

In Chapter 5 I proposed a method that constrains the paths of time-lapses by providing key-points together with enforcing local similarity. I showed that the method is applicable in practice on fluorescence data for phase-extractions in timelapse movies and volumetric reconstruction. This method successfully stabilizes the excursion error from which recursive registration approaches suffer. In the current context where machine learning methods are widely used, this method could also help with semi-automatic phase annotation to create a phase-based annotated dataset, with the user actively annotating the first and last phase.

Overall, this thesis opens up the possibility to use a wider variety of imaging modalities for imaging the beating heart, and allows to chose from options that were previously not available.

This thesis fills several gaps for imaging the developing heart with microscopy methods. In the light of the availability of these additional imaging options, it is possible to revisit existing and establish new guidance for live heart imaging and to help adjusting the trade-offs between temporal performance, cost, and physical and physiological constraints.

## 6.2 A short guidebook to imaging the live heart

There are several parameters to take into account to successfully image the heart. In this Section, I will discuss some possible combinations of those parameters, which broadly include resolution needs and technical knowledge.

### 6.2.1 Living or fixed?

The first decision to make is whether one needs to image a live or fixed sample. If the heart is fixed, then temporal resolution is less crucial and mostly spatial resolution has to be considered, i.e. axial and lateral resolutions of the imaging modalities.

If the heart is beating, then on top of spatial resolution, temporal resolution becomes critical as well. The choice of an imaging modality will depend on several parameters, including heartbeat frequency as compared to the scanning and image acquisition speed, the type of microscope that is potentially already available for use, budget (to build or extend existing systems), and time. A good starting point is to first determine what aspect of the live heart needs to be imaged. I will examine a few scenarios below.

### 6.2.2 Single phase imaging for the custom microscope-equipped researcher

If the goal is to image a single phase of the heartbeat, be it for a whole volume during one developmental point, or several developmental points, then several methods are available. The two methods that come to mind first are the methods from Taylor *et al.*, 2019 [2], that

prospectively gate for both volumes and timelapses, and the method from Greer *et al.*, 2019 [25], that can image a volume at seemingly a single phase. Those two methods typically do not require post-processing, those microscopes and additional hardware do not necessarily cost more than a commercially available microscope, but require a lot of know-how. Wiring the hardware physically and computationally to reach the speed and precision demonstrated in those papers is not trivial.

### 6.2.3 Commercially available microscopes as an alternative

As single-phase acquisitions are not currently implemented in commercially-available microscopes, the combination of time-series with post-processing steps is a good alternative to custom single-phase acquisition systems.

If going this route, the next steps will mostly depend on the heartbeat-to-microscope speed ratio.

#### High-speed microscope

If a high-speed microscope is available (light-sheet, spinning disk, ...) with a high framerate and a fast camera, then the method I propose in Chapter 5 can be used as a complement to realign the phases, whether in a timelapse or volume. High-speed microscopes have some trade-offs, for instance the axial resolution of a light-sheet is limited by the thickness of the sheet and a thinner light sheet has a less uniform illumination. The axial resolution of a spinning disk is limited by the distance between neighboring pinholes, or pinhole crosstalk. Dim fluorescence signals is also limiting for spinning disk microscopes.

#### Slow frame writing

If the frame acquisition rate is fast, but the camera is slow or post processing of images is necessary before saving (AiryScan module), then there will not be many frames per period, and most realignment software might struggle. One solution is to increase virtually the framerate by phase-sorting the data, as proposed in Chapter 2.

#### Slow frame acquisition

However, if one needs to image with a point-scanning confocal microscope for a better axial resolution, or if the fluorescence is dim, or if one needs to image with a scanning multi-photon microscope, the method proposed in Chapter 4 can be used. This method allows recovering the dynamics of the heartbeat and produces similar image quality as high-speed microscope in slower phases of the heartbeat, but has remaining artifact in faster phases of the heartbeat. This method offers an alternative to changing imaging modality. However, timelapse or volumetric imaging would for instance not be realistic with a slow scanning microscope due

to the amount of light the sample receives. It would typically work for time sequences.

### 6.2.4 OpenSPIM

The OpenSPIM [40], an open design of a light-sheet microscope, was proposed with the idea that everyone could then build a simple light-sheet in their own lab. This idea is true to a certain extent. Even with this publication, building a microscope still requires a lot of know-how and time to optimize it. As compared to a commercially-available microscope, it is more difficult to handle (for laser/lens alignment for instance), and the software controlling the microscope and the imaging process has to be written as well. However, the OpenSPIM has big advantages. As compared to a commercial light-sheet, an OpenSPIM is much cheaper. The imaging protocols can easily be adapted or changed, and additional hardware (such as microcontrollers for custom illumination patterns, see Chapter 3) can easily be added to the imaging pipeline. The software is not a black box, which has huge advantages as everything can be controlled or measured. It is a great solution for software- and hardware- oriented researchers.

### 6.2.5 Concluding recommendations

There are many solutions for imaging the beating heart. It is thus all the more important to have a clear idea of what the goal of the imaging process is, and what is expected to be present in the images. Each imaging modality and software have their advantages and limitations, whether physical, cost, or time. The methods and characterization procedures described in this thesis both extend the applicability range of certain instruments and allows to simulate the appropriateness of a given methodology.

## 6.3 Future perspectives

This thesis opens up a few new problems and directions that I will discuss in this Section.

### 6.3.1 Adaptive time-lapse volume acquisition

In Chapter 5, I proposed a method that limits the excursion error when registering sequences, either in time or as a volume. In the context of timelapse microscopy the data that outgrows the field of view is of course lost. I would propose an adaptive depth selection at acquisition time that takes the previous position as a starting point, and finds the new heart depth boundaries. As it is live imaging, this method could be based on local intensity variation for instance. Provided the microscope allows flexible acquisition. The post-processing realignment should then be adapted to volume with increasing number of slices. This proposed adaptive depth acquisition resonates with the importance of good data coverage explained by He *et al.*, 2020 [86], where they optimize illumination and multi-view acquisition for optimal sample

coverage.

### 6.3.2 Machine learning solutions

Machine learning (including deep learning)-based methods are increasingly being used for image processing problems. For cardiac imaging, many machine learning solutions have been developed in the medical imaging field, covering any topic from segmentation, to classification or image enhancement [87, 88, 89, 90].

In the context of neural networks, only a few methods have been proposed for zebrafish heart development [91] (segmentation of the heart chambers), [92] (segmentation of the cardiac trabecular network). The limited development of neural-network-based solutions in zebrafish live heart imaging is because, contrarily to medical imaging, a phase of the cardiac cycle can look very different depending on the experiment. The images will vary with orientation, age, and will depend on the tagged gene (where the fluorescent proteins are expressed). The issue here is the need for annotated data. A different training should be used for the different data configurations, which means different datasets of annotated data. To make this task more feasible, I would see three possible axes: the first would be to use a shallow network to limit the number of parameters and thus limit the quantity of required data. An autoencoder, which is typically for dimension reduction, could be a good start. The second would be using a pre-trained network of similar data (for instance from [91]), and re-train the last layers with additional data to fit the problem. The third solution would be completing the data with simulated data. During this thesis I have extensively used a simulation framework that includes many of the realistic noise characteristics of imaging systems. This could form the basis for training methods. However the model would need to be further developed to fit more closely the shape and fluorescence pattern of a zebrafish heart.

## 6.4 Concluding remarks

Cardiac imaging will undoubtedly continue to offer many opportunities to leverage both hardware and software technologies. The techniques that I developed both offer new practical solutions that can be used in the field as well as new cardiac imaging approaches that might form the basis for less constraining imaging approaches.





# A Microscopy and Zebrafish

## A.1 Microscopes

In this Appendix section, I present a brief overview of the microscopy techniques mentioned in the thesis.

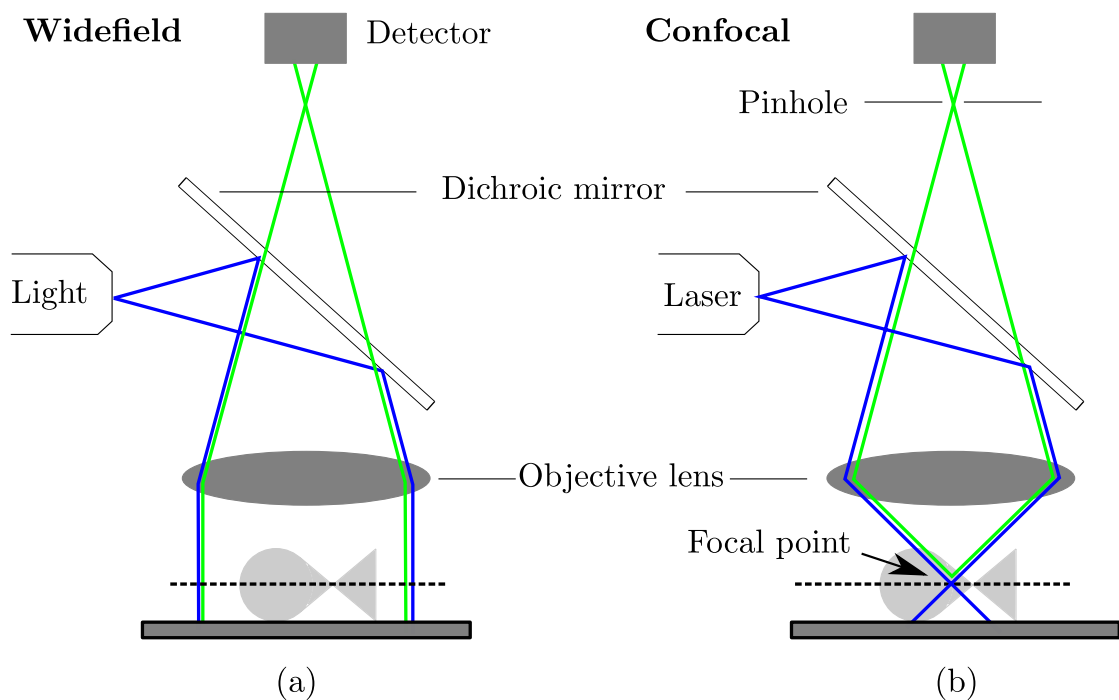


Figure A.1 – Widefield vs confocal microscopy. (a) In a widefield microscope the light goes through the whole sample and the reflected light is captured by the camera. (b) In a confocal microscope the light goes through the whole sample, but the pinhole rejects out-of-focus light, creating a thin optical sectioning, as the camera receives the light from the focal plane only.

### A.1.1 Point-scanning confocal microscope

A confocal microscope rejects out-of-focus light, which means the only light received by the detector comes from the desired plane. To do so, confocal microscopes have a pinhole at the focal plane of the objective lens thereby rejecting the out-of-focus light (Fig. A.1). The standard acquisition is thus point-wise, which means it is easy to acquire only a region of interest, but the acquisition is slow. One solution to increase the acquisition speed is using multiple pinhole, as is the case in a spinning disc confocal microscope (see Section A.1.2).

### A.1.2 Spinning disk

The spinning-disc microscope (Fig. A.2) is a confocal microscope using arrays of pinholes instead of a single pinhole. The pinholes are arranged such that with one rotation of the disc, each point of the sample is illuminated once. The advantage of a spinning disk is the frame acquisition speed. The downside is the axial resolution, as it is limited by the distance between the pinholes.

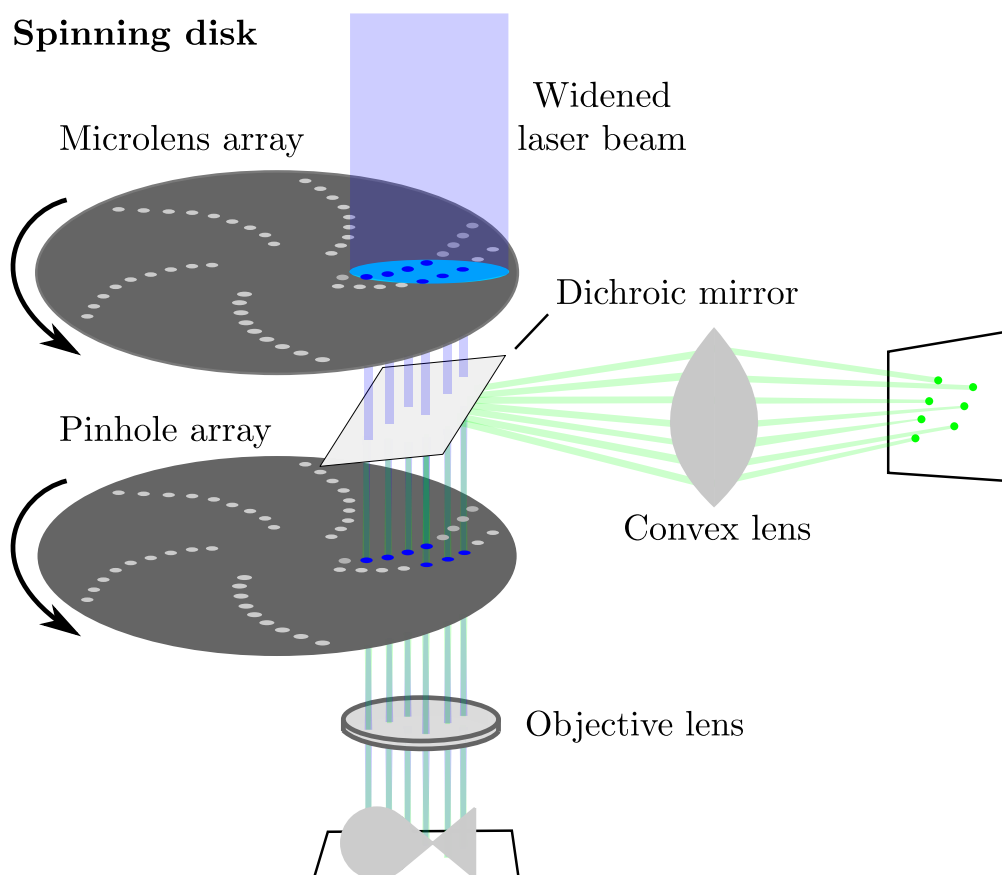


Figure A.2 – Spinning disk microscope. The laser light goes through spinning disks of microlenses and pinholes, making multiple point-wise acquisition operations at once.

### A.1.3 AiryScan module

This module was developed by Zeiss [50], and the principle of the AiryScan is that instead of a Photon Multiplier Tube (as in a standard point-scanning confocal microscope) or a linear array of detector, the detector is composed of 32 detectors in a honeycomb shape. The light from the laser is projected onto the honeycomb, thereby mapping the point-spread function. The pinhole is produced virtually, through binning of Airy rings. A deconvolution step is necessary. The Airyscan module increases both the lateral and axial resolutions, but the framerate is slow due to the processing steps.

### A.1.4 Two-photon microscopy

Two-photon (or multi-photon) microscopy is a fluorescence microscopy technique that sends two low-energy photons to excite a fluorescent molecule. Contrarily to standard fluorescence microscopy, by arriving at nearly the same time, the energy of the photons will cumulate (Fig. A.3).

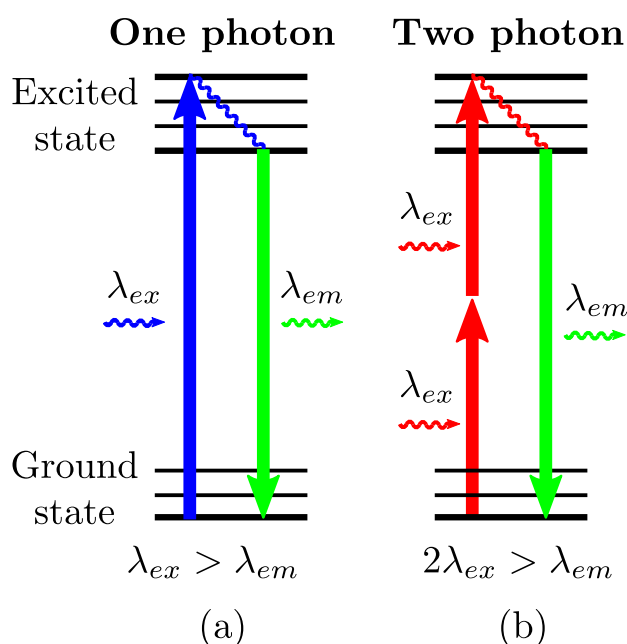


Figure A.3 – (a) One-photon microscopy. The excitation wavelength  $\lambda_{ex}$  has to be high enough ( $\lambda_{ex} > \lambda_{em}$ ) to push electrons in the excited state. (b) Two-photon microscopy. As two photons reach the electrons simultaneously, only half the wavelength is necessary, as the energies of the two photons cumulate.

The advantage of this technique is two-fold. First, low-energy photons (typically near-infrared to infrared wavelength) penetrate deeper in the tissue, and the cumulation of energies allows for fluorophores excited by higher energy photons to be excited by photons with a higher wavelength. Second, the transition probability depends on the square of the excitation intensity (since there are two photons), which excludes the occurrence of out-of-focus fluorescence,

i.e. there is fluorescence only where the beam is more intense and focused. [93].

### A.2 Zebrafish heart development

This section gives a brief overview on the zebrafish model and as a model for live heart imaging. It is meant to give an idea of the magnitude in terms of size and developmental time.

As nicely explained by Nguyen *et al.*, 2012 [94], Genge *et al.*, 2016 [95], and Giardoglou *et al.*, 2019 [96], the zebrafish has been used as an animal model for heart development for its many advantages. Namely, they are relatively easy to manipulate genetically, they are small (less than 1 cm), lay many eggs (i.e. large number of offspring), the embryos develop fast, and can be maintained transparent with no noticeable impact on heart development until several days post fertilization with the use of a chemical (1-phenyl-2-thiourea). Moreover, zebrafish embryos can reach their necessary oxygen levels through passive diffusion and don't need to swim to get enough oxygen. They can thus be immobilized for a few days without impacting their development. All of those qualities made them excellent candidates for optical microscopy.

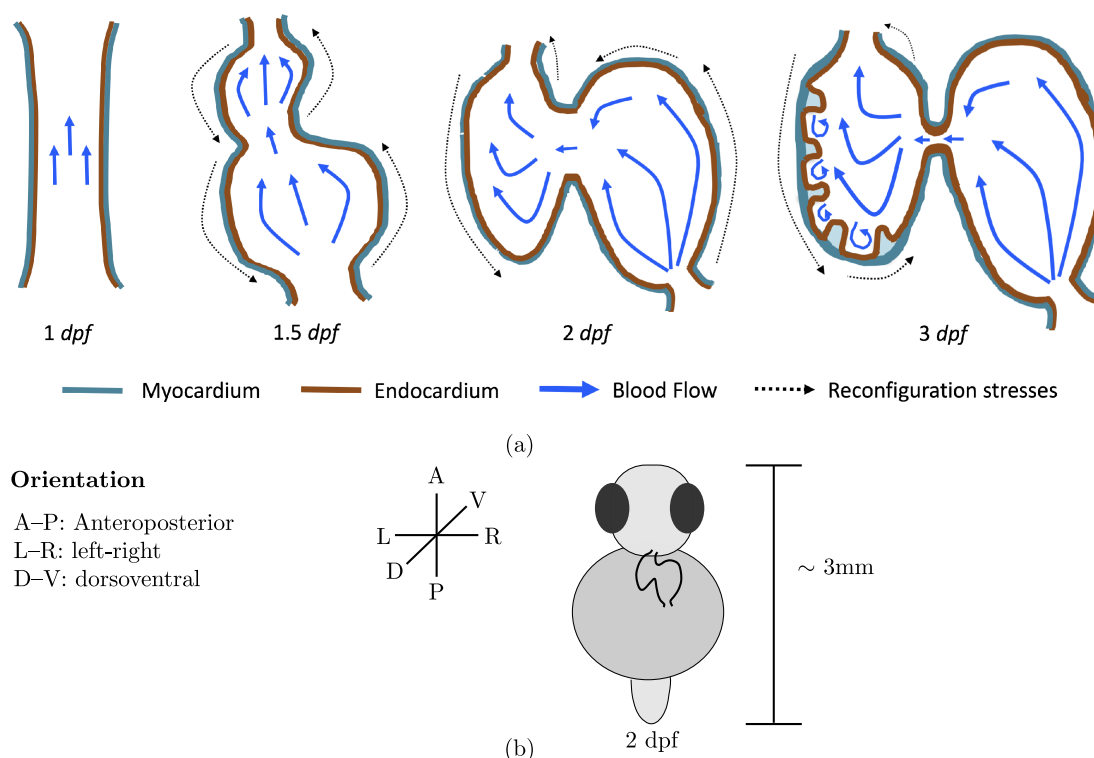


Figure A.4 – Zebrafish heart development. (a) the zebrafish heart first pumps blood through a valveless tube at 1dpf, then at 1.5 dpf the heart starts looping and forming the chambers, valve formation starts. At 2dpf the two chambers are formed and at 3dpf the valve mature. (b) Orientation of the heart and size at 2 dpf. (a) was first published in Battista *et al.*, 2019 [97] under Creative Commons Attribution License

However, at first glance, the hearts of zebrafishes and humans are quite different as zebrafishes are not mammals and have two instead of four heart chambers. Fig. A.4 (a) shows the development of a zebrafish heart, from 1 day post fertilisation (dpf), to 3 dpf. At 1 dpf the heart is a peristaltic tube, that pumps the blood without valves or chambers. At 1.5 dpf, the heart start looping and the chambers and the valves start to form. At 2 dpf the looping is done, two chambers are formed, and the valves continue developing. At 3 dpf the valves start maturing, and trabeculation begins. Trabeculation is the process that increases the muscle mass of the heart through protrusions in the interior part of the heart [98, 27] (Fig. A.4 (c)). Fig. A.4 (b) shows the orientation of the heart, which appears on some experimental data in this thesis. It also shows the order of magnitude of a zebrafish at 2 dpf. The morphogenetic processes shown in Fig. A.4(a) are actually similar in humans [99, 100, 101, 102, 103, 104]. Zebrafishes also undergo trabeculation, which is the process of increasing the muscle (Fig. A.4 (c)) The heart of the zebrafish is also similar to the human heart in terms of heart rate and contractile dynamics [105, 106, 107].

Moreover, the zebrafish is able to regenerate several organs including the heart [108, 109], which is of course of major interest.

For all reasons mentioned above, the zebrafish became a highly used model for heart development, in particular in the context of live imaging with optical microscopes.



# Bibliography

- [1] J. M. Taylor, “Optically gated beating-heart imaging,” *Front. Physiol.*, vol. 5, 2014.
- [2] J. M. Taylor, C. J. Nelson, F. A. Bruton, A. Kaveh, C. Buckley, C. S. Tucker, A. G. Rossi, J. J. Mullins, and M. A. Denvir, “Adaptive prospective optical gating enables day-long 3D time-lapse imaging of the beating embryonic zebrafish heart,” *Nat. Commun.*, vol. 10, p. 5173, Nov. 2019.
- [3] C. J. Tralie and M. Berger, “Topological Eulerian synthesis of slow motion periodic videos,” in *2018 25th IEEE Int. Conf. Image Proces. (ICIP)*. IEEE, Oct. 2018, pp. 3573–3577.
- [4] Q. Zhang and R. Pless, *Segmenting cardiopulmonary images using manifold learning with level sets*, ser. Lecture Notes in Computer Science. Berlin, Germany: Springer, 2005, vol. 3765, ch. 48, pp. 479–488.
- [5] J. B. Tenenbaum, d. V. Silva, and J. C. Langford, “A global geometric framework for nonlinear dimensionality reduction,” *Science*, vol. 290, no. 5500, pp. 2319–2323, Dec. 2000.
- [6] P. Kner, B. B. Chhun, E. R. Griffis, L. Winoto, and M. G. L. Gustafsson, “Super-resolution video microscopy of live cells by structured illumination,” *Nature Methods*, vol. 6, no. 5, pp. 339–342, May 2009.
- [7] C. Jaques, E. Pignat, S. Calinon, and M. Liebling, “Temporal super-resolution microscopy using a hue-encoded shutter,” *Biomed. Opt. Express*, vol. 10, no. 9, pp. 4727–4741, Sep 2019.
- [8] C. Jaques, A. Ernst, N. Mercader, and M. Liebling, “Temporal resolution doubling in fluorescence light-sheet microscopy via a hue-encoded shutter and regularization,” *OSA Continuum*, vol. 3, no. 8, pp. 2195–2209, Aug 2020.
- [9] A. L. Lopez, S. Wang, and I. V. Larina, “Embryonic mouse cardiodynamic oct imaging,” *Journal of Cardiovascular Development and Disease*, vol. 7, no. 4, p. 42, 2020.
- [10] K. V. Larin, I. V. Larina, M. Liebling, and M. E. Dickinson, “Live imaging of early developmental processes in mammalian embryos with optical coherence tomography,” *J. Innov. Opt. Health Sci.*, vol. 2 3, pp. 253–259, 2009.

## Bibliography

---

- [11] I. V. Larina, N. Sudheendran, M. G. Ghosn, J. Jiang, A. Cable, K. V. Larin, and M. E. Dickinson, "Live imaging of blood flow in mammalian embryos using doppler swept-source optical coherence tomography," *Journal of biomedical optics*, vol. 13, no. 6, p. 060506, 2008.
- [12] M. Liebling, A. S. Forouhar, M. Gharib, S. E. Fraser, and M. E. Dickinson, "Four-dimensional cardiac imaging in living embryos via postacquisition synchronization of nongated slice sequences," *J. Biomed. Opt.*, vol. 10, no. 5, pp. 1–10, 2005.
- [13] M. Liebling, A. S. Forouhar, R. Wolleschensky, B. Zimmermann, R. Ankerhold, S. E. Fraser, M. Gharib, and M. E. Dickinson, "Rapid three-dimensional imaging and analysis of the beating embryonic heart reveals functional changes during development," *Dev. Dyn.*, vol. 235, no. 11, pp. 2940–2948, Nov. 2006.
- [14] O. A. Grishina, S. Wang, and I. V. Larina, "Speckle variance optical coherence tomography of blood flow in the beating mouse embryonic heart," *Journal of biophotonics*, vol. 10, no. 5, pp. 735–743, 2017.
- [15] I. V. Larina, K. V. Larin, M. E. Dickinson, and M. Liebling, "Sequential Turning Acquisition and Reconstruction (STAR) method for four-dimensional imaging of cyclically moving structures," *Biomed. Opt. Express*, vol. 3, no. 3, p. 650, Mar. 2012.
- [16] S. Bhat, I. V. Larina, K. V. Larin, M. E. Dickinson, and M. Liebling, "4D reconstruction of the beating embryonic heart from two orthogonal sets of parallel optical coherence tomography slice-sequences," *IEEE Trans. Med. Imaging*, vol. 32, no. 3, pp. 578–588, Mar. 2013.
- [17] M. W. Jenkins, O. Q. Chughtai, A. N. Basavanahally, M. Watanabe, and A. M. Rollins, "In vivo gated 4D imaging of the embryonic heart using optical coherence tomography," *J. Biomed. Opt.*, vol. 12, no. 3, p. 030505, May 2007.
- [18] M. W. Jenkins, M. Watanabe, and A. M. Rollins, "Longitudinal imaging of heart development with optical coherence tomography," *IEEE J. Sel. Top. Quantum Electron.*, vol. 18, no. 3, pp. 1166–1175, 2012.
- [19] M. Gargsha, M. W. Jenkins, D. L. Wilson, and A. M. Rollins, "High temporal resolution OCT using image-based retrospective gating," *Opt. Express*, vol. 17, no. 13, pp. 10 786–10 799, Jun. 2009.
- [20] U. Sharma, E. W. Chang, and S. H. Yun, "Long-wavelength optical coherence tomography at 1.7 microm for enhanced imaging depth," *Optics express*, vol. 16, no. 24, pp. 19 712–19 723, Nov 2008.
- [21] K. Guesmi, L. Abdeladim, S. Tozer, P. Mahou, T. Kumamoto, K. Jurkus, P. Rigaud, K. Loulier, N. Dray, P. Georges, M. Hanna, J. Livet, W. Supatto, E. Beaurepaire, and F. Druon, "Dual-color deep-tissue three-photon microscopy with a multiband infrared laser," *Light: Science & Applications*, vol. 7, no. 1, p. 12, Jun 2018.



- 
- [22] C. J. Rowlands, O. T. Bruns, D. Franke, D. Fukamura, R. K. Jain, M. G. Bawendi, and P. T. C. So, "Increasing the penetration depth of temporal focusing multiphoton microscopy for neurobiological applications," *Journal of Physics D: Applied Physics*, vol. 52, no. 26, p. 264001, apr 2019.
- [23] M. Mickoleit, B. Schmid, M. Weber, F. O. Fahrbach, S. Hombach, S. Reischauer, and J. Huiskens, "High-resolution reconstruction of the beating zebrafish heart," *Nat. Methods*, vol. 11, no. 9, pp. 919–922, Sep. 2014.
- [24] V. Trivedi, T. V. Truong, L. A. Trinh, D. B. Holland, M. Liebling, and S. E. Fraser, "Dynamic structure and protein expression of the live embryonic heart captured by 2-photon light sheet microscopy and retrospective registration," *Biomed. Opt. Express*, vol. 6, no. 6, pp. 2056–2066, May 2015.
- [25] C. J. Greer and T. E. Holy, "Fast objective coupled planar illumination microscopy," *Nat. Commun.*, vol. 10, no. 1, p. 4483, Oct 2019.
- [26] O. Mariani, K. G. Chan, A. Ernst, N. Mercader, and M. Liebling, "Virtual high-framerate microscopy of the beating heart via sorting of still images," in *2019 IEEE 16th Inter. Symp. on Biomed. Imaging, (ISBI 2019)*, Apr. 2019, pp. 312–315.
- [27] D. W. Staudt, J. Liu, K. S. Thorn, N. Stuurman, M. Liebling, and D. Y. R. Stainier, "High-resolution imaging of cardiomyocyte behavior reveals two distinct steps in ventricular trabeculation," *Development*, vol. 141, no. 3, pp. 585–593, 2014. [Online]. Available: <http://dev.biologists.org/content/141/3/585>
- [28] J. Huiskens and D. Y. R. Stainier, "Selective plane illumination microscopy techniques in developmental biology," *Development*, vol. 136, no. 12, pp. 1963–1975, Jun. 2009.
- [29] J. M. Taylor, J. M. Girkin, and G. D. Love, "High-resolution 3D optical microscopy inside the beating zebrafish heart using prospective optical gating," *Biomed. Opt. Express*, vol. 3, no. 12, p. 3043, Dec. 2012.
- [30] P. Mahou, J. Vermot, E. Beaurepaire, and W. Supatto, "Multicolor two-photon light-sheet microscopy," *Nat. Methods*, vol. 11, no. 6, pp. 600–601, Jun. 2014.
- [31] R. F. Stellingwerf, "Period determination using phase dispersion minimization," *Astrophys. J.*, vol. 224, pp. 953–960, Sep. 1978.
- [32] M. M. Dworetzky, "A period-finding method for sparse randomly spaced observations or "How long is a piece of string?,"" *Mon. Not. R. Astron. Soc.*, vol. 203, no. 4, pp. 917–924, Aug. 1983.
- [33] C. M. Happel, J. Thommes, L. Thrane, J. Männer, T. Ortmaier, B. Heimann, and T. M. Yelbuz, "Rotationally acquired four-dimensional optical coherence tomography of embryonic chick hearts using retrospective gating on the common central A-scan," *J. Biomed. Opt.*, vol. 16, no. 9, pp. 1–7, Sep. 2011.

## Bibliography

---

- [34] W. Cook, “Concorde Home.” [Online]. Available: <http://www.math.uwaterloo.ca/tsp/concorde.html>
- [35] D. Applegate, W. Cook, S. Dash, and M. Mevenkamp, “QSopt linear programming solver.” [Online]. Available: <http://www.math.uwaterloo.ca/~bico/qsopt/index.html>
- [36] D. L. Applegate, R. E. Bixby, V. Chvatal, and W. J. Cook, *The Traveling Salesman Problem: A Computational Study*, ser. Princeton Series in Applied Mathematics. Princeton, NJ, USA: Princeton University Press, 2007.
- [37] H. H. Hoos and T. Stützle, “On the empirical time complexity of finding optimal solutions vs proving optimality for Euclidean TSP instances,” *Optim. Lett.*, vol. 9, no. 6, pp. 1247–1254, Aug. 2015.
- [38] S. Rohr, C. Otten, and S. Abdelilah-Seyfried, “Asymmetric Involution of the Myocardial Field Drives Heart Tube Formation in Zebrafish,” *Circ Res.*, vol. 102, no. 2, pp. e12–e19, 2008.
- [39] M. Westerfield, *The Zebrafish Book: A Guide for the Laboratory Use of Zebrafish*, 4th ed. Univ. of Oregon Press, Eugene, 2000.
- [40] P. Pitrone, J. Schindelin, L. Stuyvenberg, S. Preibisch, M. Weber, K. Eliceiri, J. Huisken, and P. Tomancak, “OpenSPIM: An open-access light-sheet microscopy platform,” *Nat. Methods*, vol. 10, pp. 598–599, 2013.
- [41] B. D. Lucas and T. Kanade, “An iterative image registration technique with an application to stereo vision,” in *IJCAI Proc. 7th Int. Joint Conf. Artif. Intell.*, ser. IJCAI’81, vol. 2. San Francisco, CA, USA: Morgan Kaufmann Publishers Inc., Aug 1981, p. 674–679.
- [42] J. Shi and C. Tomasi, “Good features to track,” in *Proc. IEEE Conf. Comput. Vis. Pattern Recognit.*, 1994, pp. 593–600.
- [43] M. Behrndt, G. Salbreux, P. Campinho, R. Hauschild, F. Oswald, J. Roensch, S. W. Grill, and C.-P. Heisenberg, “Forces Driving Epithelial Spreading in Zebrafish Gastrulation,” *Science*, vol. 338, no. 6104, pp. 257–260, 2012.
- [44] A. Edelstein, N. Amodaj, K. Hoover, R. Vale, and N. Stuurman, “Computer Control of Microscopes Using  $\mu$ Manager,” *Curr. Protoc. Mol. Biol.*, vol. 92, no. 1, pp. 14.20.1–14.20.17, 2010.
- [45] O. Mariani, A. Ernst, N. Mercader, and M. Liebling, “Reconstruction of image sequences from ungated and scanning-aberrated laser scanning microscopy images of the beating heart,” *IEEE Trans. Comput. Imag.*, vol. 6, pp. 385–395, 2020.
- [46] A. Zhang, Q. Zhang, C.-L. Chen, and R. K. Wang, “Methods and algorithms for optical coherence tomography-based angiography: a review and comparison,” *J. Biomed. Opt.*, vol. 20, no. 10, pp. 1–11, Oct. 2015.

- 
- [47] A. Liu, R. Wang, K. Thornburg, and S. Rugonyi, "Efficient postacquisition synchronization of 4-D nongated cardiac images obtained from optical coherence tomography: application to 4-D reconstruction of the chick embryonic heart," *J. Biomed. Opt.*, vol. 14, no. 4, pp. 1–11, Jul. 2009.
- [48] J. Rietdorf and E. H. K. Stelzer, "Special optical elements," in *Handbook of Biological Confocal Microscopy*, 3rd ed., J. B. Pawley, Ed. Springer Science & Business Media, 2006, ch. 3, pp. 52–54.
- [49] P. Gonnord and R. Varma, "Imaging distributions of molecules in motile cells by high-speed confocal microscopy," in *Fluorescent Methods to Study Biological Membranes*, ser. Springer Series on Fluorescence, Y. Mely and G. Duportail, Eds. Springer Science & Business Media, 2013, vol. 13, ch. 2.2, pp. 369–370.
- [50] J. Huff, A. Bergter, J. Birkenbeil, I. Kleppe, and R. Engelmann, "The new 2D superresolution mode for ZEISS Airyscan," *Nat. Methods*, vol. 14, no. 12, pp. iv–vi, Nov. 2017.
- [51] D. Toomre and J. B. Pawley, "Disk-scanning confocal microscopy," in *Handbook of Biological Confocal Microscopy*, 3rd ed., J. B. Pawley, Ed. Springer Science & Business Media, 2006, ch. 10, pp. 231–232.
- [52] P.-Y. Lam, R. S. Fischer, W. D. Shin, C. M. Waterman, and A. Huttenlocher, *Spinning disk confocal imaging of neutrophil migration in zebrafish*, ser. Methods in Molecular Biology. Humana Press, 2014, vol. 1124, ch. 14, pp. 219–233.
- [53] S. Inoué and T. Inoué, *Direct-View High-Speed Confocal Scanner: The CSU-10*, ser. Methods in Cell Biology. Elsevier, 2002, vol. 70, pp. 87–127.
- [54] E. J. Gualda, T. Vale, P. A., J. A. Feijó, G. G. Martins, and N. Moreno, "OpenSpinMicroscopy: an open-source integrated microscopy platform," *Nat. Methods*, vol. 10, p. 599, 2013.
- [55] J. Huff, "The Airyscan detector from ZEISS: confocal imaging with improved signal-to-noise ratio and super-resolution," *Nat. Methods*, vol. 12, p. 1205, 2015.
- [56] J. B. Tenenbaum, V. de Silva, and J. C. Langford, "A global geometric framework for nonlinear dimensionality reduction," *Science*, vol. 290, pp. 2319–2323, Dec. 2000.
- [57] P. Kellman, C. Chefd'hotel, C. H. Lorenz, C. Mancini, A. E. Arai, and E. R. McVeigh, "High spatial and temporal resolution cardiac cine MRI from retrospective reconstruction of data acquired in real time using motion correction and resorting," *Magn. Reson. Med.*, vol. 62, no. 6, pp. 1557–1564, Dec. 2009.
- [58] L. Feng, L. Axel, H. Chandarana, K. T. Block, D. K. Sodickson, and R. Otazo, "XD-GRASP: Golden-angle radial MRI with reconstruction of extra motion-state dimensions using compressed sensing," *Magn. Reson. Med.*, vol. 75, no. 2, pp. 775–788, Feb. 2016.

## Bibliography

---

- [59] P. Hanslovsky, J. Bogovic, and S. Saalfeld, “Image-based correction of continuous and discontinuous non-planar axial distortion in serial section microscopy,” *Bioinformatics*, vol. 33, no. 9, pp. 1379–1386, May 2017.
- [60] G. De Haan and E. B. Bellers, “Deinterlacing—an overview,” *Proc. IEEE*, vol. 86, no. 9, pp. 1839–1857, Sep. 1998.
- [61] S. Lee, C. Vinegoni, M. Sebas, and R. Weissleder, “Automated motion artifact removal for intravital microscopy, without a priori information,” *Sci. Rep.*, vol. 4, Mar. 2014.
- [62] M. Unser, “Splines: a perfect fit for signal and image processing,” *IEEE Signal Process. Mag.*, vol. 16, no. 6, pp. 22–38, Jun. 1999.
- [63] J. A. Nelder and R. Mead, “A simplex method for function minimization,” *Comput. J.*, vol. 7, no. 4, pp. 308–313, 1965.
- [64] P. Jaccard, “Étude de la distribution florale dans une portion des Alpes et du Jura,” *Bulletin de la société vaudoise des sciences naturelles*, vol. 37, pp. 547–579, 1901.
- [65] C.-J. Huang, C.-T. Tu, C.-D. Hsiao, F.-J. Hsieh, and H.-J. Tsai, “Germ-line transmission of a myocardium-specific GFP transgene reveals critical regulatory elements in the cardiac myosin light chain 2 promoter of zebrafish,” *Dev. Dyn.*, vol. 228, no. 1, pp. 30–40, Sep. 2003.
- [66] J. Ohn and M. Liebling, “In vivo, high-throughput imaging for functional characterization of the embryonic zebrafish heart,” in *2011 IEEE Inter. Symp. on Biomed. Imaging: From Nano to Macro*, Mar. 2011, pp. 1549–1552.
- [67] J. Vermot, A. S. Forouhar, M. Liebling, D. Wu, D. Plummer, M. Gharib, and S. E. Fraser, “Reversing blood flows act through *klf2a* to ensure normal valvulogenesis in the developing heart,” *PLOS Biology*, vol. 7, no. 11, pp. 1–14, Nov. 2009.
- [68] W. R. Barrionuevo and W. W. Burggren, “O<sub>2</sub> consumption and heart rate in developing zebrafish (*Danio rerio*): influence of temperature and ambient O<sub>2</sub>,” *Am. J. Physiol. Regul. Integr. Comp. Physiol.*, vol. 276, no. 2, pp. R505–R513, 1999, PMID: 9950931.
- [69] J. Vermot, S. E. Fraser, and M. Liebling, “Fast fluorescence microscopy for imaging the dynamics of embryonic development,” *HFSP J.*, vol. 2, no. 3, pp. 143–155, Jun. 2008.
- [70] A.-L. Duchemin, H. Vignes, and J. Vermot, “Mechanically activated piezo channels modulate outflow tract valve development through the Yap1 and Klf2-Notch signaling axis,” *eLife*, vol. 8, p. e44706, Sep 2019.
- [71] F. Gunawan, A. Gentile, S. Gauvrit, D. Y. Stainier, and A. Bensimon-Brito, “Nfatc1 promotes interstitial cell formation during cardiac valve development in zebrafish,” *Circulation Research*, vol. 126, no. 8, pp. 968–984, 2020.

- 
- [72] A. Felker, K. D. Prummel, A. M. Merks, M. Mickoleit, E. C. Brombacher, J. Huisken, D. Panáková, and C. Mosimann, “Continuous addition of progenitors forms the cardiac ventricle in zebrafish,” *Nature communications*, vol. 9, no. 1, pp. 2001–2001, May 2018.
- [73] V. Uribe, R. Ramadass, D. Dogra, S. J. Rasouli, F. Gunawan, H. Nakajima, A. Chiba, S. Reischauer, N. Mochizuki, and D. Y. R. Stainier, “In vivo analysis of cardiomyocyte proliferation during trabeculation,” *Development*, vol. 145, no. 14, 2018.
- [74] L. Andrés-Delgado and N. Mercader, “Interplay between cardiac function and heart development,” *Biochimica et biophysica acta*, vol. 1863, no. 7 Pt B, pp. 1707–1716, Jul 2016.
- [75] M. A. Denvir, C. S. Tucker, and J. J. Mullins, “Systolic and diastolic ventricular function in zebrafish embryos: Influence of norepinephrine, ms-222 and temperature,” *BMC Biotechnology*, vol. 8, no. 1, p. 21, Feb 2008.
- [76] M. Liebling, J. Vermot, and S. E. Fraser, “Double time-scale image reconstruction of the beating and developing embryonic zebrafish heart,” in *2008 5th IEEE International Symposium on Biomedical Imaging: From Nano to Macro*, May 2008, pp. 855–858.
- [77] J. Pestel, R. Ramadass, S. Gauvrit, C. Helker, W. Herzog, and D. Y. R. Stainier, “Real-time 3D visualization of cellular rearrangements during cardiac valve formation,” *Development*, vol. 143, no. 12, pp. 2217–2227, 2016.
- [78] D. G. C. Hildebrand, M. Cicconet, R. M. Torres, W. Choi, T. M. Quan, J. Moon, A. W. Wetzel, A. Scott Champion, B. J. Graham, O. Randlett, G. S. Plummer, R. Portugues, I. H. Bianco, S. Saalfeld, A. D. Baden, K. Lillaney, R. Burns, J. T. Vogelstein, A. F. Schier, W.-C. A. Lee, W.-K. Jeong, J. W. Lichtman, and F. Engert, “Whole-brain serial-section electron microscopy in larval zebrafish,” *Nature*, vol. 545, no. 7654, pp. 345–349, May 2017.
- [79] A. W. Wetzel, J. Bakal, M. Dittrich, D. G. C. Hildebrand, J. L. Morgan, and J. W. Lichtman, “Registering large volume serial-section electron microscopy image sets for neural circuit reconstruction using fft signal whitening,” in *2016 IEEE Applied Imagery Pattern Recognition Workshop (AIPR)*, 2016, pp. 1–10.
- [80] S. Saalfeld, R. Fetter, A. Cardona, and P. Tomancak, “Elastic volume reconstruction from series of ultra-thin microscopy sections,” *Nature Methods*, vol. 9, no. 7, pp. 717–720, Jul 2012.
- [81] A. Cardona, S. Saalfeld, J. Schindelin, I. Arganda-Carreras, S. Preibisch, M. Longair, P. Tomancak, V. Hartenstein, and R. J. Douglas, “TrakEM2 Software for Neural Circuit Reconstruction,” *PLOS ONE*, vol. 7, no. 6, pp. 1–8, 06 2012.
- [82] J. Schindelin, I. Arganda-Carreras, E. Frise, V. Kaynig, M. Longair, T. Pietzsch, S. Preibisch, C. Rueden, S. Saalfeld, B. Schmid, J.-Y. Tinevez, D. J. White, V. Hartenstein, K. Eliceiri, P. Tomancak, and A. Cardona, “Fiji: an open-source platform for biological-image

## Bibliography

---

- analysis,” *Nat. Methods*, vol. 9, no. 7, pp. 676–682, Jul 2012. [Online]. Available: <https://doi.org/10.1038/nmeth.2019>
- [83] IBM ILOG Cplex, “V12. 1: User’s Manual for CPLEX,” *International Business Machines Corporation*, vol. 46, no. 53, p. 157, 2009, V.12.10 [2019].
- [84] J. Ohn, H.-J. Tsai, and M. Liebling, “Joint dynamic imaging of morphogenesis and function in the developing heart,” *Organogenesis*, vol. 5, no. 4, pp. 248–255, Oct. 2009.
- [85] H. Sánchez-Iranzo, M. Galardi-Castilla, C. Minguillón, A. Sanz-Morejón, J. M. González-Rosa, A. Felker, A. Ernst, G. Guzmán-Martínez, C. Mosimann, and N. Mercader, “Tbx5a lineage tracing shows cardiomyocyte plasticity during zebrafish heart regeneration,” *Nat Commun.*, vol. 9, no. 1, p. 428, Jan. 2018.
- [86] J. He and J. Huisken, “Image quality guided smart rotation improves coverage in microscopy,” *Nature Communications*, vol. 11, no. 1, p. 150, Jan 2020.
- [87] M. Henglin, G. Stein, P. V. Hushcha, J. Snoek, A. B. Wiltschko, and S. Cheng, “Machine learning approaches in cardiovascular imaging,” *Circulation: Cardiovascular Imaging*, vol. 10, no. 10, p. e005614, 2017.
- [88] D. Dey, P. J. Slomka, P. Leeson, D. Comaniciu, S. Shrestha, P. P. Sengupta, and T. H. Marwick, “Artificial intelligence in cardiovascular imaging: JACC state-of-the-art review,” *J. Am. Coll. Cardiol.*, vol. 73, no. 11, pp. 1317–1335, Mar 2019.
- [89] N. Duchateau, A. P. King, and M. De Craene, “Machine learning approaches for myocardial motion and deformation analysis,” *Frontiers in Cardiovascular Medicine*, vol. 6, p. 190, 2020.
- [90] G. Litjens, F. Ciompi, J. M. Wolterink, B. D. de Vos, T. Leiner, J. Teuwen, and I. Išgum, “State-of-the-art deep learning in cardiovascular image analysis,” *JACC: Cardiovascular Imaging*, vol. 12, no. 8, Part 1, pp. 1549 – 1565, 2019.
- [91] A. A. Akerberg, C. E. Burns, C. G. Burns, and C. Nguyen, “Deep learning enables automated volumetric assessments of cardiac function in zebrafish,” *Disease Models & Mechanisms*, vol. 12, no. 10, 2019.
- [92] Y. Ding, V. Gudapati, R. Lin, Y. Fei, R. R. S. Packard, S. Song, C. Chang, K. I. Baek, Z. Wang, M. Roustaei, D. Kuang, j. kuo, and T. K. Hsiai, “Saak transform-based machine learning for light-sheet imaging of cardiac trabeculation,” *IEEE Transactions on Biomedical Engineering*, pp. 1–1, 2020.
- [93] W. Denk, D. W. Piston, and W. W. Watt, “Multi-photon molecular excitation in laser-scanning microscopy,” in *Handbook of Biological Confocal Microscopy*, 3rd ed., J. B. Pawley, Ed. Springer Science & Business Media, 2006, ch. 28, pp. 535–594.

- 
- [94] C. T. Nguyen, Q. Lu, Y. Wang, and J.-N. Chen, "Zebrafish as a model for cardiovascular development and disease," *Drug discovery today. Disease models*, vol. 5, no. 3, pp. 135–140, 2008.
- [95] C. E. Genge, E. Lin, L. Lee, X. Sheng, K. Rayani, M. Gunawan, C. M. Stevens, A. Y. Li, S. S. Talab, T. W. Claydon, L. Hove-Madsen, and G. F. Tibbits, *The Zebrafish Heart as a Model of Mammalian Cardiac Function*. Cham: Springer International Publishing, 2016, pp. 99–136.
- [96] P. Giardoglou and D. Beis, "On zebrafish disease models and matters of the heart," *Biomedicines*, vol. 7, no. 1, p. 15, Feb 2019.
- [97] N. A. Battista, D. R. Douglas, A. N. Lane, L. A. Samsa, J. Liu, and L. A. Miller, "Vortex dynamics in trabeculated embryonic ventricles," *Journal of cardiovascular development and disease*, vol. 6, no. 1, p. 6, Jan 2019.
- [98] S. J. Rasouli and D. Y. R. Stainier, "Regulation of cardiomyocyte behavior in zebrafish trabeculation by neuregulin 2a signaling," *Nat. Commun.*, vol. 8, no. 1, pp. 1–11, 2017.
- [99] D. Yelon, "Cardiac patterning and morphogenesis in zebrafish," *Developmental Dynamics*, vol. 222, no. 4, pp. 552–563, 2001.
- [100] P. J. Scherz, J. Huisken, P. Sahai-Hernandez, and D. Y. R. Stainier, "High-speed imaging of developing heart valves reveals interplay of morphogenesis and function," *Development*, vol. 135, no. 6, pp. 1179–1187, 2008.
- [101] R. T. Martin and T. Bartman, "Analysis of heart valve development in larval zebrafish," *Developmental Dynamics*, vol. 238, no. 7, pp. 1796–1802, 2009.
- [102] E. Steed, N. Faggianelli, S. Roth, C. Ramspacher, J.-P. Concordet, and J. Vermot, "klf2a couples mechanotransduction and zebrafish valve morphogenesis through fibronectin synthesis," *Nat. Commun.*, vol. 7, no. 1, p. 11646, May 2016.
- [103] F. Gunawan, A. Gentile, R. Fukuda, A. T. Tsedeke, V. Jiménez-Amilburu, R. Ramadass, A. Iida, A. Sehara-Fujisawa, and D. Y. R. Stainier, "Focal adhesions are essential to drive zebrafish heart valve morphogenesis," *The Journal of cell biology*, vol. 218, no. 3, pp. 1039–1054, Mar 2019.
- [104] V. A. Lombardo, M. Heise, M. Moghtadaei, D. Bornhorst, J. Männer, and S. Abdelilah-Seyfried, "Morphogenetic control of zebrafish cardiac looping by bmp signaling," *Development*, vol. 146, no. 22, 2019.
- [105] R. Arnaout, T. Ferrer, J. Huisken, K. Spitzer, D. Y. R. Stainier, M. Tristani-Firouzi, and N. C. Chi, "Zebrafish model for human long qt syndrome," *Proceedings of the National Academy of Sciences*, vol. 104, no. 27, pp. 11 316–11 321, 2007.

## Bibliography

---

- [106] I. U. S. Leong, J. R. Skinner, A. N. Shelling, and D. R. Love, “Zebrafish as a model for long qt syndrome: the evidence and the means of manipulating zebrafish gene expression,” *Acta Physiologica*, vol. 199, no. 3, pp. 257–276, 2010.
- [107] M. Vornanen and M. Hassinen, “Zebrafish heart as a model for human cardiac electrophysiology,” *Channels (Austin, Tex.)*, vol. 10, no. 2, pp. 101–110, 2016.
- [108] G. Beffagna, “Zebrafish as a smart model to understand regeneration after heart injury: How fish could help humans,” *Frontiers in cardiovascular medicine*, vol. 6, pp. 107–107, Aug 2019.
- [109] I. J. Marques, E. Lupi, and N. Mercader, “Model systems for regeneration: zebrafish,” *Development*, vol. 146, no. 18, 2019.



# OLIVIA MARIANI

1903 Collonges – Switzerland

Current: +41 (0)27 721 77 90 – olivia.mariani@idiap.ch

Permanent: +41 (0)76 822 53 62 – olivia.e.mariani@gmail.com

## EXPERIENCE

---

- |          |   |
|----------|---|
| 2020     | <b>Idiap &amp; EPFL PhD Candidate</b>   |
| 2016     | <i>Computational Bioimaging Group, Prof. Michael Liebling</i> Martigny <ul style="list-style-type: none"><li>· Thesis: "Computational methods for live heart imaging with speed-constrained microscopes"</li></ul>  |
| 2015     | <b>EPFL Image analysis</b>  |
| 2013     | <i>Lausanne</i> Laboratory of Microbiology and Microsystems, Prof. John McKinney <ul style="list-style-type: none"><li>· Finalisation of the master thesis (Java, Eclipse)</li><li>· Data analysis (Matlab)</li></ul>   |
| 2013     | <b>Weill Cornell Medical College Image analysis internship</b>  |
| August   | <i>New York City</i> Laboratory of Prof. Carl Nathan <ul style="list-style-type: none"><li>· Image/Data analysis (ImageJ, Matlab)</li></ul>   |
| 2012     | <b>QGel Image analysis internship</b>   |
| Summer   | <i>Innovation Square</i> Lausanne <ul style="list-style-type: none"><li>· Quality control of current image analysis protocol (Cell Profiler, Cell Profiler Analyst)</li><li>· ImageJ plugin development for 3D image analysis</li></ul>   |
| 2013     | <b>EPFL Java application for sinusoid function fitting</b>  |
| February | <i>Lausanne</i> Biomedical Imaging Group, Prof. Michael Unser <ul style="list-style-type: none"><li>· Collaboration with Dr. Charna Dibner, Circadian Endocrinology Group, University Hospital of Geneva</li><li>· Standalone java application, eclipse environment</li><li>· Sinusoid fitting on data points</li></ul> |

## PUBLICATIONS

---

- |      |  |
|------|--|
| 2021 | O. Mariani, A. Ernst, N. Mercader, and M. Liebling, "Constrained cardiac sequence extraction from series of still images with unknown phase," In preparation   |
| 2021 | O. Mariani, F. Marelli, C. Jaques, A. Ernst, and M. Liebling, "Unequivocal cardiac phase sorting from alternating ramp- and pulse- illuminated microscopy image sequences," Submitted  |
| 2020 | O. Mariani, A. Ernst, N. Mercader, and M. Liebling, "Reconstruction of image sequences from ungated and scanning-aberrated laser scanning microscopy images of the beating heart," <i>IEEE Trans. Comput. Imag.</i> , vol. 6, pp. 385–395, 2020      |
| 2019 | O. Mariani, K. G. Chan, A. Ernst, N. Mercader, and M. Liebling, "Virtual high-framerate microscopy of the beating heart via sorting of still images," in <i>2019 IEEE 16th Inter. Symp. on Biomed. Imaging, (ISBI 2019)</i> , Apr. 2019, pp. 312–315 |

- 2015 J. Vaubourgeix, G. Lin, N. Dhar, N. Chenouard, X. Jiang, H. Botella, T. Lupoli, O. Mariani, G. Yang, O. Ouerfelli, M. Unser, D. Schnappinger, J. McKinney, and C. Nathan, “Stressed mycobacteria use the chaperone ClpB to sequester irreversibly oxidized proteins asymmetrically within and between cells,” *Cell host & microbe*, vol. 17, no. 2, pp. 178–190, Feb 2015
- 2013 T. Mannic, P. Meyer, F. Triponez, M. Pusztaszeri, G. Le Martelot, O. Mariani, D. Schmitter, D. Sage, J. Philippe, and C. Dibner, “Circadian clock characteristics are altered in human thyroid malignant nodules,” *The Journal of Clinical Endocrinology & Metabolism*, vol. 98, no. 11, pp. 4446–4456, 11 2013

## EDUCATION

---

- 2013 **MSc in Bioengineering EPFL**
- Master thesis: “Cell Tracking in live cell imaging”  
School of engineering, Bioimaging Group, Prof. Michael Unser
  - Minor in Biomedical Technologies  
Minor thesis: “Source EEG connectivity without inverse solution”  
**University Hospital of Vaud**, Biomedical Imaging Centre, Dr. Maria Knyazeva
- 2011 **BSc in Life Sciences and Technologies EPFL**
- *Bachelor thesis*: “Analysis of PGRP-LA gene function in the fitness of *Drosophila Melanogaster*“, EPFL, Global Health Institute (GHI), Laboratory of Prof. Bruno Lemaitre

## TECHNICAL STRENGTHS

---

<b>Computer Languages</b>	Python, Java
<b>Image analysis software</b>	ImageJ (plugins & macros), Imaris, Matlab
<b>Basic biological knowledge</b>	Developmental biology, Microbiology, Immunology

## SOFT SKILLS

---

Team spirit, Open-minded, Inclusive

## HOBBIES

---

Hiking, paragliding, skiing